POLITECNICO DI MILANO

Facoltà di Ingegneria Industriale

Corso di Laurea in
Ingegneria Meccanica

COMPARISON OF LASER WELDED AND RESISTANCE SPOT WELDED OVERLAP JOINTS OF MAGNESIUM AZ31B SHEETS

Relatore: Prof. Barbara PREVITALI

Co-relatore: Dr. Ing. Nikolai KASHAEV

Tesi di Laurea di:

Salvatore GIAMMARINARO Matr. 766067

Anno Accademico 2012 - 2013

Acknowledgements

The present work was accomplished during my work as Master student in the Department Joining and Assessment of the Helmholtz-Zentrum Geesthacht (HZG) in collaboration with SITEC Laboratory for Laser Application and STADCO Saarlouis Ltd.
I could perform the full experimental work in the Institute of Materials Research, Materials Mechanics, Department Joining and Assessment of the HZG.
I would like to thank Dr. Ing. Nikolai Kashaev and Prof. Barbara Previtali for the excellent care following my work with personal commitment and also granting the freedom to implement my own ideas.
I thank Stefan Riekehr and Daniele Colombo for their constant assistance and trust on my independent way of working.
My thanks to all the employees of the Department Joining and Assessment: my special thanks for their support and friendship in all situations.
I would like to thank Volker Ventzke and Jürgen Knaack for the stimulating technical discussions regarding various aspects of the work.
I would like to thank René Dinse, Peter Haack, Emma Morales and the STADCO team for their assistance with various aspects of the experimental program.

Article included in the International Conference on Joining of Materials Proceedings (JOM-17 2013, Helsingør, Denmark) [1]

S. Giammarinaro, S. Riekehr, B. Previtali, M. Hibben, N. Kashaev.

Institute for the Joining of Materials
Founded in 1979

Mechanical Performance of Laser Welded and Resistance Spot Welded Overlap Joints from Magnesium AZ31B Sheets,

JOM-17 Proc. (2013)

Contents

List of the figures

List of the tables

List of graphs

List of symbols and abbreviations

N_e	electron density
N_i	ion density
ω	frequency of the incident electromagnetic wave
T	temperature
EPMA	Electron Probe Micro-Analysis
SEM	Scanning Electron Microscope
EDX	Energy Dispersive X-Ray
EBSD	Electron Backscatter Diffraction
DOE	Design Of Experiment
ANOVA	Analysis Of Variance
FP	beam focus position
v	welding speed
P	laser beam power
Gas	shielding gas
Ar	Argon
He	Helium
DoP	Depth-Of-Penetration ratio
λ	wavelength of the laser beam
d_{fo}	fiber diameter on robot
f_f	focalization length (f)
f_r	collimation length
d_o	waist diameter of the laser beam
d_f	beam diameter out of the source
$d_o(z)$	laser beam spot diameter on work-piece (z-function)
z-zo	focus position
A (z=-2.5mm)	spot area @ surface, FP= -2.5mm
A (z= 0mm)	spot area @ surface, FP= 0mm

Abstract

Magnesium is already used as a cast alloy in the automotive industry. Using Mg wrought alloys - e.g., in the form of sheets - will allow for further weight reduction potential. In automobile manufacturing, laser beam welding is concurring to resistance spot welding due to its high process flexibility and efficiency. The rule of thumb is that a joint can be laser welded if it can be seen, which allows for complex structures to be realised. Nevertheless, studies concerning the mechanical performance of laser welded Mg overlap joints are scarce. The aim of this work was to develop a process for laser welding single overlap joints of 2.5 mm thick Mg sheets, AZ31B, and investigate the mechanical performance of these joints relative to resistance spot welded joints. A Nd:YAG laser was used for the welding experiments, and a design of experiment approach was applied. Both mechanical testing and advanced metallurgical examinations were used to establish the process-property-performance relationship of the overlap joints. The micro-hardness, shear tensile and fatigue tests were implemented for the mechanical characterisation. To improve the fatigue behaviour, different joint geometries (linear, circular and C-shape) were investigated. The developed surface preparation provided welds with optimal bead geometry and without cracks and pores. Compared with conventional resistance spot welds, laser welded joints showed improved fatigue behaviour with comparable performance for the tensile shear strength. The developed laser process can also be implemented via remote scanner welding. For example, it is expected that using a scanner optic increases the throughput and reduces the cost of automotive production.

Keywords: Laser Beam Welding, Resistance Spot Welding, Overlap Joint, Magnesium Alloy, Mechanical Performance, Fatigue Behaviour

Sommario

Il Magnesio è già impiegato nel settore automobilistico come prodotto di fonderia. Utilizzando leghe di magnesio da lavorazione plastica - per esempio, in forma di laminati – si prospetta un'ulteriore riduzione dei pesi. Nella fabbricazione ed assemblaggio dell'automobile, lo sviluppo della saldatura laser può sostituire la consolidata saldatura per punti (detta anche a resistenza) grazie alla sua elevata flessibilità ed efficienza di processo. In generale, un giunto può essere saldato laser se "a vista", il che permette anche la realizzazione di strutture complesse. Tuttavia, sono scarsi gli studi riguardanti le prestazioni meccaniche dei giunti per sovrapposizione (overlap), saldati al laser, di laminati in Mg. Lo scopo di questo lavoro è stato, perciò, lo sviluppo di un processo di saldatura laser per un giunto overlap di laminati in lega di magnesio AZ31B, di spessore 2.5mm, ed indagarne la bontà delle prestazioni meccaniche relativamente ai giunti saldati a resistenza. Una sorgente laser Nd:YAG è stata utilizzata per la campagna sperimentale di saldatura, realizzata seguendo i principi del DOE. Prove meccaniche ed avanzati esami metallurgici sono stati condotti per stabilire il rapporto processo-proprietà-prestazioni dei giunti per sovrapposizione. Micro-durezze, prove statiche di resistenza al taglio e numerose prove di fatica sono state eseguite per la caratterizzazione meccanica. Per migliorare il comportamento a fatica, sono state analizzate poi diverse geometrie di saldatura (lineare, circolare e C-shape). Le soluzioni adottate per la preparazione delle superfici di accoppiamento hanno fornito geometrie ottimali dei cordoni di saldatura, esenti da cricche o porosità. Rispetto ai tradizionali giunti saldati per punti, le giunzioni saldate al laser hanno mostrato un miglior comportamento a fatica e prestazioni paragonabili in termini di resistenza statica alla trazione. Il processo laser sviluppato può essere, inoltre, implementato tramite saldatura remota con un laser scanner. Si prevede, con l'utilizzo di uno scanner ottico, un aumento della produttività e una riduzione dei costi di produzione nel settore automobilistico.

Parole chiave: saldatura laser, saldatura per punti o saldatura a resistenza, giunto per sovrapposizione, lega di Magnesio, prestazioni meccaniche, comportamento a fatica

1 Introduction

In recent years, as lightweight structural metals, magnesium alloys have received increasing attention from various industries such as aerospace, automotive and electronics. The use of magnesium in automotive applications can contribute significantly to mass reduction due to the combination of its low density, both high specific strength and stiffness, and good castability [40].
Current welding methods, such as metal-arc inert gas (MIG), tungsten-arc inert gas (TIG), resistance spot welding (RSW), friction, electron beam, laser beam welding (LBW) and laser–TIG hybrid welding, have been used to join both magnesium alloys and their mechanical fasteners [2-7, 17-22].
However, the need for shorter cycle times and the inflexibility of conventional resistance spot methods for adapting to different complex structures have drawn the attention of the automotive industries to the LBW process [2]. LBW may prove a satisfactory solution due to its high speed, both low and precise heat input, low residual stress and low weld distortion. Moreover, laser spot welding in an overlap configuration challenges RSW as a single sided, non-contact process in the fabrication and assembly of car bodies. A single laser beam process can also be implemented via remote scanner welding. For example, it is expected that using a scanner optic increases the throughput and reduces the cost of automotive production.

1.1 Structure of the thesis

Background information regarding the topic are given in Section 2. The high features of magnesium alloys in terms of strength-to-weight ratio and recyclability, as compared to other alloys, make it useful in fabricating components in automotive industries. AZ31B Magnesium alloy, used in this study, has been extensively applied in advanced engineering because of its lightness. In particular, within transportation industries, the weight saving effect of replacing steel and aluminum parts is an important factor in increasing speed and reducing fuel consumption. In addition to the development of new alloy types, manufacturing techniques such as welding and joining play an essential role. Recent developments in high power lasers and robotic control have accelerated the application of LBW to car body fabrication and assembly instead of the conventional resistance spot welding process.
In Section 3, the state of the art of the laser welding and the resistance spot welding of Mg alloys is presented: in literature the weldability and the

optimization of magnesium alloy sheet are well discussed. The AZ31B magnesium alloy laser welded joint are discussed within 18 papers using several heat source (fiber lasers, hybrid, Nd:YAG, CO_2, diode,) in different joints configuration (butt, overlap, lap fillet joints). In literature is not found a mechanical characterization of overlap single laser welding joints in case of AZ31B. Moreover, any comparisons between laser beam overlap joints and resistance spot welding technologies is missing for magnesium alloy sheet. The few papers, concerning this topic, are focused on different materials like high strength steels for automotive applications.
The applied methodologies on the design of the experiments and on the mechanical results analysis are discussed in Section 5.
The laboratory equipment provided by the Helmholtz-Zentrum Geesthacht and used during the experimental work is presented in Section 6. A presentation of the laser welding system, the robot and the full mechanical test machines is given. The characteristics of the microstructure and chemical analysis equipment are shown. Therefore optical microscope, SEM, EDX, EBSD and the X-ray analysis measuring parameters are discussed.
The design of the full experimental work and the results analysis are here presented in Sections 7-8. The investigation is carried out on the linear, C-shape and circular spot welds in overlapped sheets of AZ31B Magnesium alloy using a Nd:YAG laser beam welding process. The research seeks to arrange an optimal laser-spot welding process of magnesium alloys to replace the lack of knowledge in the manufacture automotive joints. The research investigates, at first, the combination of process parameters and design of the joints that improves the structural and fatigue strength of the mechanical components. Mechanical behaviour of specimens is tested under fatigue and static loadings to compare the results with the conventional resistance spot weld joints.

2 Topic and context

The high features of magnesium alloys in terms of strength-to-weight ratio and recyclability, as compared to other alloys, make it useful in fabricating components in automotive industries. AZ31B Magnesium alloy, used in this study, has been extensively applied in advanced engineering because of its lightness. In particular, within transportation industries, the weight saving effect of replacing steel and aluminum parts is an important factor in increasing speed and reducing fuel consumption. In addition to the development of new alloy types, manufacturing techniques such as welding and joining play an essential role. Recent developments in high power lasers and robotic control have accelerated the application of LBW to car body fabrication and assembly instead of the conventional resistance spot welding process.

2.1 Properties of magnesium alloys

The major use of magnesium, consuming about 50 percent of total magnesium production, is as a component of aluminium alloys for beverage can stock. Another use for primary magnesium is in steel desulfurization.
A growing application for magnesium alloys is die cast automotive components.
Current trends to reduce energy consumption lead to efforts to minimize the total of vehicles [51]. Magnesium is the lightest of all the engineering metals, with a density of 1.74 g/cm^3 . It is 35% lighter than aluminium (2.7 g/cm^3) and over 75% lighter than steel (7.86 g/cm^3). Therefore wrought magnesium alloys in automotive applications are considered. Magnesium alloys are also used for manufacture of housings for portable electronic devices, not only for the material lightness but also for the recycling properties and the good electromagnetic shielding capabilities. Magnesium alloys have already found considerable applications in aerospace, aircraft and other fields, especially magnesium die-castings in the automotive industry.
Magnesium alloys have also been employed in nuclear energy industrial equipment due to the low tendency to absorb neutrons and good thermal conductivity. Many magnesium alloy components are used at high rotational speeds to minimize inertial forces [52].

Moreover, Mg alloy AZ31 is an attractive candidate for coronary artery stents, as it possesses excellent biocompatibility in human body and good mechanical properties [50].

2.1.1 The classification and characteristics of magnesium alloys

Magnesium is the eighth most plentiful element in the Earth's crust and the sixth most abundant metal. It is produced by extraction from seawater or by reduction (using silicon as a reducing agent) from minerals such as dolomite ($MgCa(CO_3)_2$) or magnesite ($MgCO_3$) or saltwater. It is also the third element dissolved in seawater.
The major alloying elements are aluminium, zinc, zirconium, silver and rare earths. Magnesium alloys are usually designed by two capital letters and two or three numbers following the standard four-digit ASTM designation system. The first two letters indicate the main alloying elements: A, aluminum; C, copper; E, rare earths; Q, silver; K, zirconium; M, manganese; N, nickel; S, silicon and Z, zinc. The numbers represent the nominal compositions of these alloying elements in weight rounded percentage. For example, AZ31 indicates the alloy contains a nominal 3 wt% aluminium and 1 wt% zinc.
Suffix letters A, B, C refer to variations in composition within the specified range. For instance, in the AZ31B Magnesium alloy, the B modification contains a different level of impurity compared to the AZ31.
Other following designation refer to the mechanical or thermal treatments and chemical composition specifications. For example, AZ31B-H24 designation indicates that the alloy is strain-hardned and partially annealed; AZ31hp means that the alloy has high purity.
Most of the Magnesium alloys are ternary types and they can be divided into two categories: non-structural applications and structural applications. Within the alloys for structural application the common cast alloys can be divided in the following four groups [52].

- Wrought magnesium alloys: the Mg-Al-Zn series alloys are the most widely used wrought magnesium alloys (AZ31, AZ61, AZ80). They are the most important for the industrial application because of the combination of good castability, lightness and strength. Mg-Zn-Zr series alloys have higher yielding strength thanks to the grain refinement obtained with zirconium. The AZ31 magnesium alloy consist of α-Mg (hexagonal crystal structure) and β-$Mg_{17}Al_{12}$ (cubic crystal structure) phases. The β phase could precipitate in the matrix or on the boundaries to strengthen the alloys.

- Mg-Al-X casting alloys systems: they are the most widely used magnesium casting alloys. Aluminum is the major alloying element in the ternary Mg–Al series, which comprises AZ (Mg–Al–Zn), AM (Mg–Al–Mn), AS (Mg–Al–Si) alloys and Mg–Al-rare earth (AE series). In the AZ series, such as the AZ91D alloy, the addition of zinc gives strengthening. In the AM series (AM60B, AM50A) the manganese causes good ductility improves yield strength. The AS series, as the AS41, has a better creep resistance than AZ91 at elevated temperatures but lower strength [51]. The AE series (AE42) reaches improvements in creep behaviour.

- Mg-Zn-X casting alloys systems: in the ZE series (ZE41) the rare earth addition improves the creep strength at elevated temperatures. The ability to grain refinement of Mg-Zn alloys with Zr allowed the introduction of the ZK series used as high-strength press forgings.

- Mg-Ag-X casting alloys systems: they are known as high temperature Mg casting alloys because of their high strength at elevated temperatures and good castability. QE22, for example, has been used for aerospace applications.

It is possible to classify magnesium alloys into two other groups: the materials for room temperature and for elevated temperature applications. Rare earth metals are used for high temperature alloys while aluminium and zinc are alloying elements for room temperature applications because at elevated temperatures the tensile and creep properties degrade rapidly.
Approximately 85% of all magnesium components are manufactured by casting processes because of the high cost of wrought semi-finished production [52].

Unlikely, magnesium alloys possess limited ductility and cold workability at room temperature because the deformation is limited by the HCP structure. They also have poor surface properties such as low hardness and corrosion resistance, large shrinkage during solidification and high chemical reactivity in molten state [52].
Slip occurs primarily on the {1000} basal planes in the <1120> direction. Twining on the {1012} pyramidal planes. At T>250 °C slip can also occur on pyramidal and prismatic planes.

2.1.2 AZ31B and wrought Mg alloy

Nominal composition	*UK designation*	*UK BS2970 MAG*	*USA ASTM*	*USA AMS*	*France AFNOR*	*Standard AECMA*	*W. Germany aircraft*	*W. Germany DIN 1729*
Al3Zn1Mn0.3	AZ31	S-1110	AZ31B-0	4375F	G-A2Z1	MG-P-62	W.3504	3.5312

Wrought magnesium alloys can be produced by extruding, rolling or forging in the temperature range of 300–500◦C because the forming behaviour of magnesium is poor at room temperature. Formed and drawn magnesium products are manufactured at this temperature ranges generally without a protective atmosphere. Wrought alloys generally have higher strength and ductility in comparison with cast alloys. The hexagonal structure of magnesium requires elevated forming temperatures to activate more slip systems and to allow better formability, causing higher energy consumption during processing. Additional process developments are needed for the surface appearance.
In particular, AZ31 sheet products are available on the world market in a thickness of 0.8-30 mm. AZ31 sheet as magnesium has similar hot deep-drawing characteristics as steel and aluminium sheet. At 225°C the draw ratio of AZ31 is 2.6 and is higher than that of deep drawing Al and deep drawing steels in common use which have a ratio of 2.5 and 2.2, respectively [42]. Extruded magnesium bars, sections and tubes are widely used in aerospace, nuclear, automotive and other engineering applications. For the extruded magnesium components the minimum wall thickness of Mg alloys is approximately 1.5 mm.

Table 2.1: Properties of AZ31B magnesium

Properties	**Magnesium (AZ31B)**
Crystal structure	HCP
Density at 20°C (g/cm^3)	1.78
Coefficient of thermal expansion (×10^6/C)	26.0 (20–100°C)
Elastic modulus (10^6 Mpa)	45
Tensile strength (Mpa)	232
Melting point (°C)	630
Thermal conductivity (W m^{-1} K^{-1})	84
Specific heat (J kg^{-1} K^{-1})	1050

2.1.3 The magnesium alloys in automotive applications

Magnesium alloys have recently attracted great attention in academic research owing to some unique properties such as their low density, high specific strength, elastic modulus and damping capacity, and recyclable characteristics. Moreover, magnesium, as the lightest commercial engineering metal, has recently attracted the automobile industry too. The automotive industry is one of the industries most affected by the energy, oil and financial crises experienced in recent years. The fluctuations experienced in fuel prices, in the last 30–40 years, due to crises have compelled countries to take economic precautions. In this respect, the increase in taxes and decrease in purchasing power make saving fuel a current issue for consumers. Although steel is the main material used in automobile production, materials such as aluminium, magnesium, plastic, and composites are utilised to reduce the vehicle weight [51]. To comply with ever restricting environmental laws and improve performance, automotive manufacturers are increasing the average magnesium usage per car from 3 kg in 2005 to 20 kg in 2010 [51].
Due to being lightweight, the high resistance against corrosion of the Al alloys, its durability, its low-cost maintenance, and its recovery potential its use has gradually become widespread.
To date magnesium alloys have not usually been welded because of the occurrence of defects such as oxide films, cracks, and cavities [3]. However, the wider application of magnesium alloys needs reliable welding processes. From the joining perspective, Magnesium alloy components can be welded with a variety of welding methods including tungsten-arc inert gas (TIG), metal-arc inert gas (MIG), plasma arc, electron, laser, friction, adhesive [47], ultrasonic, and resistance spot welding [16, 34-39] or joined with mechanical fasteners. Today TIG and MIG processes are the main methods for magnesium alloys, especially for the removal and repair of casting defects. However, low welding speeds, large heat affected zone (HAZ) and fusion zone (FZ), high shrinkages, variations in microstructures and properties, evaporative loss of alloying elements, high residual stress and distortion of arc-welded joints have caused attention to be drawn towards laser welding [43-45] due to the low and precise heat input, small HAZ, deep and narrow FZ, low residual stress and joint distortion, and high welding speed [29].

2.2 Laser weld joint configurations

As shown in **Fig. 2.1**, there are four main laser weld joint configurations: Butt weld, Fillet lap weld, Overlap weld, Edge flange weld.

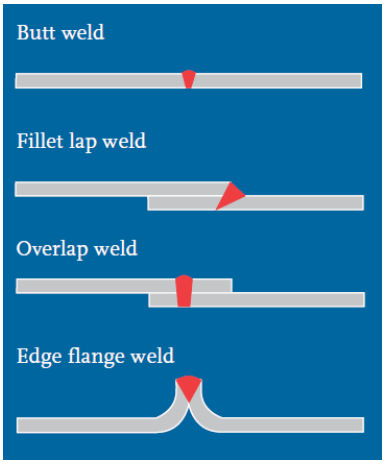

Figure 2.1: The main weld joint configurations

A butt weld is a configuration where the parts to be assembled lie on the same plane. Automotive tailored blanks are a typical application of this type of weld. The parts are joined by melting their edges, which are pressed together in order to minimize gaps. The edge fit-up is critical, especially in tailored blank welding applications. The welding of coated materials does not cause any trouble as long as the edges are not coated.
In fillet lap welds, the parts lie on top of each other, and the edge of one part is melted to bond with the surface of the other part. Weld edge preparation focuses on the joining of pure metal faces and requires removal of oxides and surface layers from the joining area.
In an overlap weld, the parts lie on top of each other. Laser spot welding is a typical application of this type of weld. Most importantly, similar to lap welds the interface of the parts to be joined must be free from oxide and surface layers. The fit-up requirements are secondary. The beam must be powerful enough to penetrate a thickness equal to almost the total of the material gauges. Coating materials (zinc, etc.), which cannot escape from the overlapping area, present major problems and may lead to pores and other inclusions in the weld. This may be prevented by leaving a small gap (0.05 – 0.2 mm, respectively 0.002– 0.008 in) between the parts to be assembled. This gap allows for the coating to evaporate and escape from the weld zone so that seam quality is not affected. Two main failure modes are generally observed in overlap spot welded joints: a *plug type failure* (sheet failure) and an *interface failure* (nugget failure). From an optimum structural performance point of view, the plug type failure is the preferred

mode of failure because a stable fracture or shear takes place in one of the BM sheets and provides high deformation capacity.
In an edge flange weld, the parts to be welded are bent to provide a flange, which is then joined at the edge. Here again, good fit-up is crucial.

2.3 Laser Welding

2.3.1 The laser welding technologies

Within the last decade, industrial lasers have advanced from exotic to state-of-the art technology in many fields of manufacturing. While laser cutting is certainly the most popular application of high power lasers, other processes such as laser welding and laser surface modification are also becoming the process of choice in their respective industries. Laser welding is increasingly being used in industrial production ranging from microelectronics to shipbuilding. Automotive manufacturing, however, is among the industrial sectors which have proven to be most outstanding at developing applications that take advantage of the many benefits of this technology**.** The nature of the laser beam enables it to be irradiated on a very small spot on the substrate material, allowing the beam to achieve high power density to melt and join components. This type of welding process is particularly useful in cases where the localized heating is required.

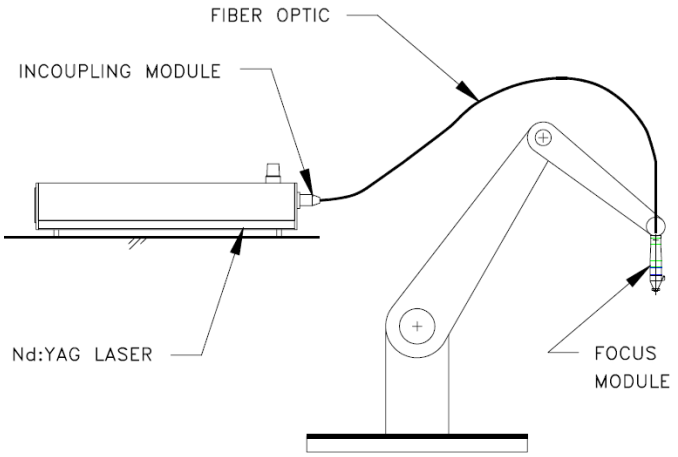

Figure 2.2: General scheme of Nd:YAG laser system with fiber optic beam delivery system

Moreover, Nd:YAG (neodymium-doped yttrium aluminum garnet; $Nd:Y_3Al_5O_{12}$) laser beam welding is a high power density welding process

which has the capability to focus the beam to a very small spot diameter of about 0.4 mm. This is favorable achieve the objectives listed above.
A Nd:YAG laser beam is typically divided in two types -continuous and impulse- defined according to the means of transferring energy. The laser used in this study was a continuous, diode-pumped laser. These kind of laser sources are optically pumped crystal-based devices, excited by a laser diode or an array of diodes instead of a flash-lamp. Systems can be either longitudinal- or side-pumped (**Fig. 2.3**), with Nd:YAG rod geometries [29].

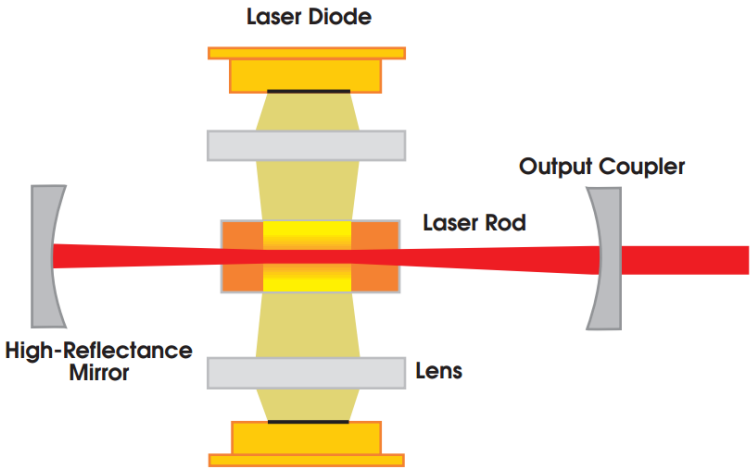

Figure 2.3: Scheme of a Nd:YAG laser source diode pumped (cylindrical rod type with side pumping)**.** Courtesy of Rofin-Sinar

Diode pumped rod lasers in the kW range are available on the market place as industrial product since the end of the past century. In the last years, the disk lasers and the fiber lasers, using laser diodes as a pump source, entered in the materials processing market.
The Rofin Sinar DY033 is an example of high power solid state laser. It possess six resonant cavities (six cylindrical Nd:YAG rods). In a high power laser typically the rod has a diameter of 4 to 8 mm, a length of 150 to 200 mm. They are placed in series (**Fig. 2.4**), increasing the maximum output laser power.

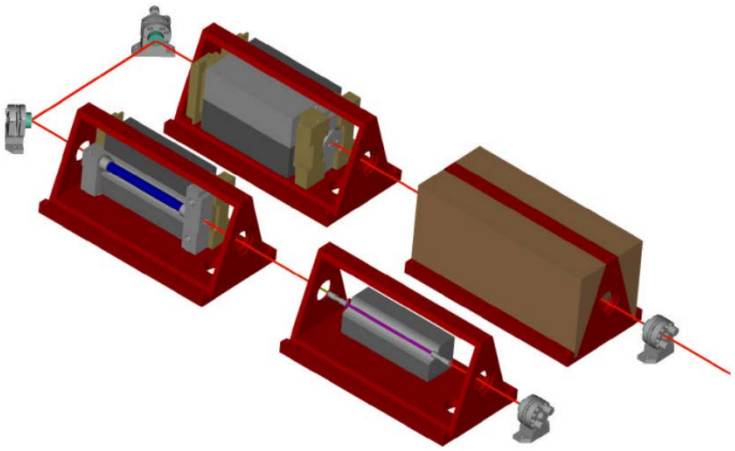

Figure 2.4: A four resonant cavities series within a Nd:YAG solid state laser source. Courtesy of Rofin-Sinar

A beam delivery system is comprised of components that accept the beam from the laser, direct it to the workpiece, and condition it into a useable form of energy. These generally include: beam bending mirrors, interconnecting beam guard tubes, and may include a beam collimator for moving beam or long beam delivery systems in a reflective system, or a coupling module, fiber optic cable and a collimator in a fiber optic delivery system. In addition, both systems require a focus module with a focusing optic, and a shield gas delivery nozzle. Focus modules that use a nozzle cone for shield gas delivery often provide the adjustments required to center the focused beam through the nozzle orifice. Nd:YAG focus modules typically use inexpensive, expendable glass cover slides to protect the focus optic from spatter and smoke from the welding process [29].
In general, the Nd:YAG laser wavelength is absorbed better than the CO_2 wavelength by most metals. The use of fiber optics for Nd:YAG beam delivery has taken the important consideration of flexibility into the realm of relatively low cost three-dimensional laser welding. The fiber optic beam delivery is useful especially when considering robot applications.
Compared to the CO_2 laser, a Nd:YAG laser provides an easy beam alignment, beam switching and beam sharing. A solid state laser source possess a less extensive and simpler maintenance and less floor space for the equipment [29]

2.3.2 The laser welding process for automotive applications

Nowadays, laser spot welding is widely recognized as an important modern joining technology, especially in the field of industrial manufacturing applications.
There are two main methods of laser welding: conduction mode welding where the heat is transferred from the surface into the material by thermal conduction; keyhole welding where the laser beam energy is transferred deep into the material via a cavity filled with metal vapor.
The conduction mode welding is typical of low-power lasers (< 500 W) where power density is normally not sufficient to create a keyhole. The resulting weld is characterized by a relatively wide and shallow profile.
High-power laser welding is characterized by keyhole welding. The laser beam, with a radius of 400 µm (Nd:YAG), illuminates the surface sheet inducing the fusion of the zone to assembly. Because of very high energy density in laser, the material will be vaporized quickly. This vaporization will be accompanied by a recoil pressure, which will push the liquid, inducing a deformation and the appearance of the keyhole, a vapor capillary. To realize the welded joint, the laser beam is moved at a speed which ensures the minimum energy input for the keyhole stability. This speed is function of the laser power and the sheet metal thickness.

Design for laser welding is continuing to make its place in the fabrication of car bodies. The advantages of using laser welding over other conventional welding technologies are the generation of high weld bead depth-to-width ratio, low distortion and narrow Heat Affected Zone (HAZ) [48]. Thanks to the low heat input associated with the laser welding process it is possible to reduce or eliminate post process rework or straightening.
Independent of robot speed, precise weld shapes can be used in the joining of components. With a flexible laser welding process, short lines, circles, C-shaped welds can be arranged (in terms of size and orientation) to optimise weight and strength of the welded assembly. This is possible by choosing the solution with the best flow of stresses (**Fig. 2.5**).

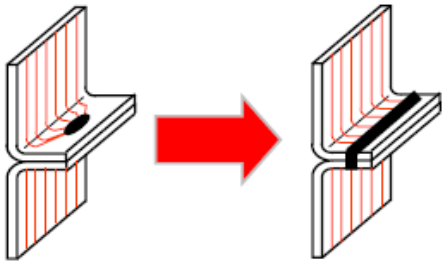

Figure 2.5: Joint strength improvement due to uniform stress flow distribution [54]

Though linear welds require significantly less flange width than a resistance spot weld resulting in a material saving and weight reduction (**Fig. 2.6**).

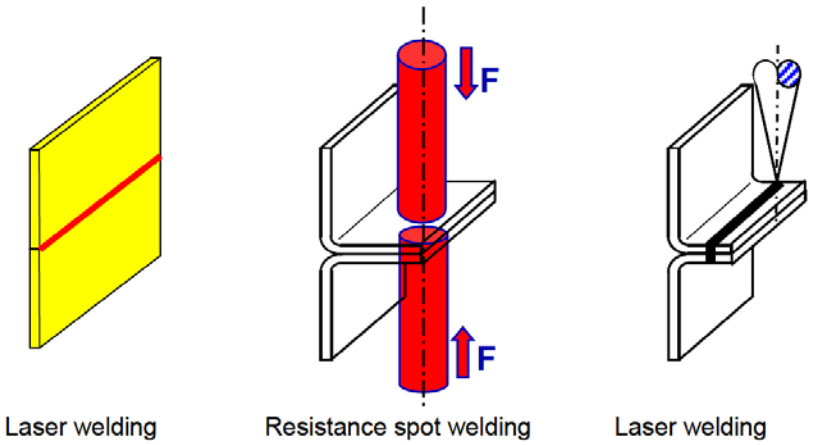

Figure 2.6: Example of a flange reduction or elimination using laser welding compared to resistance spot welding process [54]

Furthermore the single sided access of the laser welding technique provides another advantage compared to resistance spot welding that needs a double sided access for the electrodes. Closed cross sections, such as tubes and profiles used for frames, are much more rigid compared to open sections and formed sheet metal. Thus, by assembling profiles with closed section it is expected an increasing in the overall structure strength resulting in a reduction of weight and cost (**Fig.2.7**).

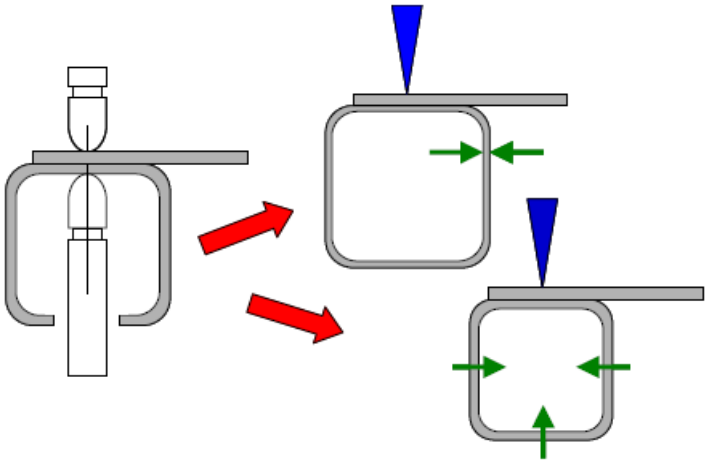

Figure 2.7: Single side access in laser welding can reduce weight and increase strength compared to resistance spot welded components [54]

A greatest advantages in costs and productivity compared to resistance spot welding can be achieved. The laser welding process reduces the RSW cycle time which is approximately one second.
Another thing that can be done to maximize "beam on" time is to utilize a remote welding process with a scanner optic device. The highly dynamic scanning mirrors enable extremely fast indexing in-between welds, which simply means the laser is spending more time joining parts and much less time waiting to be in position to create the next weld. The results are higher throughput, less stations and lower costs.
Hybrid processes involving a combination of laser and MIG arc welding are being developed reducing the most critical aspects of laser welding: the fit-up and fixture requirements on the parts to be joined. Unfortunately, this solution is not available in the case of laser remote scanner welding.

2.4 Resistance Spot welding

2.4.1 The resistance spot welding technologies

This kind of welding is only suitable for joining thin-gauge sheets in overlapping configuration.

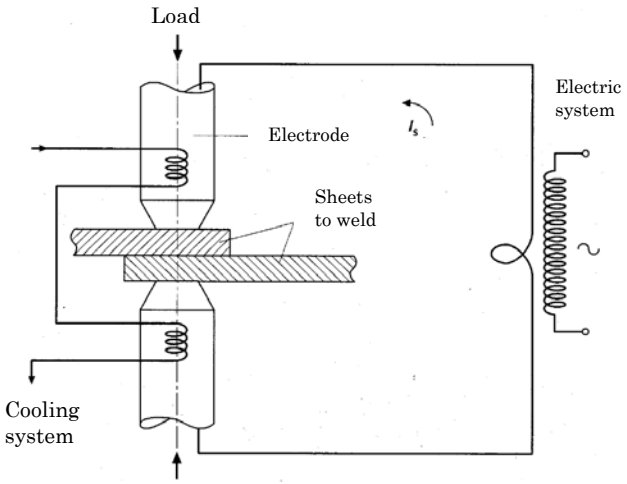

Figure 2.8: General scheme of resistance spot welding system

The heat supply in resistance welding processes is produced by the passage of a high current (several kA), which causes melting at the interface of the sheets to be welded. The current is applied via copper contacts or electrodes, which usually take the form of wheels in the case of continuous (seam) welding, pressed against the assembly to be welded. The processes usually

employed using this principle are resistance spot welding, resistance seam welding, projection welding, resistance and flash butt welding.
From the microstructural perspective of the weld, a columnar-to-equiaxed transition (CET) is generally observed in resistance spot welds. The size and shape of the columnar and equiaxed regions depend on factors such as cooling rate, temperature gradient and the nature of inoculant particles. Nevertheless, resistance spot welding (RSW) is still the predominant joining technique in automobile body assembly lines for its reliability even with less fit-up and fixture requirements.

2.4.2 The resistance spot welding process

Nowadays 70 % of the welds in the automotive field is carried out by resistance spot welding. Each car possess 2000-5000 spot welds.

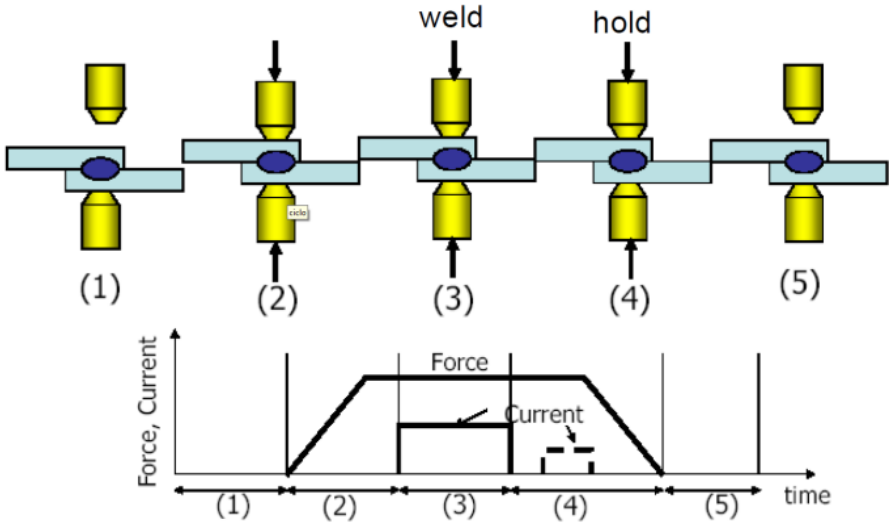

Figure 2.9: The resistance welding spot process cycle

The resistance spot welding process includes interacting processes such as mechanical loading, resistance heating, rapid thermal changes and metallurgical phase changes (**Fig. 2.9**). Among these the mechanical loading starts from a clamping force at the start of the process (2). This is followed by heat initiated volume changes resulting from thermal gradients. Once the temperature crosses the transition range, phase changes also begin to contribute to the volume changes during heating (3), subsequent holding (4) and cooling stages (5). It is important to note that different regions of the workpiece undergo these transitions at different points of time, while thermal diffusion between the interacting parts and within the workpiece happen throughout the process.

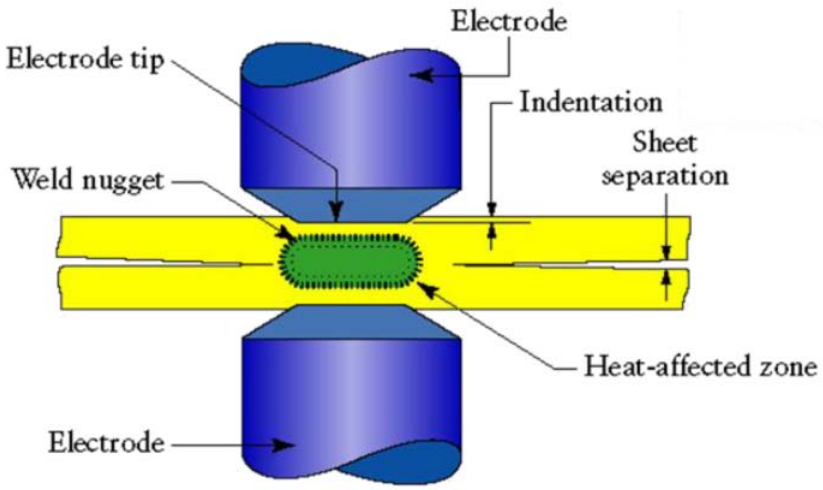

Figure 2.10: Resistance spot welded joint structure

The advantages of this welding technique are the high production rates (lower than laser welding), the process is easily automated with low skill levels. The welding results have good repeatability and reliability. Moreover the filler is not required.
On the other hand, a very limited number of weld configurations are possible (lap).
The main disadvantage of the RSW approach is its inherent inflexibility in adapting to new vehicle program changes without significant modifications of the equipment. Due to the rapidity of present vehicle model change, the manufacturing process, system design and construction need to be accelerated to respond to the fast-to-market drive.
Resistance spot welding is a double sided access process, thus is not possible to join close section components. Moreover, comparing to RSW, LBW has the advantages of high welding speed and precision while providing consistent weld integrity and low heat process which yields reduced distortion. Unlike RSW, laser spot welding can be used as a single side, non-contact process. As a result, LBW is becoming a very attractive joining method for automotive mass production.

3 State of art

In literature the weldability and the optimization of magnesium alloy sheet are well discussed. The AZ31B magnesium alloy laser welded joints are discussed within 18 papers using several heat source (hybrid, Nd:YAG, CO_2, diode, fiber lasers) in different joints configuration (butt, overlap, lap fillet joints). In literature is not found a mechanical characterization of overlap single laser welding joints in case of AZ31B. Moreover, any comparisons between laser beam overlap joints and resistance spot welding technologies is missing for magnesium alloy sheet. The few papers, concerning this topic, are focused on different materials like high strength steels for automotive applications.

3.1 Laser Welding of Magnesium alloys

In general, magnesium alloy welding has been documented for the different welding techniques (TIG, MIG). However, the relative laser weldability of magnesium alloys has not been methodically investigated.
The first researches into stable laser welding has involved identifying and controlling the processing parameters to produce defect-free welds. Because of this butt joints and bead-on-plate welding configurations were commonly investigated. On the other hand laser welded overlap joints and their mechanical properties have rarely been studied.
It is well known how the efficiency of laser welding depends mainly on the interaction between the laser beam and the material to be welded. Magnesium alloys are highly susceptible to oxidation and possess low absorptivity of laser beams, high thermal conductivity, high coefficient of thermal expansion, low melting and boiling temperatures, high solidification shrinkage, low viscosity and low surface tensions (Section 2.1). Because of this physical properties some processing problems can be encountered during the laser welding process as unstable welding pool, substantial splatter, a strong tendency to drop-through in case of keyhole welding mode, porous oxide inclusions, loss of alloying elements, cracking and an pore formation (particularly for untreated surfaces).
Nevertheless, crack-free laser welded joints, with low porosity and good surface quality, can be achieved for wrought magnesium alloys using appropriate surface preparation of the joint and laser processing conditions.
Three main types of lasers, CO_2, Nd:YAG and Fiber laser, have been usually used to investigate the weldability of magnesium alloys.
In the past years, the CO_2 laser has been largely used due to its high power output. However, thanks to the possibility of fiber delivery, that increases

the flexibility of the processes, the Nd:YAG and the Fiber laser are challenging the dominating CO_2 laser.
With the recent high output power of the modular Fiber laser and thanks to its electrical efficiency and high beam quality, the Fiber laser source development is taking place.
Wavelength effects generally include laser beam absorption on the substrate surface and loss of laser beam absorption due to the plasma plume. For metals, laser beam absorption on the substrate surface generally increases with a shorter wavelength [4]. At the Nd:YAG wavelength (1.06μm), the laser beam has less tendency to form plasma than a CO_2 laser. Unlike the Nd:YAG, fiber or disk laser beams, the CO_2 beam is absorbed in its own plasma. This allows the Nd:YAG source to be more flexible regarding the shielding gas used.
The better weldability magnesium alloys with the Nd:YAG laser is proved and it is due to its shorter wavelength, which in turn reduces the keyhole threshold irradiance and produces a more stable weld pool [2]. For instance, for a 1.5 kW laser beam with a similar spot diameter and welding speed (5m/min), a penetration depth of 2 mm was achieved for a Nd:YAG laser as compared to only 0.7 mm for the CO_2 laser [49].
Pierron et al. [26] stated that the absorptivity for a Nd:YAG laser beam was 20-30% at room temperature, but nearly 90% when the keyhole is stabilized.
In addition to the used laser source many other parameters may influence the laser welding process.
Regarding to the focal plane, for 3mm AZ91 welded using a 3000 W Nd:YAG laser, the best focal position is approximately 0.8mm below the workpiece surface, with a tolerance of ±0.5 mm [2].
At different levels of laser power the penetration depth and weld width both decrease linearly with increasing welding speed [29].
Moreover, though similar welding parameters are used, various magnesium alloys exhibit different welding performance due to their different thermophysical properties. The surface condition of magnesium alloys may influence the energy absorption of laser beams as well as the threshold power density for keyhole welding. Furthermore, a MgO surface films or contaminants on magnesium alloys sheets can cause weld crack and porosity [2]. Thus, it is preferable to clean all surfaces and edges of the workpiece to remove such oxides and grease before the welding.
After the laser welding process, the microstructure of the magnesium alloys welds is the typical microstructure from a high-speed process in which heat is rapidly extracted from the molten fusion zone.
The rapid cooling experienced during laser welding leads to significant grain refinement in the fusion zone. If the thermal gradient is relatively large (high cooling rate) the grains are finer at the fusion boundary and the microstructure will be predominantly cellular.

The grain coarsening occurs with low cooling rate, for example due to a large energy input in the workpiece. The growth direction is perpendicular to the isotherm curves.
If the alloy is susceptible to grain growth, the grains will grow in the HAZ with consequently decreased mechanical properties. The grain growth was observed in the HAZ of laser welded AZ31B joints, especially at slow speeds [2].
Sun et al. [31] compared TIG and laser welding (CO_2 and pulsed Nd:YAG lasers) of AZ31 sheets. It was found that laser welding could obtain finer grains than the TIG welding.

3.1.1 Laser welding process for AZ31B in literature

In the last years, researchers have investigated the microstructure and properties of laser beam welded AZ31 magnesium alloy joints fabricated in various joint configurations under different welding parameters [3-7, 17-20].

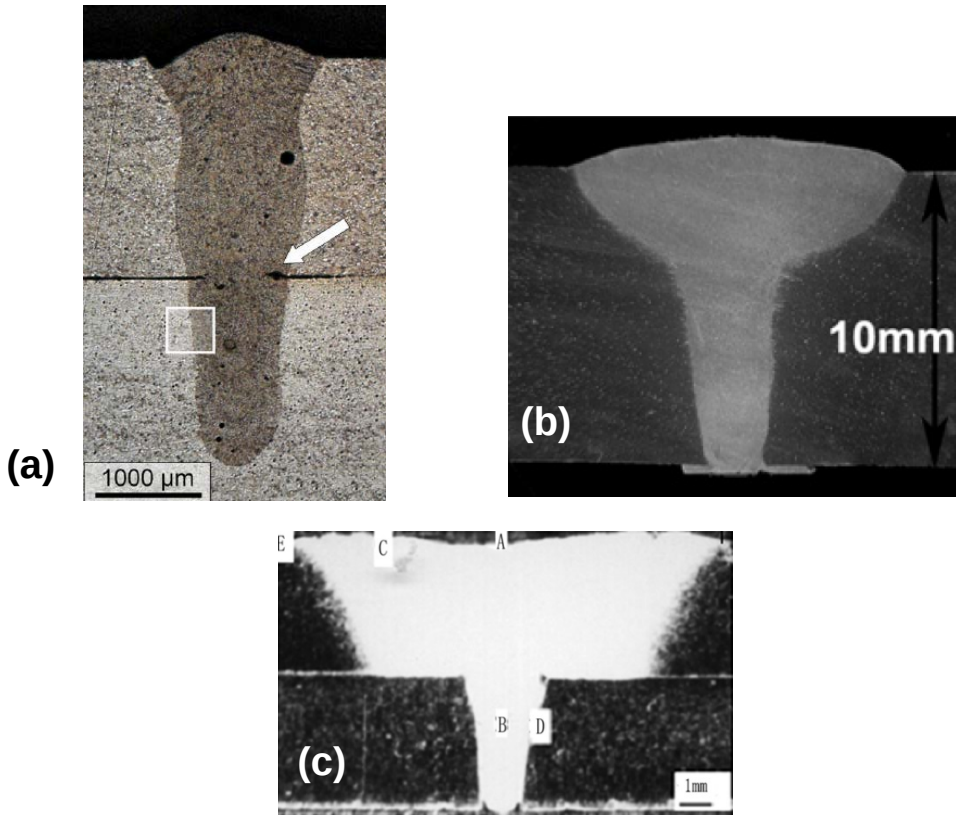

Figure 3.1: Cross section of the weld bead of AZ31B Mg alloy using: Nd:YAG source (a)-[20], CO_2+MIG hybrid source (b)-[25] and Nd:YAG+TIG hybrid source (c)-[21]

Zhu et al. [3] analysed the effect of the beam spot size on the quality of AZ31B-24H welds using different welding modes – such as keyhole welding with a CO_2 laser and heat conduction welding with both CO_2 and diode lasers for bead-on-plate welds. Hiraga et al. investigated the effects of the shielding gas and laser wavelength (Nd:YAG, CO_2) for the bead-on-plate welding of AZ31B sheets [4]. Many studies focused on the microstructure and mechanical properties of AZ31B laser (CO_2, Nd:YAG, Fibre laser) welds in the butt joint configuration [5-7, 17, 18]. Coelho et al. [20] investigated the microstructure of laser beam welded overlap joints between AZ31 sheets and AZ31 extruded profiles; however, the mechanical performance of these joints was not considered.

Year	Author	Source	Joint config.	Topic
2005	**Song**	Hybrid (YAG+TIG)	Overlap	
2001	**Hiraga**	Nd:YAG and CO_2	Bead On Plate	
2005	**Liu**	Hybrid (YAG+TIG)	Butt Joints	Pores formation
2005	**Zhu**	CO_2, diode	Bead On Plate	Weldability
2008	**Coelho**	Nd:YAG	Butt Joints	
2008	**Quan**	CO_2	Butt Joints	Microstructure and tensile properties
2008	**Coelho [20]**	Nd:YAG	Overlap	Microstructure
2009	**Liang [21]**	Hybrid (YAG+TIG)	Overlap	
2010	**Scintilla**	Nd:YAG	Butt Joints	Weldability
2011	**Padmanaban**	CO_2	Butt Joints	Tensile properties
2011	**Wang**	Fiber laser	Butt Joints	
2012	**Lin**	CO_2	Bead On Plate	
2012	**Gao [25]**	Hybrid (CO_2+MIG)	Butt Joints	
1999	**Leong**	CO2, Nd:YAG	Butt Joints	Weldability

Year	Author	Source	Joint config.	Topic
2004	**Pan**	Nd:YAG	Butt Joints	Optimization
2004	**Kim**	Hybrid (YAG+TIG)	Butt Joints	Tensile properties
2011	**Chowdhury**	Fiber laser, Diode	Butt Joints	Microstructure and mechanical properties
2012	**Ishak**	Nd YAG	Fillet Lap configuration	Weldability

Table 3.1: Summary of the papers found in literature about Hybrid or single Laser beam welding for AZ31 Magnesium alloy under different joint configurations

Some research concerning the performance of AZ31B Mg alloy overlap joints was conducted with a laser-arc hybrid heat source [21-22, 25] to enhance the absorption of the laser energy.
A good overlap joint of Magnesium AZ31B sheets, was achieved by adopting laser-TIG hybrid heat source welding [21]. Song, Liu et al. produced lap autogenously welds on 1.6- to 2.5-mm thick using a pulse YAG laser combined with GTAW process [22, 46]. Ren et al. studied laser weld bonding overlap joining of AZ61 magnesium alloy, investigating the synergistic effect of the laser welding and the adhesive bonding [24] .
Only a few researches were carried out comparing different laser welding paths (circular, C-shape, linear) to improve the mechanical performance of the overlap joints, but in the case of steel sheets [11, 13, 14, 45].
Nevertheless, microstructure and mechanical properties of such laser welded Mg alloy overlap joints have rarely been studied. This means that the feasibility of this AZ31B Mg alloy joints has to be proved yet.

3.1.2 Typical defects of laser welded Mg alloy sheets

The welding result depends on the laser process parameters. If the laser parameters, such as welding speed, focal plane position, laser power and shielding gas condition, are not optimized various defects can be observed.
Some typical defects laser welding defects are shown in the following **Fig. 3.2.**

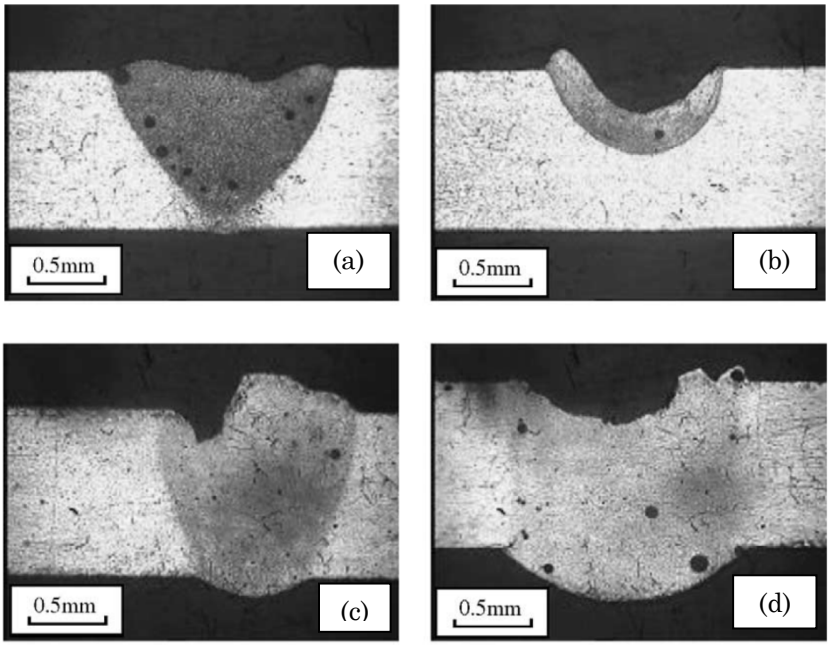

Figure 3.2: Typical defects in AZ31 laser welds [3]: porosity (a), vaporization (b), side-blow (c), weld drop-out (d)

Porosity

The natural surfaces of Mg alloys are usually covered with an oxide film (MgO) due to its high reactivity with oxygen, especially over extended periods of time. Otherwise, the sheet surfaces are dirtied by oil coating or chromate conversion coating for protection during the storage.

It is well known how the surface contamination enhances the presence of porosity in the weld [27]. The issues due to the collapse of the keyhole and the turbulent flow in the weld pool could also be linked to porosity formation [9]. Anyway, magnesium alloys possess more stable keyhole due to a high equilibrium vapor pressure and low boiling temperature [28].

The pores were located mainly around the fusion boundary, indicating that entrapment of gases try to exit at the interface between the two sheet in the overlap joint.

The presence of hydrogen, depending on the surface preparation of base material, is another cause of gas porosity in magnesium alloys welding [2].

L. Liu et al found that during hybrid laser-TIG welding of AZ31B magnesium alloys the hydrogen do not play a significant role in porosity formation and the pores are macropores, which are mainly located in a line. It is proved that air enters into the molten pool and forms large quantity pores when the laser beam cannot be shielded by inert gas [27].

Weisheit et al. [32] tested CO_2 laser welding of different Mg alloys. The results showed that most alloys used could be welded easily without serious

defects. Just in the QE22 cracks occur and AZ91, AM60 have high porosity issues.
J. Zhu e al. [3] studied the keyhole welding with the CO_2 laser and conduction welding with the diode laser on a AZ31B-24H magnesium alloy. The bead on plate welds showed the followings defects: weld drop-out, under-cut, craters and cracks.

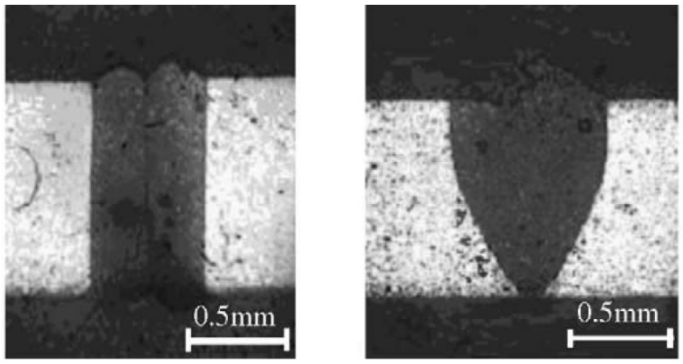

Figure 3.3: CO_2 laser welding with (a) central under-cut weld, (b) surface irregularity [3]

Weld drop-out
When the laser energy input was higher than required for a full penetration weld dropout would occur. While the low viscosity liquid is not able to sustain the welding pool. This problem could be overcome by selecting the appropriate welding energy input by calibrating the correct ratio of laser power to speed [8]. The P/v ratio is the Energy input per linear unit (E [J/mm]), representing the heat input on the workpiece.

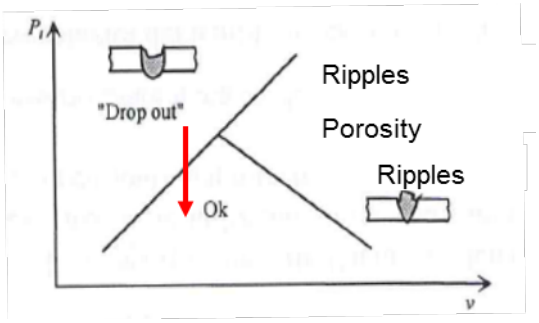

Figure 3.4: The graph represents the correct combination of the process parameters P (laser power) and v (welding speed) [8]

A slight decrease in the laser power values is preferred to eliminate the drop-out defects [8] and reduce inner porosity [9].

Under-cut
In laser keyhole welding there is a large gradient of temperature within the weld pool even at low power. The narrow temperature range between boiling and melting points of magnesium allows the presence of under-cut because of the material vaporization. Defocusing is an effective way to avoid this defect because the density power distribution results more uniform on the workpiece .

Cracks
The oxides weaken the components if incorporated into the weld pool, where solidification cracks would initiate. For the magnesium alloys, an increase in alloying elements could increase the solidification temperature range. Moreover, the large solidification shrinkage of the magnesium and the low melting point of the intermetallic constituents make magnesium alloys exposed to solidification cracking in FZ and HAZ liquation cracking [30].

Craters
Typical craters on the top bead surface may occur because of the vaporisation and fast cooling. Magnesium is susceptible to vaporisation during both keyhole and conduction welding because of its low boiling point. The strong vaporisation can be reduced by defocusing the laser beam but it is inevitable.

3.1.3 Shielding gas effects

Magnesium has a strong tendency to oxidize, thus inert gases protection is required. The gas shielding can both avoid burning and protect the optics from metal spatter.
Shielding gas configuration, its flow rate and composition affect in different way the weld zone oxidation and weld bead profile. The shielding gas configuration (coaxial, one side, gas box) could have a significant effect on the surface weld quality.
If the gas flow is too weak, there would be insufficient weld protection, while if the gas flow is strong it would cause defects or disturb the bead surface [4].
The most used gases during laser welding of magnesium alloys are helium, argon and nitrogen. Helium provides the best results in terms of surface roughness, penetration depth and seam shape factor (depth/width). This is because the shielding gas also influences the formation of the plasma. Argon is heavier than air so it provides a better shield than helium, but it ionizes easily. Helium has a ionization potential of 24.5 eV (15.8 eV for the

argon) and possess a good thermal conductivity [33]. This causes a problem with CO_2 welding: the metal vapor from the keyhole is partially ionized, with charged atoms and free electrons. The free electrons absorb some of the laser light, reducing the power available for the welding [19]. Less plasma is produced using helium.
In the case of Nd:YAG laser source, the wavelength is shorter than the CO_2 one and the argon on the upper surface is sufficient to produce sound beads without back shielding. Nd:YAG laser has less tendency to form plasma, thus the lower ionization potential of the argon is not a problem.
The tensile strength of CO_2 laser welded joints are more affected by the different shielding conditions regarding to Nd:YAG joints. Moreover the Nd:YAG source, being equal the other parameters, provides a higher and more stable strength regardless of shielding conditions [4].
Weisheit et al. [32] investigated the effectiveness of the mentioned three shielding gases and confirmed that helium was the best choice.
Hiraga et al. [4], studied 1.7 mm thick AZ31B-H24 butt joints and achieved some improvements using argon back shielding in addition to the helium centre shielding. Moreover it was investigated the effects of the laser wavelength (Nd:YAG, CO_2): the high-speed camera showed how Nd:YAG laser forms very little plasma. The effect due to plasma plume formation also amounts to a loss of effective laser power through absorption due to reverse bremsstrahlung. The absorption coefficient due to reverse bremsstrahlung for an electromagnetic wave is proportional to

$$N_e \times N_i \times \omega^{-2} \times T^{-3/2} \qquad \text{(Eq. 3.1)}$$

The CO_2 laser (λ=10.6 μm) possesses lower frequency than the Nd:YAG laser (λ=1.06 μm), resulting in two places higer absorption. Thus in the case of Nd:YAG laser the beam absorption by the plasma plume is 10^{-2} times less than CO_2 laser welding and the plasma plume formation due to reverse bremsstrahlung does not occur easily.
Moreover, the pressure due to expansion of the generated plasma induce reaction force to the molten material. This is a problem because magnesium is well known as low viscosity material with low surface tension in fluid form.
In the Nd:YAG welding experiments from Hiraga et al. [4], the metal vapour not converted into plasma provide a protective shield against ambient air and prevents bead oxidation (**Fig. 3.5**).

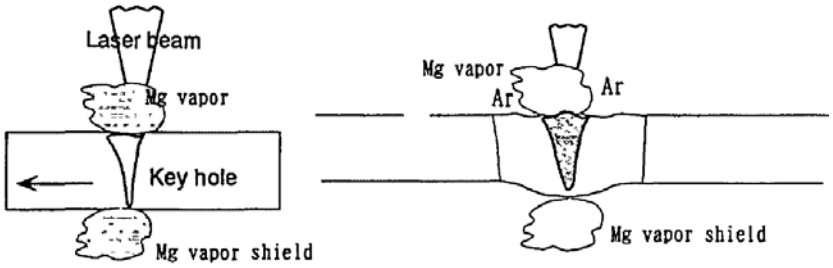

Figure 3.5: Nd:YAG laser welding, centre gas Ar, without back shielding [4]

The results obtained from Hiraga et al. [4] during the EPMA analysis of microparticles adhering to the bead back show that, during vaporisation, the magnesium is itself oxidised due to the reaction with ambient oxygen. This study prove how the Mg metal vapour generated during the welding process providing adequate protective shielding (**Fig. 3.5**) against enviroment, to prevent bead oxidation. Thus, sufficiently high tensile strength is achieved.

3.2 Resistance Spot Welding of wrought Mg alloy sheets

To date, the majority of studies of the mechanical performances of RSW have been on steel and aluminum alloys. That is because these material are predominant in the automotive applications.
Only a few studies report the microstructures and tensile shear properties of resistance spot welded AZ31B magnesium alloy joints [38, 42]. Generally, the microstructure of Mg spot welds includes both columnar dendritic and equiaxed dendritic structures.
The weld nugget diameter and tensile shear strength of joints welded by RSW with cover plates were measured in the study of Qiu et al. The used Mg alloy AZ31B sheets were 1.2 mm thick [39, 41].
Liu et al. [34] analysed the tensile properties, the fracture toughness (K_C) and microstructures in resistance spot welding of AZ31 magnesium alloys from two different suppliers. Xiao et al. [36] studied the fatigue life of the joint achieved from the same two groups of suppliers. Two different failure modes were identified under cyclic loads: interfacial and through thickness failure.

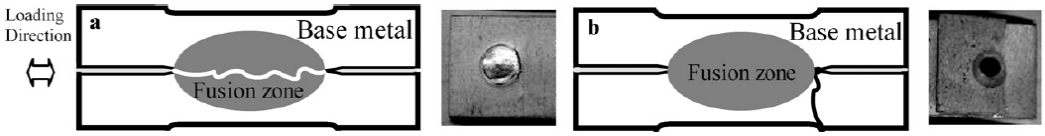

Figure 3.6: Schematic illustration of failure mode (a) interfacial failure at a higher level of cyclic load range and (b) through thickness failure at a lower level of cyclic load range

S. B. Behravesh et al. [24] provided a systematical characterization of spot welds under both tensile and cyclic loading for AZ31B-H24. The specimens in this study were made from 2 mm thick sheets. They were produced by hot rolling followed by annealing to half of the initial hardness. Five sets of spot weld specimens were prepared, utilizing different welding parameters. The resistance spot welds of the magnesium alloy were also characterized in terms of microstructure and hardness. The results of this work were used as a reference (see **Section 7.1**) for the mechanical characterization of the LBWs and RSWs prepared respectively at the Helmholtz-Geesthacht Zentrum and at the STADCO Saarlouis plant.
To the best of the author's knowledge there are no other works on the fatigue of magnesium resistance spot welds.
Hayat et al. [37] investigated the effects of the RSW parameters on the mechanical properties on joints with Mg/Al dissimilar materials. Hassanifard et al. [35], studying the fatigue life behaviour of aluminium alloy spot welded joints, investigated the effects of the gap distance between the two sheets. It was found that smaller gaps predict the shorter fatigue life for the joints, because the small distance can behave as a sharp crack.

3.3 Comparison between Laser Beam Welding and conventional Resistance Spot Welding of AZ31B Magnesium alloy

To achieve the role as a major material in automotive manufacturing, a methodological investigation of the mechanical performance for magnesium alloy joints is necessary. It is therefore essential to examine the merits of welds made of magnesium under both static and cyclic loads.
The only work that studies of AZ31B laser overlap joints to replace the most established joining process in car industry were from Coelho et al. [20]. The characterization of the joint concerns only the hardness and the residual stresses analysis. While a direct comparison between RSW and LBW in terms of the mechanical properties of the joints was not found in literature.
Other works make a comparison regarding fatigue and tensile behaviour of laser overlap joints, but just in the case of steel sheets [11, 13, 14, 45].

4 Aims of the work

In automotive manufacturing, laser beam welding is concurring to resistance spot welding due to its high process flexibility and efficiency.
The study will offer an in-depth comparison between the two welding processes: the resistant spot welding (RSW) being the reference state of the art of the industrial practice and the laser welding, the new competitor, when a common magnesium alloy, AZ31B, is the investigated material.

The aim of this work will be to develop a process for laser short distance welding overlap joints of 2.5 mm thick Mg AZ31B sheets.
The welding defect formation will be studied optimising the laser process parameters at the Helmholtz-Zentrum Geesthacht. A 3.3 kW Nd:YAG laser will be used for the welding experiments, and the design of experiment approach will be applied.
Both mechanical testing and advanced metallurgical examinations will be used to establish the process-property-performance relationship of the overlap joints. The micro-hardness, shear tensile and fatigue tests will be implemented for the mechanical performances investigation.

To improve the fatigue behaviour, different joint geometries (linear, circular and C-shape) will be investigated. It is expected to develop an empirical model that will provide the relation between the main laser process parameters and the quality of the welds, depending on the geometry of joints employed.

After this, a mechanical characterisation of these joints will be done. In detail, using the regression analysis principles, L-N curves will be plotted to describe the LBW fatigue behaviour compared with the traditional resistance spot welded joints.

5 Methodologies

The design of experiment (DOE) and analysis of variance (ANOVA) principles were used in the first screening experiments to define the feasibility of the process parameters.
In any experiment response variables can be found to be affected by a number of factors in the overall system some of which can be controlled during the experiment. An experiment in which the treatments consist of all possible combinations of the selected levels in two or more factors is referred as a factorial experiment.
Well designed experiments can reduce the risk of coming to an incorrect conclusion during a process characterization or process validation study. The primary goal is usually to extract the maximum amount of information regarding the factors from as few observations as possible. Typically, design of experiments can be categorized into two classes: screening designs and optimization designs.

Within the factorial plans, the 2^k designs are the most used as first screening experimental designs. The 2^k refers to designs with k factors where each factor has just two levels. These designs are created to explore a large number of factors, with each factor having the minimal number of levels, just two. By screening we are referring to the process of screening a large number of factors that might be important in the experimental factors range of interest. The goal is to select the important ones for the measured response variable, within the factors range of interest.

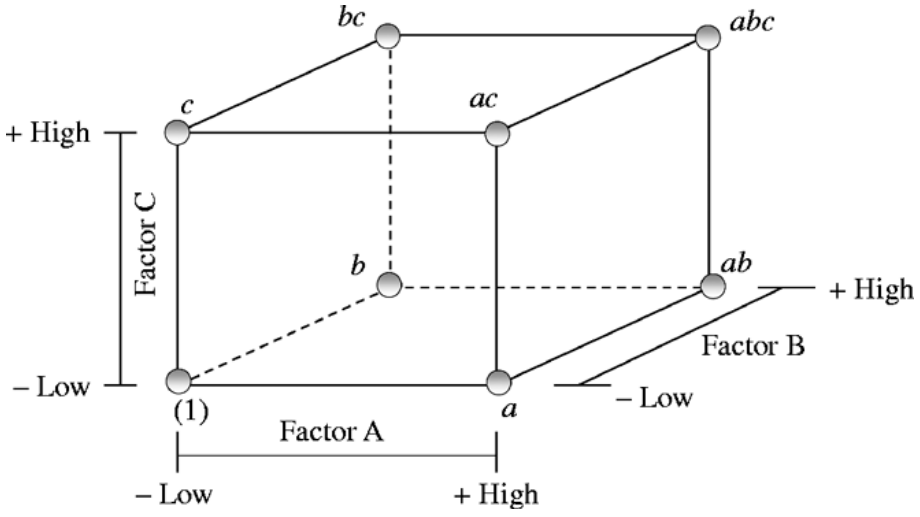

Figure 5.1: The 2^3 factorial design [55]

Table 5.1: Design matrix for 2^3 factorial plan [55]

Run	Factor A	B	C	Label
1	−	−	−	(1)
2	+	−	−	*a*
3	−	+	−	*b*
4	+	+	−	*ab*
5	−	−	+	*c*
6	+	−	+	*ac*
7	−	+	+	*bc*
8	+	+	+	*abc*

The total number of treatments in a full factorial experiment is the product of the number of levels of each factor; in the 2^3 factorial example, the number of treatments is 2 x 2 x 2 = 8 runs. Thus, as the number of the investigated factors increases, the complete set of treatments (full factorial design) is replaced by a fractional factorial design (FFD). While a complete factorial experiment means that all the combinations of the selected factors levels are included in the tests, the term fractional factorial experiment is used when only a fraction of all the combinations is tested.
For instance a 2^{3-1} FFD refers to a 2^3 factorial design where only a half of the totality of all possible treatment combinations are tested (8/2= 4 runs).
The chosen combinations fraction depends on the identity relationship (or defining contrast relation) for example written as I=ABC. Given the identity relationship, it is possible to get the alias structure of each factorial effect interpreting I as unity and multiplying each effect on both sides of the identity relationship and deleting any letter whose power is two.

$A = A(ABC) = A^2BC = BC$

$B = B(ABC) = AB^2C = AC$

$C = C(ABC) = ABC^2 = AB$

In this example, the equality sign between the two factorial effects is to be interpreted as "aliased with". The aliased effects will be indistinguishable from one another regarding the variation of the response variable.
The resolution of the experimental design refers to the "aliasing structure" and is given by the length of the shortest "word" in the identity relationship[55]. For example, a fractional factorial plan with Resolution IV means that the main effect is aliased with 3-order interactions and the 2-order interactions aliased with other 2-order.

One of the simplest statistical method to determine if a relationship exists between the response variable is the linear regression analysis. It is sometimes referred to as correlation analysis, which is the statistical tool used to describe the degree to which one variable (response variable Y) is linearly related to another (X). The correlation coefficient assesses the strength of the relationship between X and Y. The correlation coefficient ranges from –1 to 1, with 1 being a strong positive correlation and –1 being a strong negative correlation.
The regression analysis was used for both screening experiments results in terms of the DoP variable (see Section 8.2.1) and fatigue testing results. The L-N curves were plotted, according to the standards [15], to compare these results to those for the state-of-art resistance spot welds.
In this case the ANOVA analysis helped to understand which were the significant predictors to insert in the regression model. If the P-value for the F statistic is very small ($p<0.05$), so we would conclude that at least one of the input variables (X) is a nonzero regression coefficient.
Another important parameter is the R^2. It is a measure of the amount of reduction in the variability of Y obtained by using the regressor variables (X) in the model.
However, a large value of R^2 does not necessarily imply that the regression model is a good one. Adding a variable to the model will always increase R^2 regardless of whether the additional variable is statistically significant or not. Thus it is possible for models that have large values of R^2 to yield poor predictions of new observations or estimates of the mean response.
Because R^2 always increases as we add terms to the model, some regression model builders prefer to use an adjusted R^2 statistic. In general, the adjusted R^2 statistic will not always increase as variables are added to the model. In fact, if unnecessary terms are added, the value of R^2_{adj} will often decrease.

6 Experimental equipment

The laboratory equipment provided by the Helmholtz-Zentrum Geesthacht and used during the experimental work is presented. A presentation for the laser welding system, the robot and the full mechanical test machines is given. The characteristics of the microstructure and chemical analysis equipment are shown. Therefore optical microscope, SEM, EDX, EBSD and the X-ray analysis measuring parameters are discussed.

6.1 Laser System, KUKA robot and weld joint configuration

The laser system used was based on a Nd:YAG solid state laser source, a laser head, the shielding gas adduction system as well as the transport fiber to transfer the laser radiation from the source to the laser head.
The laser used was a diode pumped Nd:YAG laser (Rofin Sinar DY033 **Fig.6.1**) with a maximum output power of 3.3 kW. The beam was led through a 400 µm diameter fiber to a six-axis robot and focused with a 200 mm focal length optic. The collimation lens had a focal length of 200 mm, too. Therefore, the beam spot at the focus was approximately 0.4 mm in diameter.

Figure 6.1: Rofin Sinar DY033 Nd:YAG laser source with control panel

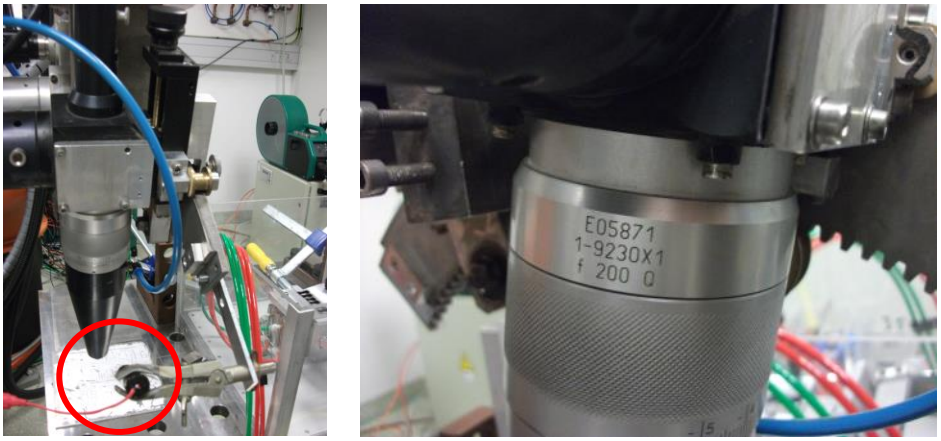

Figure 6.2: Laser head with the blue pipe for the coaxial shielding gas adduction and green laser selected with the red circle

In **Fig. 6.2** is shown also the green laser device fixed on the laser head to ensure the focus plane position regarding to the work piece surface. The positioning system used the triangulation between the green laser beam and the camera installed coaxially above the laser head.

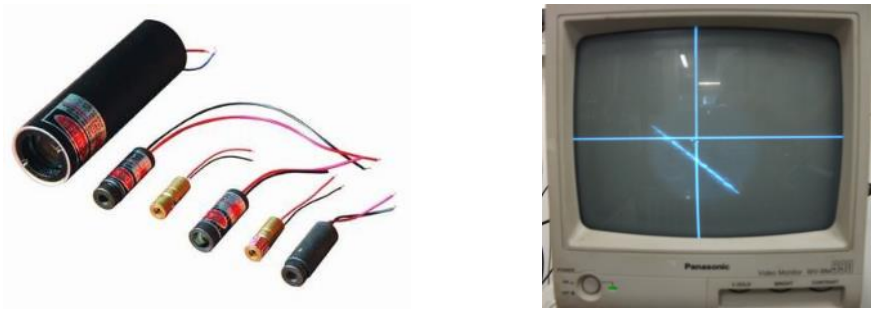

Figure 6.3: Examples of the green laser used for the laser head positioning and the online image from the coaxial camera

Table 6.1: Nd:YAG laser system characteristics

Laser Source	Nd:YAG Rofin Sinar DY033
Max output power	3.3 kW
Fiber diameter	400 µm
Focal lens	200 mm
Collimation lens	200 mm

The used robot, KUKA KR 30 HA (high accuracy), is an industrial 6 axis robot arm, with 30kg of load capacity, particularly suitable for laser applications [W1]. The repeatability declared of the robot is better than ±0,05 mm (**Fig. 6.4**).

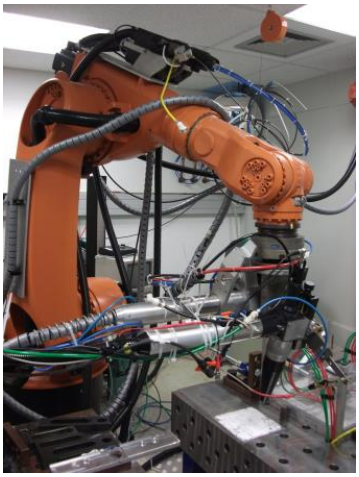

Figure 6.4: KUKA KR 30 HA with the installed laser head

It is well known that magnesium is highly susceptible to oxidation and thereby elaborate protection from the atmosphere is required. Because of this the laser welding of Magnesium AZ31B commonly uses an inert gas as a shielding gas [2,4]. An EL-Flow Bronkhorst mass flow controller was used to control the shielding gas of a laser welding machine for both top shielding and back shielding of the welds.
The bottom gas adduction channel was integrated with the fixture system (**Fig. 6.5**).

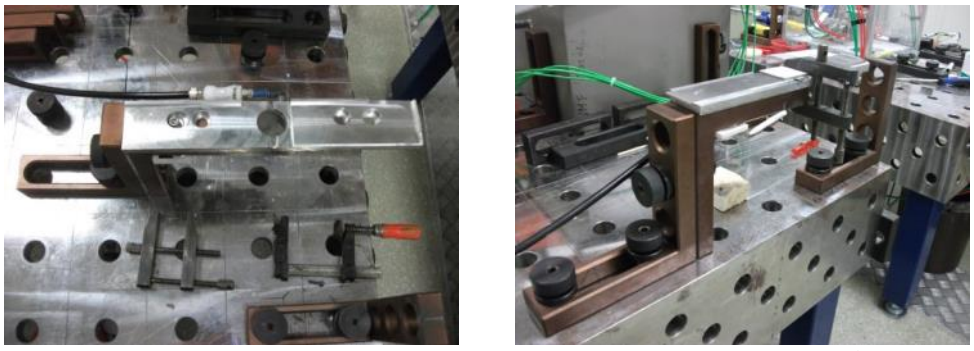

Figure 6.5: Fixture system for welding process with the black pipe for the bottom gas flow (left) and the mechanical clamps on the Mg alloy plates

The laser welding experiments investigated the overlap joint configuration. This configuration was obtained by securing the plate positions on a customised fixture with mechanical clamps (**Fig. 6.5**). The lateral surface of

the plates was machined to obtain unnotched specimens. The AZ31B sheets were cut and overlapped as shown in **Fig. 6.6**.

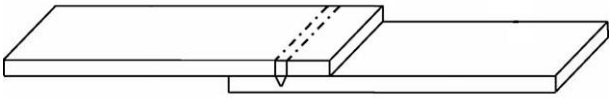

Figure 6.6: Configuration of the overlapping linear laser weld

6.2 Mechanical test equipment

6.2.1 Tensile test machine and laser extensometer

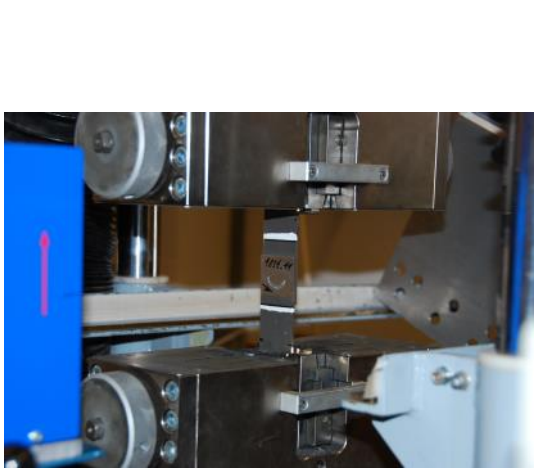

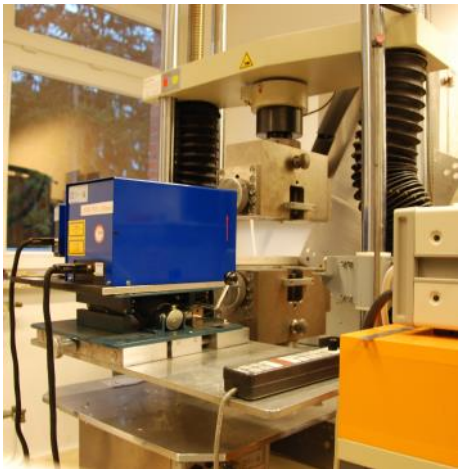

Figure 6.7: Tensile shear test and the tensile machine with the laser extensometer (blue box)

Monotonic tensile shear tests were conducted on a Zwick Roell RM100 machine (**Fig. 6.7**) equipped with a 100 kN load cell. A Fiedler Opto-Electronic (FOE) laser extensometer was used during the tensile shear tests. The extensometer allows non-contact deformation measurement from elastic range till plastic deformation with an accuracy of 0.01mm. The surface of the specimen is scanned by a laser beam. A set of white stripes (**Fig. 6.7**) applied to the surface reflects the laser light. The receiver evaluates the reflected light and changes the signals into measured displacement values.

6.2.2 Fatigue test equipment

Figure 6.8: A running fatigue test and the full fatigue testing equipment

The fatigue tests were conducted on a Schenck vertical servo hydraulic 10 kN test station (**Fig. 6.8**). The load-controlled tests were carried out at 30 Hz. Instability issues occurred following the imposed sinusoidal load with higher frequencies. For the fatigue test of overlap joints samples is preferred a S-type transverse vibration mode [15]. In this mode the spot weld in the middle is a vibration node. The test frequency was set to obtain the required oscillation mode.
Moreover, to ensure that the test sheets were not distorted or bent, suitable shim plates were inserted in the fixture system to prevent bending of the specimen when clamping it to the testing machine.
During the tests, the maximum and the minimum load was maintained constant with a load ratio of R=0.2. A positive value for the load ratio is preferred to ensure the stability of the system. The tests were terminated when the specimens failed or when they reached the chosen endurance limit of 10^7 cycles. Two machines with the same fixture system and testing parameters were used to reduce the required experimental time (**Fig. 6.8**).

6.3 Microstructure and chemical analysis equipment

Macro pictures and the bead measurements of the cross sections were obtained via optical microscopy. The microscope used was a VHX-Digital Microscope from Keyence with both distance and area measurement software integrated.
X-ray investigations were performed to discover any cracks or pores using the following parameters: 1.5 mm × 1.5 mm focal spot, a voltage of 50 kV, a current of 3.1 mA and a 2.9 min duration.

The microstructures were determined using a JSM-6490 SEM. The SEM is also equipped with an EDX detector and an EBSD system. These two systems allow for the chemical and structural characterization of materials at micrometer scales. The texture orientation and the grain size was inspected with the EBSD system.

7 Experimentation: design of experiments

The design of the full experimental work and the results analysis is here presented. In this section, the investigation is carried out on the linear, C-shape and circular spot welds in overlapped sheets of AZ31B Magnesium alloy using a Nd:YAG laser beam welding process. The research seeks to arrange an optimal laser-spot welding process of magnesium alloys to replace the lack of knowledge in the manufacture automotive joints. The research investigates, at first, the combination of process parameters and design of the joints that improves the structural and fatigue strength of the mechanical components. Mechanical behaviour of specimens is tested under fatigue and static loadings to compare the results with the conventional resistance spot weld joints.

7.1 Reference joint configuration obtained via resistance spot welding

Resistance spot welding is the conventional welding process with which the work with the laser welding process will be compared. Therefore, state-of-the-art resistance spot welded specimens were obtained. Several different conditions were created during the preliminary experiments by changing the main welding parameters in accordance to [16]. These conditions correspond to the process parameters listed in **Table 7.1** and were selected because of the low distortion, large nugget size and reduced number of visual defects produced.

Table 7.1: Process parameters for resistance spot welds characterisation

Welding current [kA]	Electrode force [kN]	Pre heating time [ms]	Welding time [ms]	Post heating time [ms]	Nugget diameter [mm]
24	5	1200	140	300	7.03 ± 0.46

The resulting overlap joints with the typical circular welded nugget were fabricated using an industrial resistance spot welding machine at STADCO as a comparative case study.

7.2 Laser beam welds

7.2.1 First screening experiments of laser welded joint configuration

The laser beam generated by the Nd:YAG source had a 1.06 μm wavelength and little tendency to create plasma [4]; therefore, Argon should be sufficient to produce sound beads. However, helium was used on the root side of the weld to ensure proper shielding. The upper surface was shielded with argon or helium blown coaxially from the laser head.

The DOE and ANOVA principles were used in the first screening experiments to define the feasibility of the process parameters.
The response variable was the depth-of-penetration ratio (DoP):

$$DoP = \frac{w}{t} \times 100 \qquad \text{(Eq. 7.1)}$$

Where the penetration, w, in Eq. 7.1 was measured using cross sections obtained from the linear joints as shown in **Fig. 7.1**.

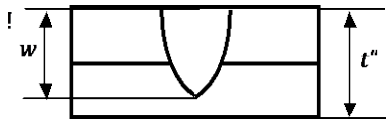

Figure 7.1: Depth of penetration measured from the cross section of the linear joints

The main laser welding parameters that influenced the DoP were first identified [7, 17-19]. To minimise the experimental effort required, a fractional factorial design with 2 levels and 4 factors: beam focus position (FP), welding speed (v), laser beam power (P) and shielding gas used for the top surface (Gas). A 2^{4-1} design was realised without replicates and a resolution=IV. The default design generator is Gas = v* P* FP
Table 7.3 lists the variable parameters of the factorial design with (-1) in the last column standing for 10 l/min Argon and (+1) standing for 20 l/min of Helium, respectively. The helium flow on the bottom was fixed to 4.5 l/min for all conditions. The welding direction coincides with the rolling direction of the Mg-alloy sheets.
The keyhole laser mode is reached thanks to the high irradiance values reported in **Tab. 7.3** as the ratio of the laser power to the spot area on the work piece.

$$A(z) = \pi \times \frac{{d_o}^2(z)}{4} \qquad \text{(Eq. 7.2)}$$

In **Eq. 7.2**, d_o is the waist diameter of the laser beam.
The Energy input per linear unit (E [J/mm]), representing the heat input of the laser welding process, is calculated as written below (**Eq. 7.3**)

$$E = \frac{P}{v} \qquad \textbf{(Eq. 7.3)}$$

Table 7.2: Laser optical parameters for laser welding process

λ	wavelength	1,064	µm
d_{fo}	fiber diameter on robot	400	µm
f_f	focalization length (f)	200	mm
f_r	collimation length	200	mm
d_o	waist diameter	400	µm
d_f	beam diameter out of the source	8	mm
$d_o(z)$	spot diameter on work-piece (z-function)	412,3	µm
$z\text{-}z_o$	focus position	-2,5	mm
A (z=-2.5mm)	spot area @ surface, FP= -2.5mm	0,134	mm^2
A (z= 0mm)	spot area @ surface, FP= 0mm	0,126	mm^2

The waist diameter was calculated with the following equation (Eq. 7.4)

$$\boldsymbol{d_o = d_{fo} \times \frac{f_f}{f_r}} \qquad \textbf{(Eq. 7.4)}$$

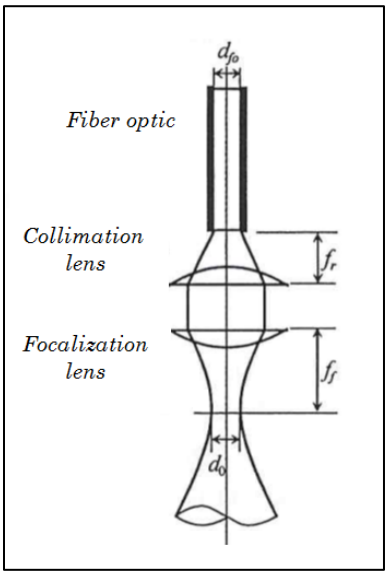

Figure 7.2: Focalization of a laser beam led from an optic fiber [29]

It is possible introduce the waist diameter (d_o) value in the "caustic equation" (**Eq. 7.5**) that is a rotational hyperboloid representing the convergent-divergent laser beam profile (**Fig. 7.2**)

$$d_o{}^2(z) = d_o{}^2 + (z - z_o)^2 \times \vartheta^2 \qquad \textbf{(Eq. 7.5)}$$

In the **Eq. 7.5**, ϑ is the divergence angle related to the beam quality and wavelength. This parameter can be approximated by the following equivalence:

$$\vartheta = \frac{d_f}{f_f} \qquad \textbf{(Eq. 7.6)}$$

The **Eq. 7.5** becomes:

$$d_o{}^2(z) = d_o{}^2 + (z - z_o)^2 \times \left(\frac{d_f}{f_f}\right)^2 \qquad \textbf{(Eq. 7.7)}$$

The $d_o(z)$ value achieved from the last equation (**Eq. 7.6**) was used to calculate the laser spot area at the surface to get approximately the irradiance values on the work piece (**Tab. 7.3**).

Table 7.3: LBW Fractional Factorial Design

Sample n.	Std Order	v [mm/s]	P [W]	FP [mm]	Gas	Irradiance [W/mm²]	Energy input [J/mm]
#1	6	60	2600	0	-1	20635	43
#2	1	40	2600	-2.5	-1	19403	65
#3	7	40	3000	0	-1	23810	75
#4	4	60	3000	-2.5	-1	22388	50
#5	5	40	2600	0	+1	20635	65
#6	3	40	3000	-2.5	+1	22388	75
#7	2	60	2600	-2.5	+1	19403	43
#8	8	60	3000	0	+1	23810	50

A statistical model using the significant factors allowed the combination of valid laser beam parameters required to obtain a fully penetrated bead. The ANOVA analysis was applied to the average of the two DoP values obtained for the cross section from the middle of the linear joint. Before welding, the sample surface was ground using P100 abrasive paper in the rolling direction to eliminate any contamination. The bead cross sections were manually ground, polished, and etched with a Picric acid solution according to the composition shown in **Table 7.4**.

The etching time in the Picric acid solution was around 10 seconds. Ethanol was used to clean the surface after the etching. The penetration depth was evaluated via optical microscopy.

Table 7.4: Etching solution

Picric acid standard solution			
Distilled water	Acetic acid	Ethanol	Picric acid
30-40 ml	6.5-7 ml	140 ml	2-3 ml

7.2.2 Optimised laser welded joint configuration

Based on the results of the statistical analysis (see the **Section 8.2.1**), two of the conditions from **Table 7.3** were selected to characterise the mechanical properties of the laser welded joints and determine the best process parameters for reproducing different laser welded joint shapes. **Table 7.5** shows the experimental process parameters used in the static characterisation. A slight decrease in the laser power from the previously tested values was preferred to eliminate the drop-out defect [8] and reduce inner porosity [9]. Helium was chosen as the shielding gas because it produced a more stable welding process and provided a smoother bead with fewer notches [2]. Three replications were executed for each condition of the Table 7.5.

Table 7.5: The two process parameters tested during the tensile shear tests

Sample n.	**V** [mm/s]	**P** [W]	**FP** [mm]	**Sh. Gas**
#3b	40	2800	0	+1
#6b	40	2800	-2.5	+1

Monotonic tensile shear tests were conducted at a rate of 0.5 mm/s according to the standard ISO 14273:2000 [10] on the Zwick Roell machine (**Section 6.2.1**). The AZ31B sheets were cut and overlapped as shown in **Fig.6.6** in accordance with the standard for shear testing resistance spot welds ISO 14273:2000 (**Tab. 7.6**). The lateral surface was machined to obtain un-notched specimens.

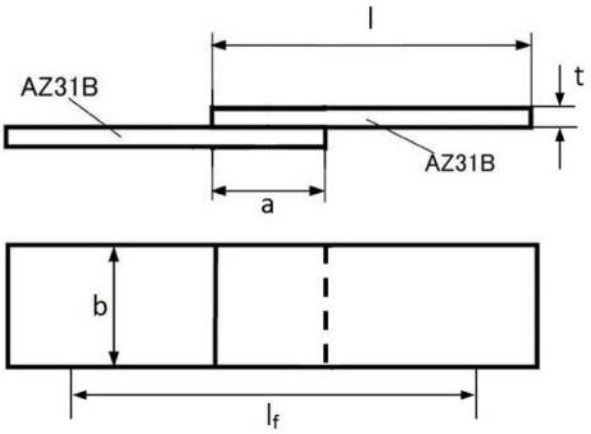

Figure 7.3: Specimen dimensions and configuration for shear tensile testing after laser welding

Table 7.6: Specimen size for shear tensile testing as defined by ISO 14273:2000 (l_f stands for free length between clamps)

	t [mm]	**a [mm]**	**b [mm]**	**l [mm]**	**l_f [mm]**
Tensile test	2.5	46	40*	138	105

***: nonstandard length, 10% reduction in strength**

The rolling direction may influence the results, therefore, the material was always cut in order to have the rolling direction perpendicular to the load direction during the tensile test (**Fig. 7.4**).

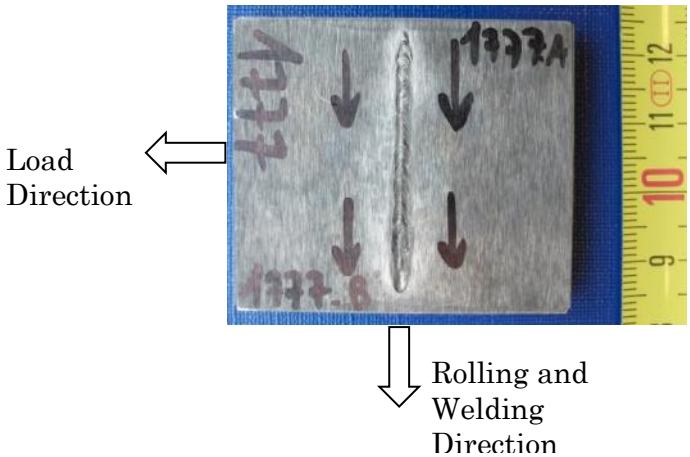

Figure 7.4: Specimen configuration for shear tensile and fatigue testing

An optimised laser beam joint was observed at the BSE and EBSD for the microstructure and texture analysis. First of all, the bead cross section was

analysed at the SEM. Several pictures were taken to investigate the effect of the solidification after the welding process, from the top to the root of the laser weld bead. The energy dispersive X-ray microanalysis (EDX) was performed to show the chemical composition of the laser fusion zone.
With the EBSD analysis it was expected to characterize the overlap weld in terms of microstructural features and local orientations. Moreover, the aim of the investigation was to find if there is any effect on mechanical behaviour. The cross section investigated was the #6b experimental condition with a linear laser lap welding of AZ31. The EBSD and the microstructural studies performed were matched to illustrate and discuss the structure and constitution of the laser weld.

7.2.3 Design of the different laser welded joint shapes

After the preliminary static characterisation, the best of the two conditions in terms of the maximum tensile shear load with lowest standard deviation (see **Table 8.3**) was selected for executing the different laser welded joint paths. **Table 8.7** shows the optimised process parameter conditions.

Table 7.7: LBW process parameters used for fabrication of tensile and fatigue specimens of different joint shapes

v [mm/s]	**P [W]**	**FP [mm]**	**Shielding Gas**
40	2800	0	20 l/min He above 6 l/min He below

Different laser welded paths were used to understand how different shapes could affect the maximum load and fatigue behaviour [11]. Three different joint shapes, arc, circle and line (see **Fig. 7.5b**), were investigated for comparison to the nugget shape from the resistance spot weld. The principle of equivalently resistant areas was used to dimension the three different shapes (**Table 7.8**). Partially overlapping the circular trajectory and power ramp during the starting and ending welding phases is a common strategy for avoiding discontinuities that can affect the specimen fatigue resistance [12-14].
The investigated laser welding shapes (**Table 7.8**) were designed to obtain a nominal resistant area closer to a Resistance Spot weld nugget area (d_{nugget}=7mm).
To ensure the closure of the weld ring, a 90 degrees overlapped welding line was established. A power ramp to switch off the laser beam smoothly was performed along this overlapped weld sector by decreasing the laser power and increasing 50% of the welding speed [..].

The critical points are in the front of the weld ring for fatigue test [12,14] and at the points on the diametrical line, perpendicular to the load direction for the stresses intensification in static load. Therefore, the start and end locations of the LSW rings were not positioned to the highly stressed regions. The linear welds were designed with two power ramps on the start and the end point to reduce the beam instability.
For all the welding paths, the real resistant area was evaluated via digital microscopical measurements of the surfaces after the tensile failure.

Table 7.8: Welding geometries for mechanical characterisation (the bead width was assumed to be 1.5 mm)

LASER WELDING			*RESISTANCE SPOT WELDING*
Arc path	*Circular path*	*Linear path*	
Radius = 11.4 mm 120°	7.6 mm	23.9 mm	7 mm

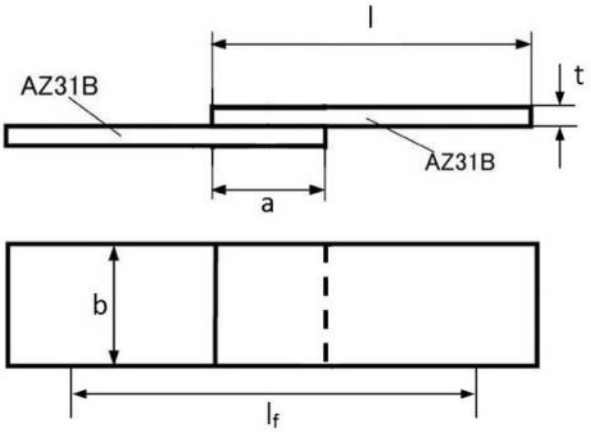

(a)

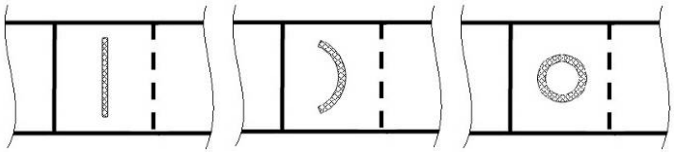

(b)

Figure 7.5: Specimen dimensions and configurations for tensile shear and fatigue testing after laser welding (a), and the laser welded joint shapes (b)

The AZ31B sheets were cut and overlapped as shown in **Fig. 7.5** according to the resistance spot welding standards for shear tensile and fatigue testing, ISO 14273 and EN ISO 14324, respectively [10, 15]. The lateral surface was machined to obtain unnotched specimens. The free length between the clamps differentiates the two configurations (see respective measures in **Table 7.9**). Nine replications of each welding path were tested with a load ratio of R=0.2 at 30 Hz for each joint shape. L-N curves were plotted to compare the fatigue behaviour of the different laser welding paths. Macro pictures of the cross section were obtained via optical microscopy as well as the fracture surface images of the tested specimens.

Table 7.9: Specimen size for fatigue tests as defined in EN ISO 14324:2003 (l_f stands for free length between clamps)

	t [mm]	**a [mm]**	**b [mm]**	**l [mm]**	**l_f [mm]**
Fatigue test	2.5	45	40*	138	200

***: non standard length, 10% reduction in strength**

7.3 Comparison of the Laser Beam and Resistance Spot welds

The microstructures of the welded metal (WM) and base metal (BM) were investigated. The microstructures were determined using the scanning electron microscope (SEM) with different magnifications.
Micro-hardness tests (HV0.1) were performed on the weld cross section according to the ASTM E384-99 standard. Micro hardness measurements were realised for the following five linear profiles: along the interface between the two AZ31B rolled sheets and at varying distances from the interface (± 1.25 mm and ± 0.5 mm from the interface plane).
The tensile shear tests were carried out to compare the LBWs and RSWs in terms of load to failure[10]. The fatigue tests were conducted according to the standard EN ISO 14324:2003 [15] using the Schenck vertical test station (**Section 6.2.2**).
12 replications were used for the resistance spot welding and 9 were used for the linear laser path to study the strength of the joints in the tensile-shear configuration under different cyclic loadings. L-N curves were plotted, according to the standards [15], to compare these results to those for the state-of-art resistance spot welds.
X-ray investigations were performed to discover any cracks or pores. The EDX microanalysis showed the chemical composition of both laser and

resistance spot joints after the welding process. The variation of the chemical composition was investigated along a linear profile, starting from the base material and until it crossed the weld metal.

8 Experimentation: results analysis

8.1 Material characterisation

8.1.1 Base material properties

AZ31B magnesium alloy conforming to ASTM275 was obtained as 2.5 mm thick plates.
The rolling direction influence the results, therefore, the AZ31 samples were cut in order to have the rolling direction normal to the load direction during the mechanical tests. The nominal chemical composition and measured mechanical properties of the base material are presented in **Table 8.1**.
"MgF Flachprodukte GmbH" from ThyssenKrupp provided the AZ31B sheets used for the laser and resistance spot specimens.

Table 8.1: Chemical composition and mechanical properties of AZ31B

(a) Chemical composition of the base magnesium alloy AZ31B (measured - wt. %)

Al	Cu	Mn	Fe	Ni	Zn	Si	Mg
2.69	0.00092	0.318	0.00138	0.00031	0.69	0.0308	96.26

(b) Mechanical properties of the base magnesium alloy AZ31B

Ultimate tensile strength	Yield strength (Rp02)	E-Modulus	Hardness
MPa	MPa	MPa	HV 0.1
261 ± 1	161 ± 3	42100	57.4 ± 2.4

After a hot rolling and annealing treatment, the material had an equiaxed grain microstructure (average grain size of 16.1 µm) with both α-Mg (hexagonal crystal structure) and β-$Mg_{17}Al_{12}$ (cubic crystal structure) phases and included fine Mn particles (see **Fig. 8.1**). These included particles appear bright in **Fig. 8.2** because of their higher Mn and Al content and lower Mg content relative to the matrix.

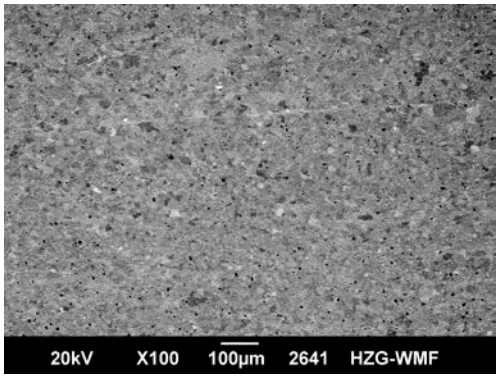

Figure 8.1: Microstructure of the base material AZ31B

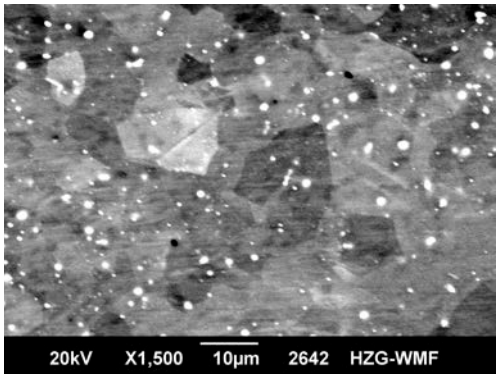

Figure 8.2: Base material at higher magnification used as reference for EDX point analysis

8.1.2 EDX analysis and microtexture of base material

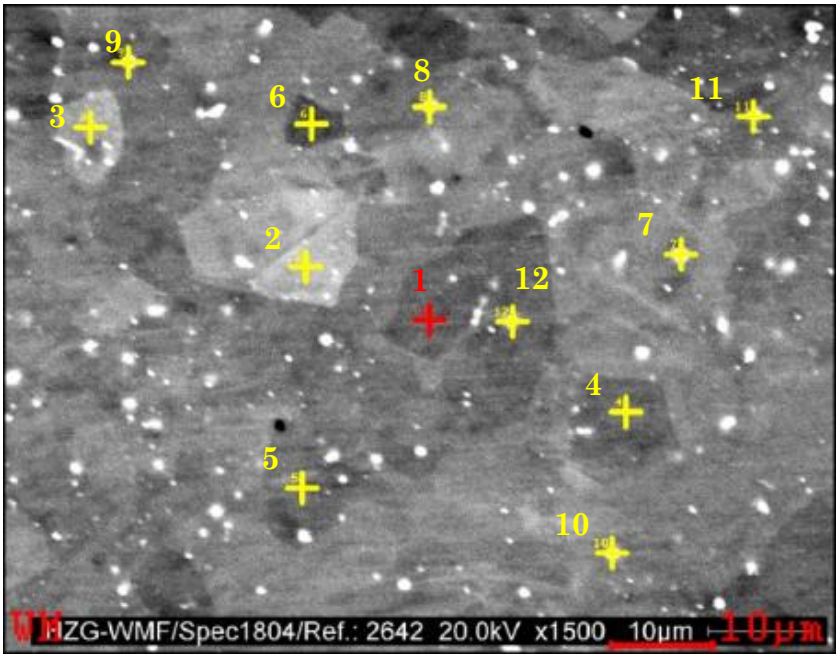

Figure 8.3: Measure points #1 - #6 record chemical composition of grains. Measure points #7 - #12 record chemical composition of included particles

Table 8.2: Punctual chemical composition at the listed position referred to Fig. 8.3

Position	Mg	Al	Zn	Mn
Matrix				
1	97.06	1.98	0.68	0.28
2	96.95	2.03	0.76	0.27
3	97.02	2.01	0.70	0.26
4	97.09	1.98	0.68	0.25
5	97.16	1.91	0.67	0.25
6	97.02	2.03	0.69	0.27
Particles				
7	92.30	4.03	0.67	3.01
8	93.77	3.44	0.64	2.15
9	84.02	9.80	1.05	5.07
10	91.84	4.92	0.66	2.58
11	92.95	3.90	0.68	2.47
12	93.30	4.06	0.66	1.97

The BSE images show superposition of crystal orientation contrast and Z-number contrast. The base material is characterised by inhomogeneity regarding structure and chemical composition. The Mn addition has the function to ensure resistance against corrosion.

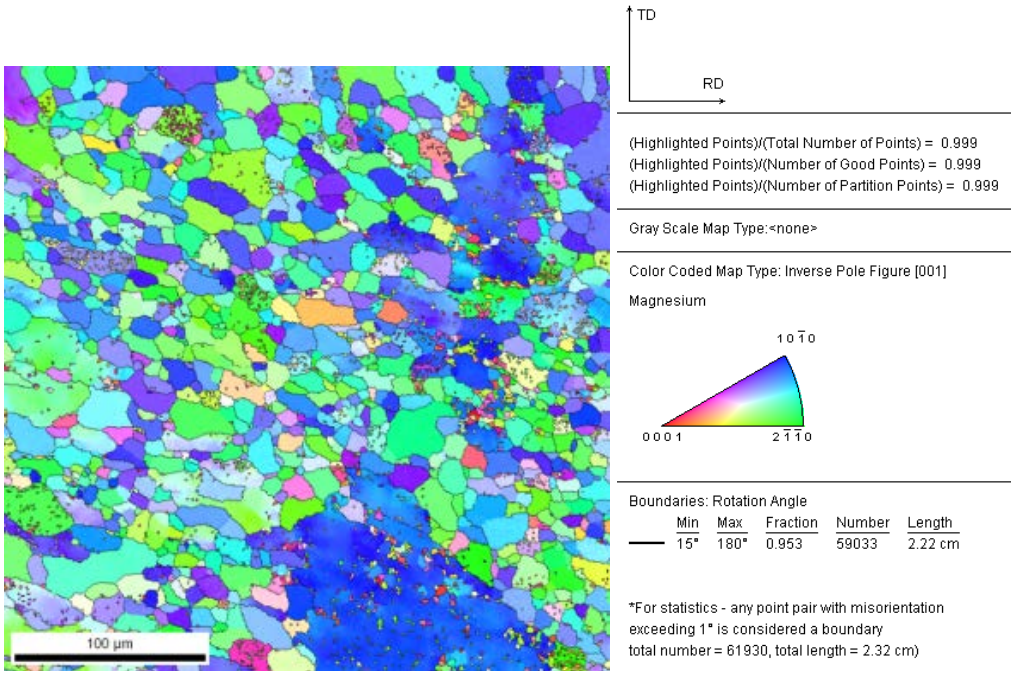

Figure 8.4: EBSD image of the base material

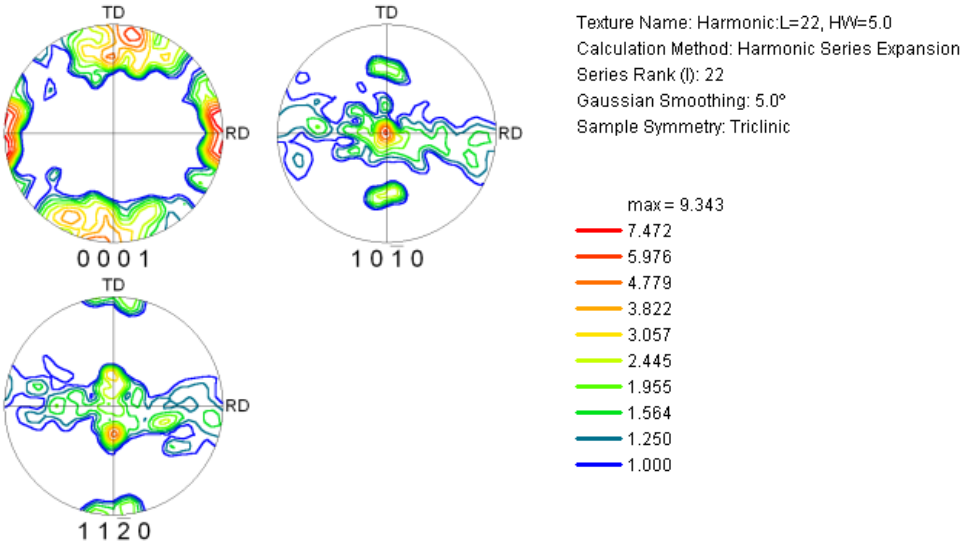

Figure 8.5: Pole figures showing the grain orientation

The grain size average within the selected region of interest was 16.1 µm not considering coarse grain below in the picture. The grain size average reached 21.2 µm considering the coarse grains in the right side of the picture.
The texture components showed <0001>//TD fibre texture, (1 0 -1 0)[0001] that means how the hexagonal crystals have the basal planes parallel to the rolling plane. Therefore, as is represented in the pole figures 1010 and 1120 (**Fig. 8.5**), prismatic crystal planes were prominent looking at the cross section trough the plates thickness (**Fig. 8.25**).

8.2 Laser beam welds

8.2.1 Laser welding process parameter investigation

As mentioned in **Section 7.2.1**, the fractional factorial design results were analysed in terms of the depth of penetration. **Fig. 7.1** shows the overall optical cross sections for the laser welded AZ31B joints under different conditions. The influence of heat on the bead geometry is clearly visible and affects both the weld penetration and bead width. At low velocities, the welding penetration increased with higher heat input [5]. Those

experiments using a welding speed of 40 mm/s were the only that reached complete penetration along the welding length.
From a visual inspection, the beads shielded by helium seemed to have a better surface quality. Helium determined a more stable welding process, obtaining a less roughened bead with less number of notches [2].
No craters were visible at the top, which indicates no material was removed via vaporisation of its chemical elements. However, the introduced heat tended to drop out when combined with the low viscosity and surface tension of magnesium [2].

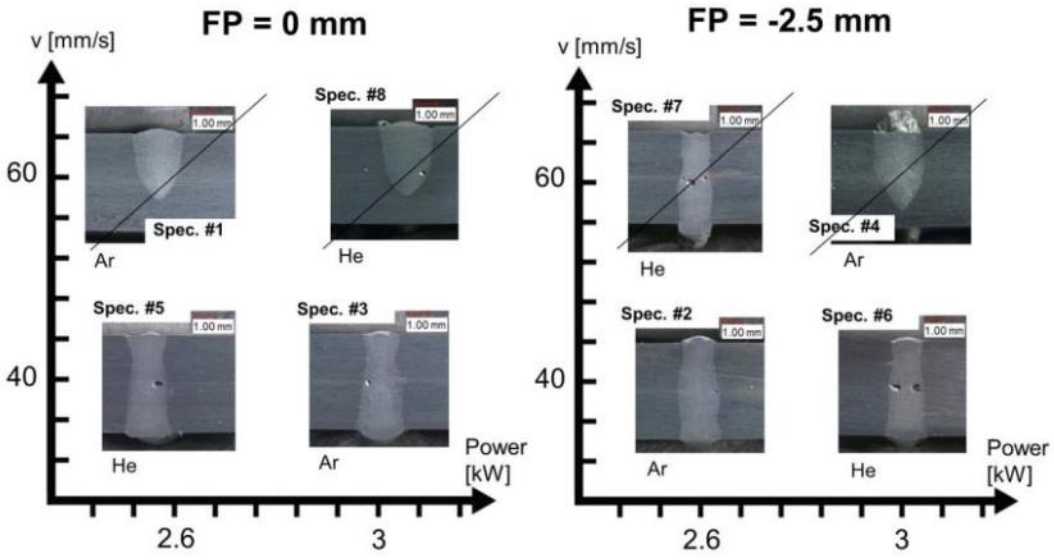

Figure 8.6: Pictures of the cross section for the different conditions in the factorial design (conditions statistically rejected are marked with a bar)

As the main effect plots in **Fig. 8.7** show, the welding speed (v) and focus position (FP) were the most significant factors while the laser power (P) and shielding gas (Gas) do not influence the penetration. Therefore, the latter two are assumed to be constant in the following experiments.

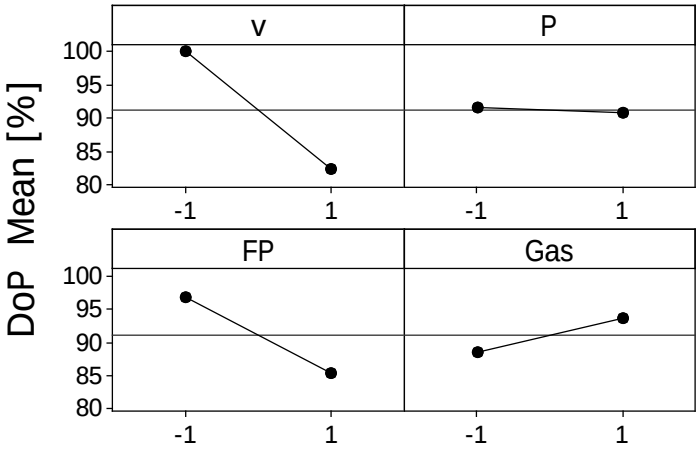

(a)

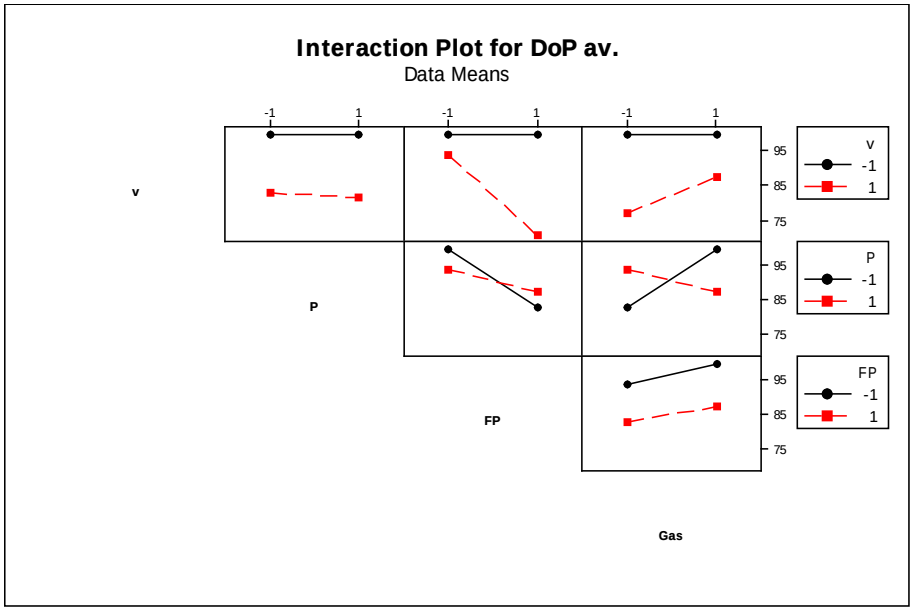

(b)

Graph 8.1: Main effect plot (a) and Interaction plot (b) for DoP data means

The ANOVA table is reported (**Table 8.3**) which indicates that the terms v, FP, v*FP are statistically significant (p-value<5%).

Analysis of Variance for DoP av. (coded units)

Source	DF	Seq SS	Adj SS	Adj MS	F	P
Main Effects	2	898,6	898,6	449,28	15,63	0,013
v	1	626,2	626,2	626,20	21,79	0,010
FP	1	272,4	272,4	272,37	9,48	0,037
2-Way Interactions	1	272,4	272,4	272,37	9,48	0,037
v*FP	1	272,4	272,4	272,37	9,48	0,037
Residual Error	4	115,0	115,0	28,74		
Pure Error	4	115,0	115,0	28,74		
Total	7	1285,9				

S = 5,36127 PRESS = 459,891
R-Sq = 91,06% R-Sq(pred) = 64,24% R-Sq(adj) = 84,35%

Term	Effect	Coef	SE Coef	T	P
Constant		91,153	1,895	48,09	0,000
v	-17,695	-8,847	1,895	-4,67	0,010
FP	-11,670	-5,835	1,895	-3,08	0,037
v*FP	-11,670	-5,835	1,895	-3,08	0,037

Table 8.2a: ANOVA table and Estimated Effects and Coefficients for DoP average

The Standardized Residual did not reject the normality and the homoscedasticity hypothesis. Moreover there are not standardized residual outliers with values not higher than 3 in modulus (**Fig. 8.8**).

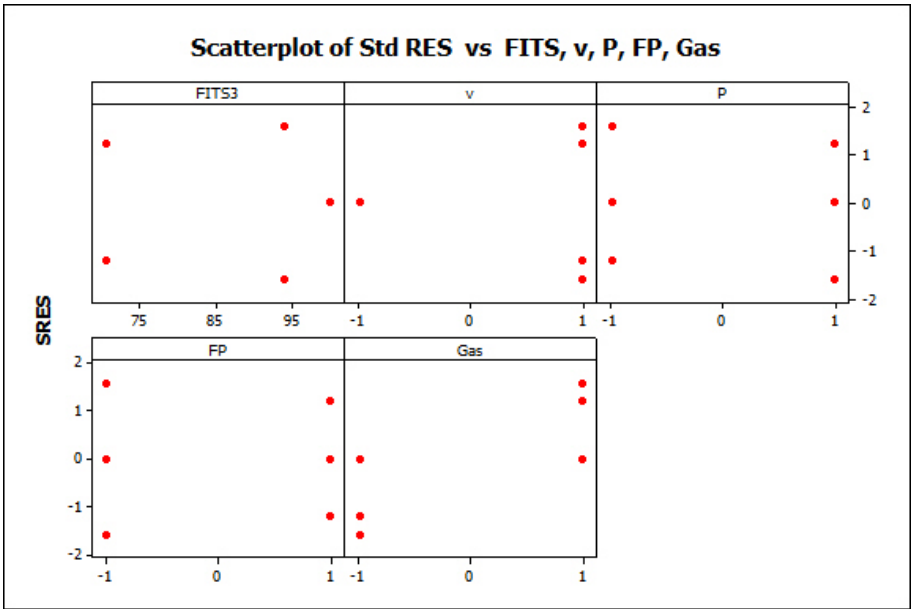

Graph 8.2: Scatterplot of the Standardized Residuals versus Fits values and the investigated parameters

Therefore, these three terms, v, FP and FP*v, were included in the following regression model (**Eq. 8.1**), which fits well with the experimental data (R-Sq_adj = 84.35%):

$$DoP\ av. = 91.1527 - (8.84732) * v - (5.8349) * FP - (5.8349) v * FP \quad \textbf{(Eq. 8.1)}$$

Using the regression Eq. 2, the low levels for both Welding speed and Focus position maximise the response variable. Furthermore, an enhancement of the depth of penetration is expected with the welding speed at the low level (- 1) and the Focus position at the high level (+ 1).
Finally, (v = - 1; FP = - 1) and (v = - 1; FP = + 1) are the conditions that maximise the response variable DoP.
Since the laser power is not statistically significant in this range, the conditions #3 and #6 (represented in **Table 7.5**) were chosen to ensure a through weld due to the higher energy input.

8.2.2 Optimised laser welded joint configuration

Linear welds on 52 mm wide samples were accomplished, they were cut after the process in 23.9 mm wide overlap joints to compare the tensile tests results to the RSW data with similar welding areas. In this way, shear tensile tests without edge notches, no start up effect of the laser beam on the weld bead were performed.

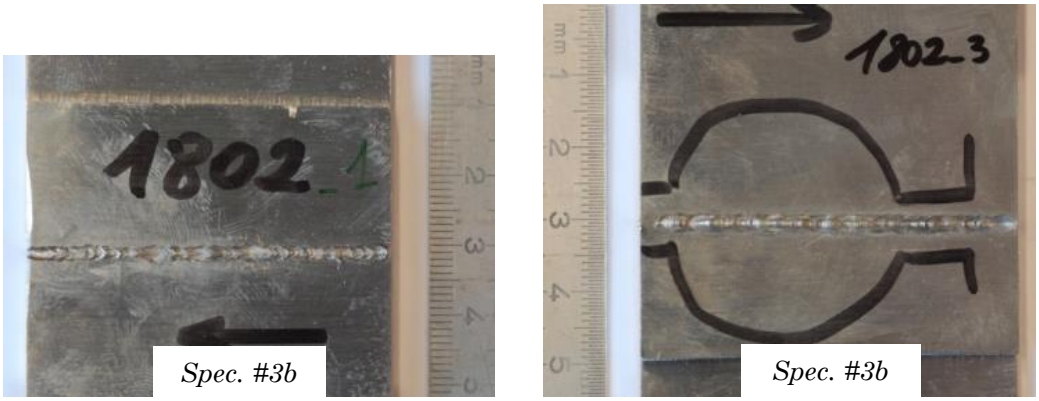

Figure 8.9: Macro-view (top and bottom in left and right pictures respectively) of laser welded surfaces using the #3b experimental condition

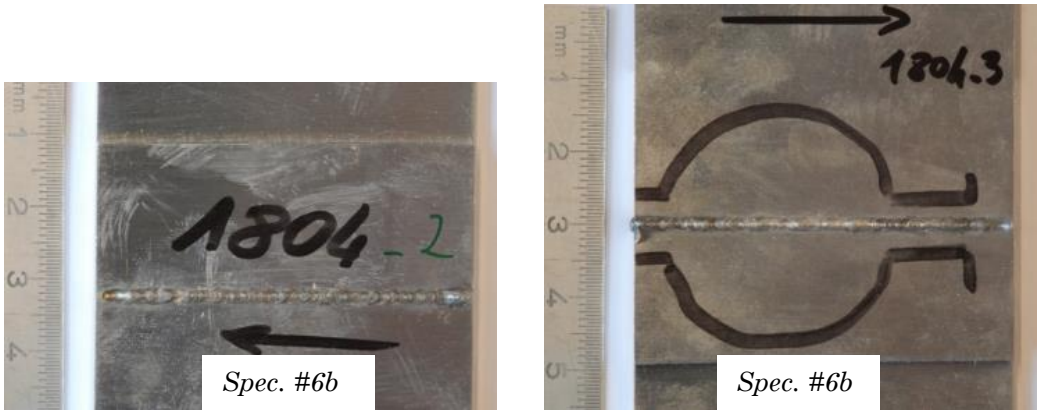

Figure 8.10: Macro-view (top and bottom in left and right pictures respectively) of laser welded surfaces using the #6b experimental condition

Fig. 8.9 and **8.10** show the bead surfaces. For the linear laser joints, smooth weld surfaces were achieved.
At a first optical appearance the condition with focus position at -2.5 mm (condition #6b) seemed to have more stability in the bead width. The good optical appearance obtained on the surfaces is an important aspect in the automotive application.

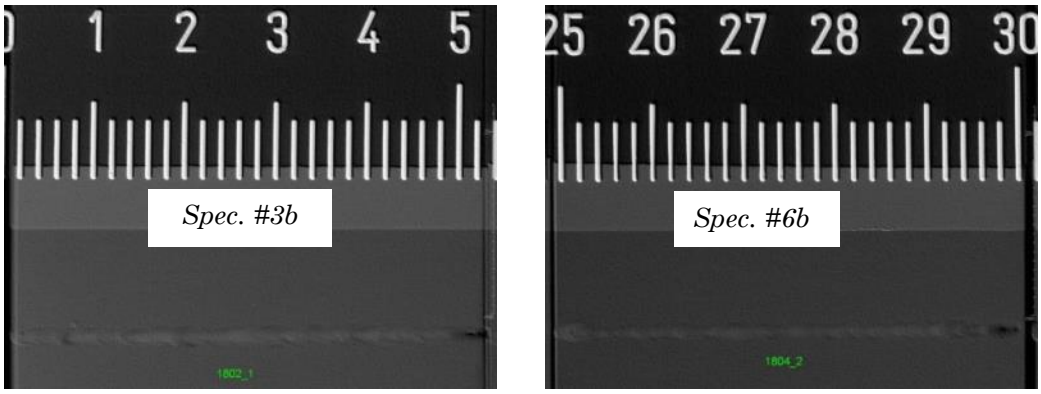

Figure 8.11: X-ray images of laser overlap joints welded of the two selected experimental conditions

Fig. 8.11 represents the X-radiography results. They reveal the absence of porosity, cavities or cracks in the weld metal. The darker holes on the right side of the pictures were due to the keyhole collapse at the bead end point.
Fig. 8.12 shows the cross section of the two selected conditions. Thanks to the surface grinding and slight decrease in power (relative to the previous tests) both bead cross sections have a good bead shape with neither cracks nor pores and do not present a drop out defect. Surfaces grinding was one of the key factors for reducing the porosity and increasing the failure strength.

Three unnotched specimens were tested under static load for each condition, #3b and #6b (**Tab. 7.5**).

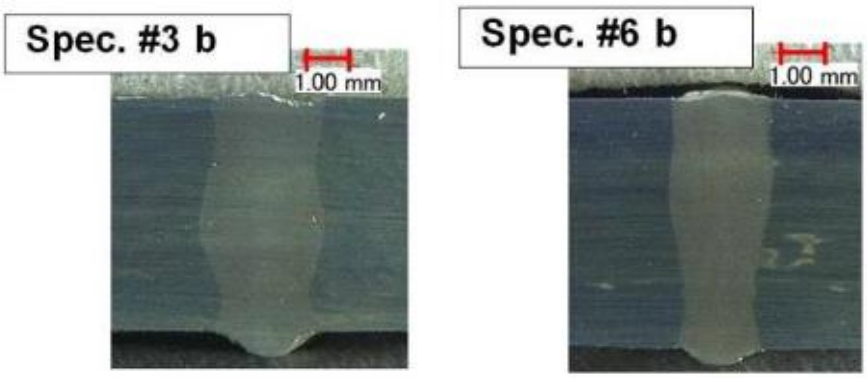

Figure 8.12: Cross section macro-view of laser overlap joints welded of the two selected experimental conditions

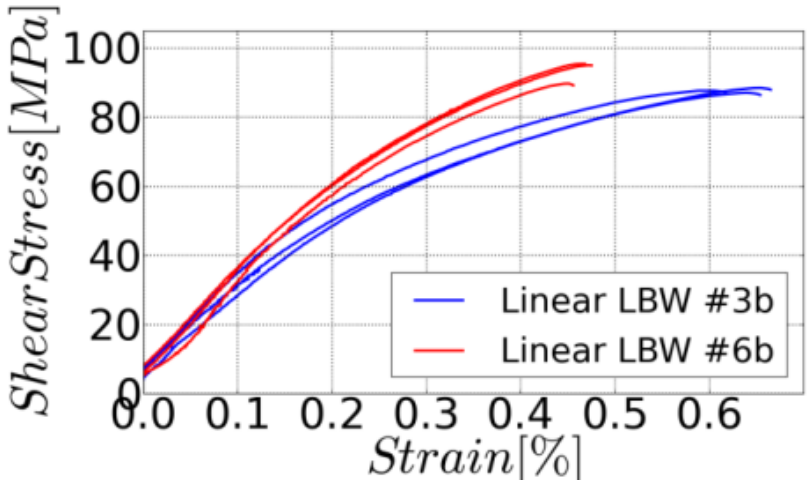

(a)

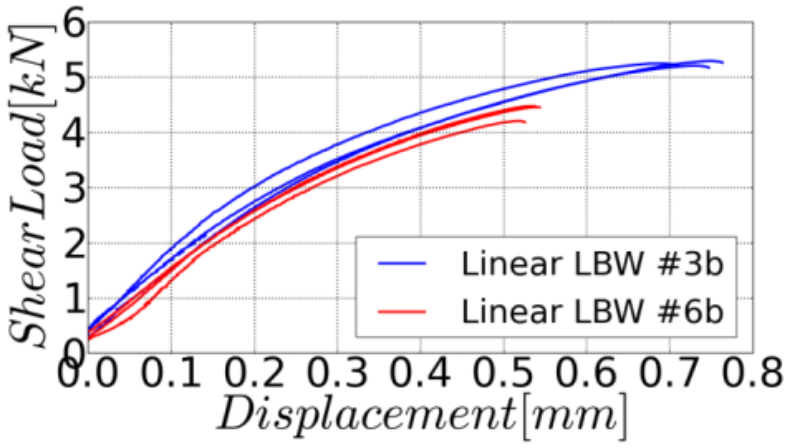

(b)

Graph 8.3: Tensile testing results for linear laser welds in overlap configuration: Stress-Strain (a) and Load-Displacement (b) graphs

Table 8.3: Ultimate tensile-shear load (UTSL) for the different linear laser weld conditions

	#3b	**#6b**
Ultimate tensile-shear load (UTSL) [kN]	5.25 ± 0.04	4.38 ± 0.14

The #3b experimental conditions possessed the highest load to failure and lowest standard deviation. The better result in term of Ultimate tensile-shear load is validated by the wider resistant section (**Fig. 8.12**).
The interfacial failure was the only mode of rupture. The weld at the interface in these specimens failed because the ultimate tensile shear strength in the fusion zone (FZ) was less than the BM. In fact, the graph in **Graph 8.8a** shows a clear failure of the mechanical properties within the fusion zone with peaks up to 40 *HV* 0.1. The hardness value of the material decreased because of grain coarsening from recrystallisation after the welding process (**Section 8.3.2**).

8.2.2.1 Microstructure and texture for linear laser beam weld BSE, EBSD analysis
Sample #6b was observed at the BSE and EBSD for the micro texture analysis.

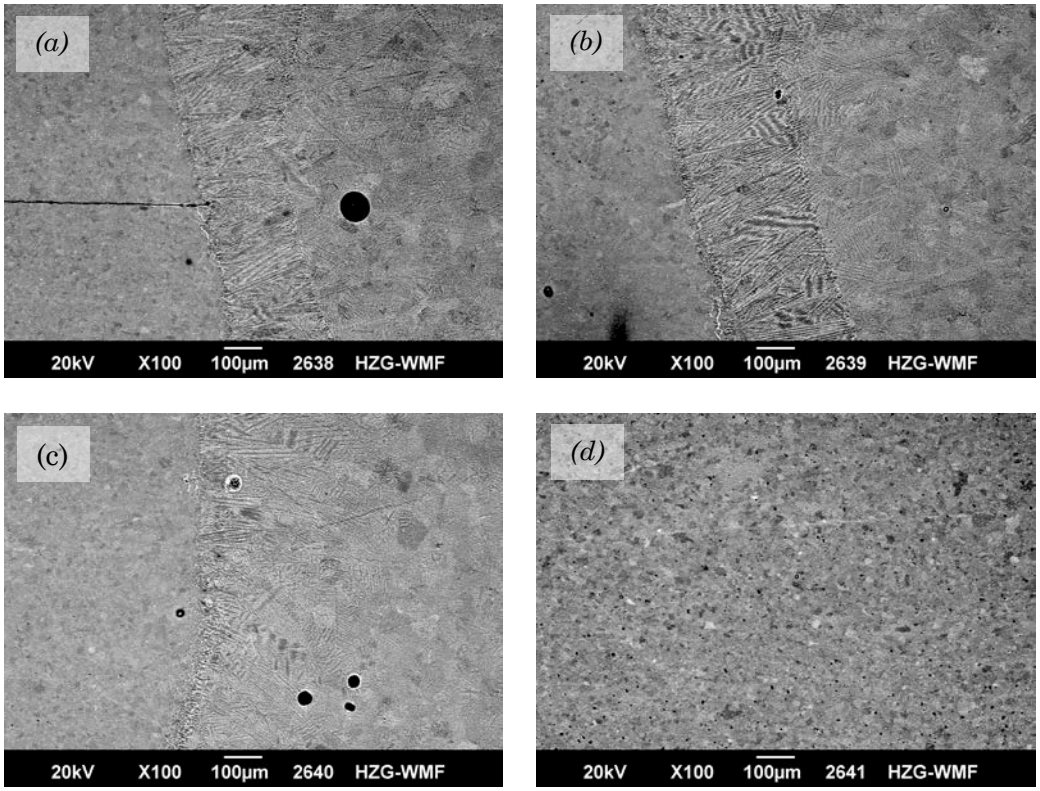

Figure 8.14: Cross section microstructures of the laser bead (experimental condition #6b) at the overlap zone on the left side (a), transitional area on the top side (b), transitional area on the bottom side (c), base material (d)

As it is possible to see in **Fig. 8.14a** and **8.14b**, there is dendritic solidification along the melt line at the interface between outer weld region and inner weld region. Equiaxial dendritic colonies are present within inner weld region (**Fig. 8.14b**) compared to the equiaxial grains within base material (**Fig. 8.14d**).
Some micro pores are located mainly near the melting line.

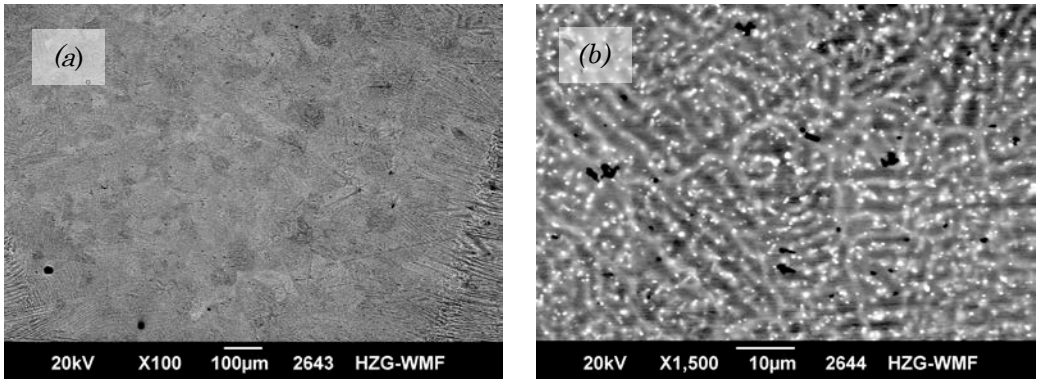

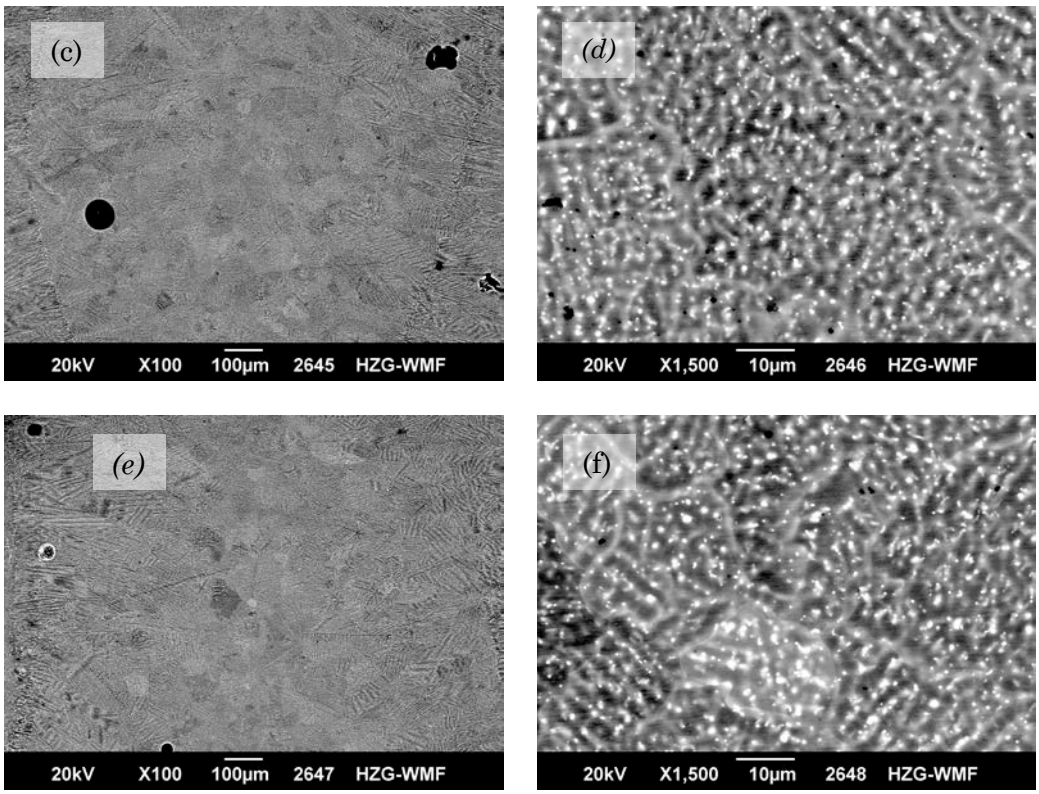

Figure 8.15: Cross section microstructures of the laser weld bead (experimental condition #6b): fusion zone on the top side(a), details of the fusion zone on the top side(b), centre of the fusion zone(c), details of the centre of fusion zone(d), fusion zone on the bottom side(e), details of the fusion zone on the bottom side (f)

As it is possible to see in **Fig. 8.15a**, the inner weld region has been uniformly developed with equiaxial colonies of dendrites. In the detail pictures (**Fig. 8.15b, d, f**) are shown the segregations due to the diffusion during the solidification after the laser process.
The fusion zone is chemically homogeneous (**Tab. 8.4**) from the top to the bottom side of the weld bead.

Region n.	Mg	Al	Zn	Mn
#2644	96.84	2.17	0.68	0.31
#2646	96.93	2.10	0.64	0.32
#2648	96.86	2.08	0.73	0.33

Table 8.4: Chemical composition of the selected area in the picture identified by the "Region n."

The first EBSD image (**Fig. 8.16**) was from the point x_0 , y_0 at the left weld/base material interface (on the cross section). The coordinates: x_0=6.742 mm, y_0= -36.855 mm are assumed as reference position.

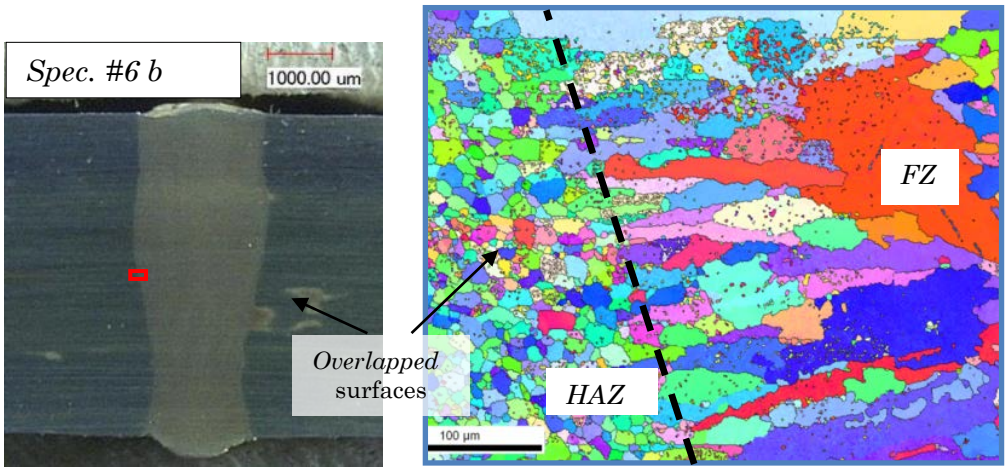

Figure 8.16: Cross section macro-view of laser overlap joints under #6b experimental condition and EBSD image at the red rectangle

In **Fig. 8.16** the bead cross section is observed. The area of the base material and the Heat Affected Zone (HAZ) show more green and blue colours which means the prismatic crystal planes of the hexagonal close-packed (hcp) are dominating the view where the equiaxial grains are placed.

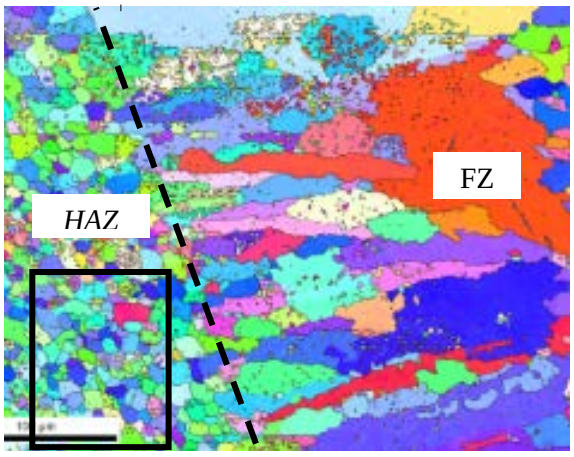

Figure 8.17: Reference cross-section picture for the EBSD analysis shown in Fig 8.18

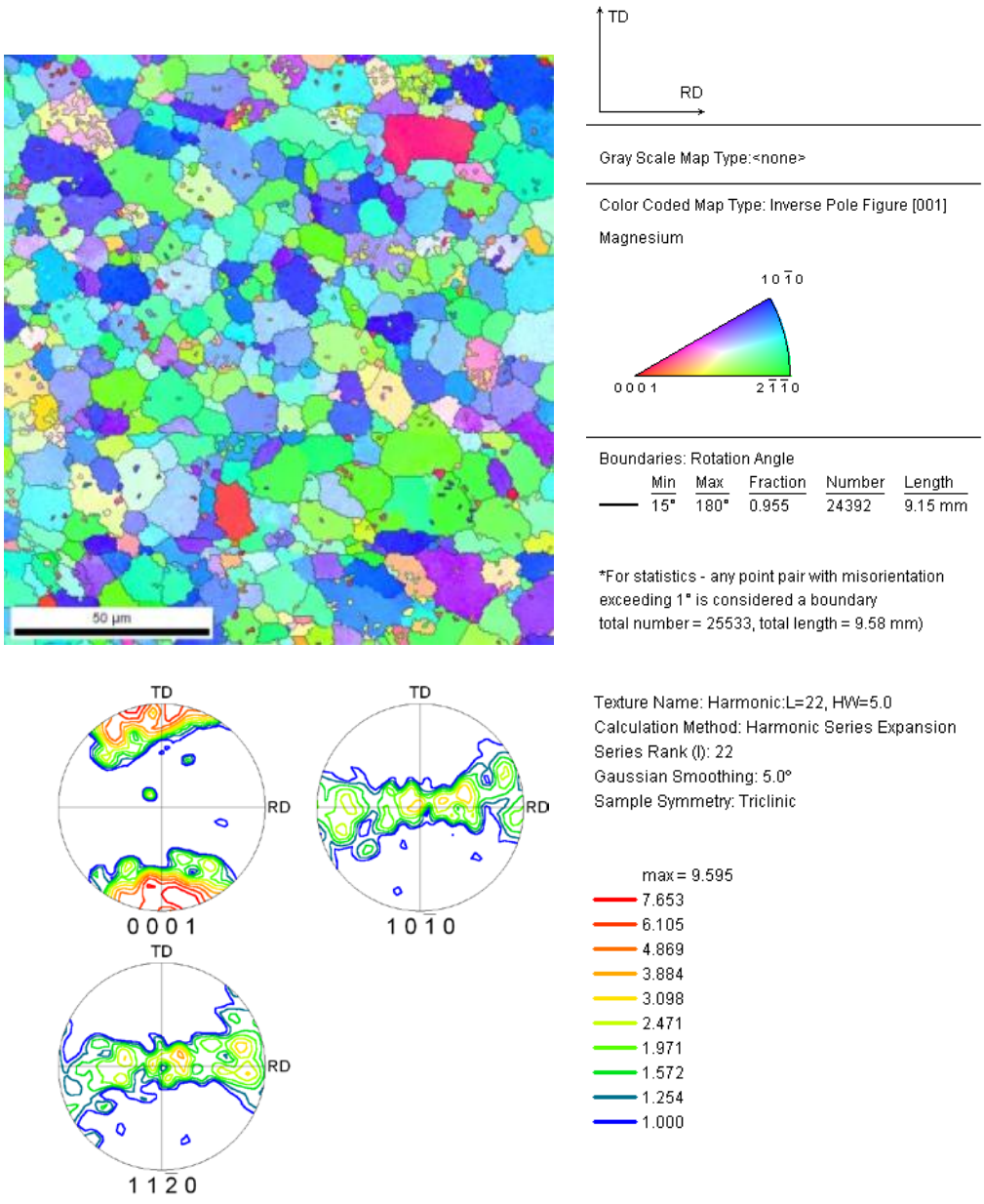

Figure 8.18: Detail of the EBSD image at the black rectangle section of HAZ at the melting line on the bead left side and corresponding pole diagrams

In **Fig. 8.18** below is shown the pole figure where transversal direction (TD) is the direction of thickness, while rolling direction (RD) is the rolling direction of AZ31B sheet (**Fig 8.19**). On the basal plane (0 0 0 1) is evident the effect on the rolling direction (anisotropic behaviour) as well as on the

prismatic plane (1 0 -1 0). At the selected region of HAZ the grains were 9.6 μm diameter wide (average).
Regard to the texture components within the selected region of interest, <0001> direction is parallel to the transversal direction (TD). In the scheme below (**Fig. 8.19**) is clearly represented the hcp crystals orientation in the HAZ.

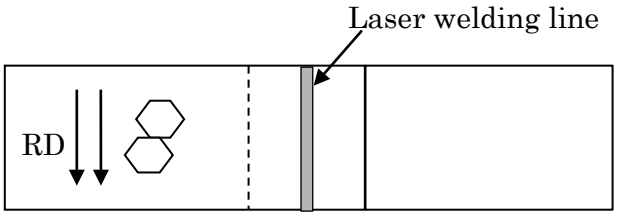

Figure 8.19: Hcp crystals orientation represented on the overlap joint configuration

At the interface FZ-HAZ the grains were 38 μm diameter wide (average). The following EBSD picture (**Fig 8.20**) represents a cross section of the laser beam weld.

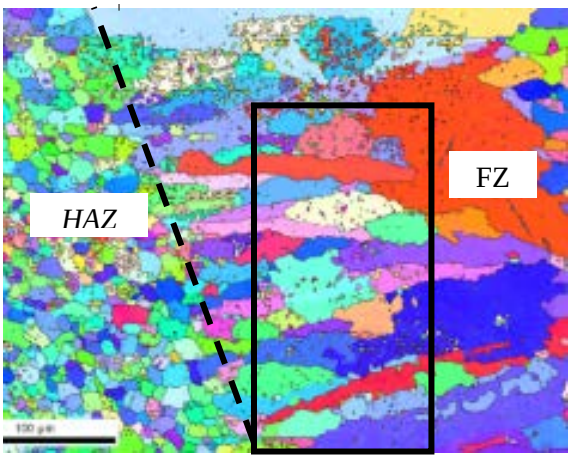

Figure 8.20: Reference cross-section picture for the EBSD analysis shown in Fig 8.21

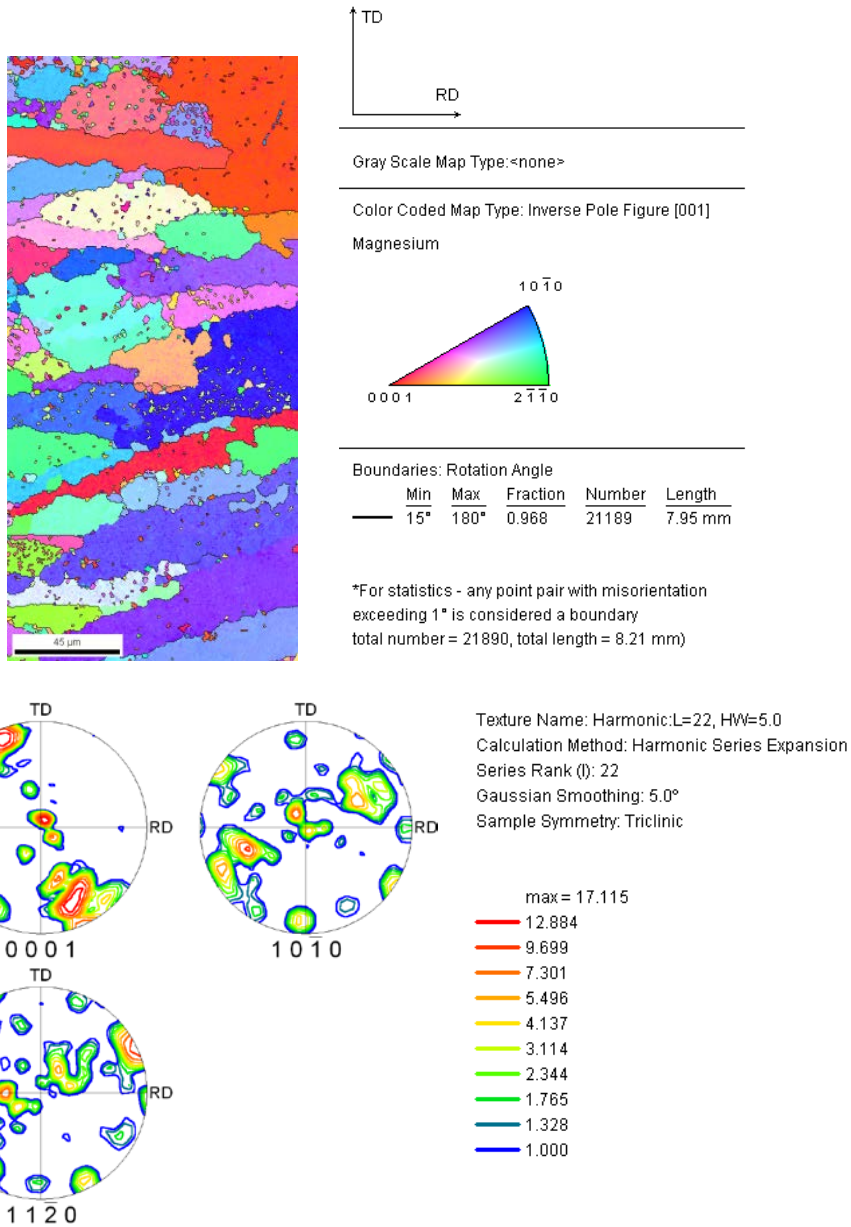

Figure 8.21: Detail of the EBSD image at the black rectangle section at the FZ on bead left side and corresponding pole diagrams

In **Fig. 8.21** on the top it is possible to observe dendritic, very coarse grains; prismatic crystal planes are pronounced. The grain size is 37.7 µm within the selected zone of interest.
In comparison to the HAZ it is possible to observe a tilt on (1 0 -1 0) pole diagram after the welding process.

The texture components are: g1 = (0 0 0 1)[1 1 -2 0]@θ = 105°, basal-transversal texture.
This way to described the texture components (g1) means that the (0001) plane is perpendicular to [1 1 -2 0] direction and tilted of 105°. As it is possible to see from the first pole diagram above (**Fig. 8.21,** (0001) pole diagram), the basal plane is tilted of 90° respect to the TD, thus <0 0 0 1> is parallel to the TD (**Fig. 8.19**). Moreover there are 15° (105°-90°) on the other angle (β=15°).

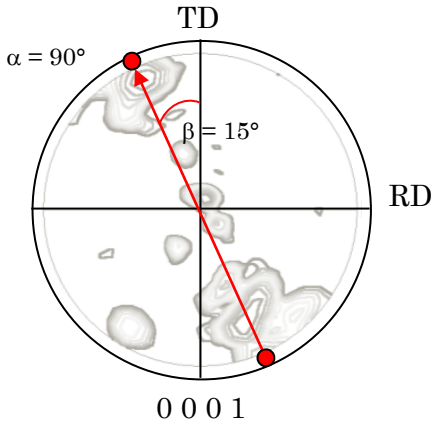

Figure 8.22: Schematic view of the pole diagram to identify the texture components

At the centre of the FZ the grains are 53μm diameter wide (average) at the point x=5.813 mm, y = -36.833 mm (**Fig. 8.23-8.24**).

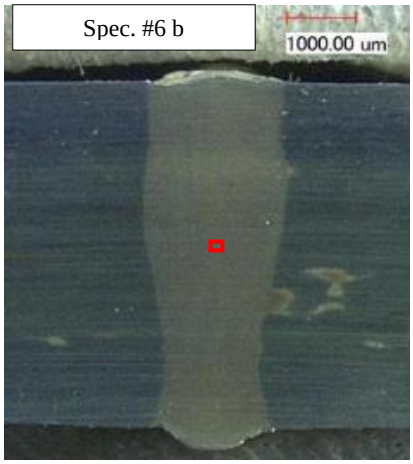

Figure 8.23: Reference picture for the EBSD analysis shown in Fig 8.24

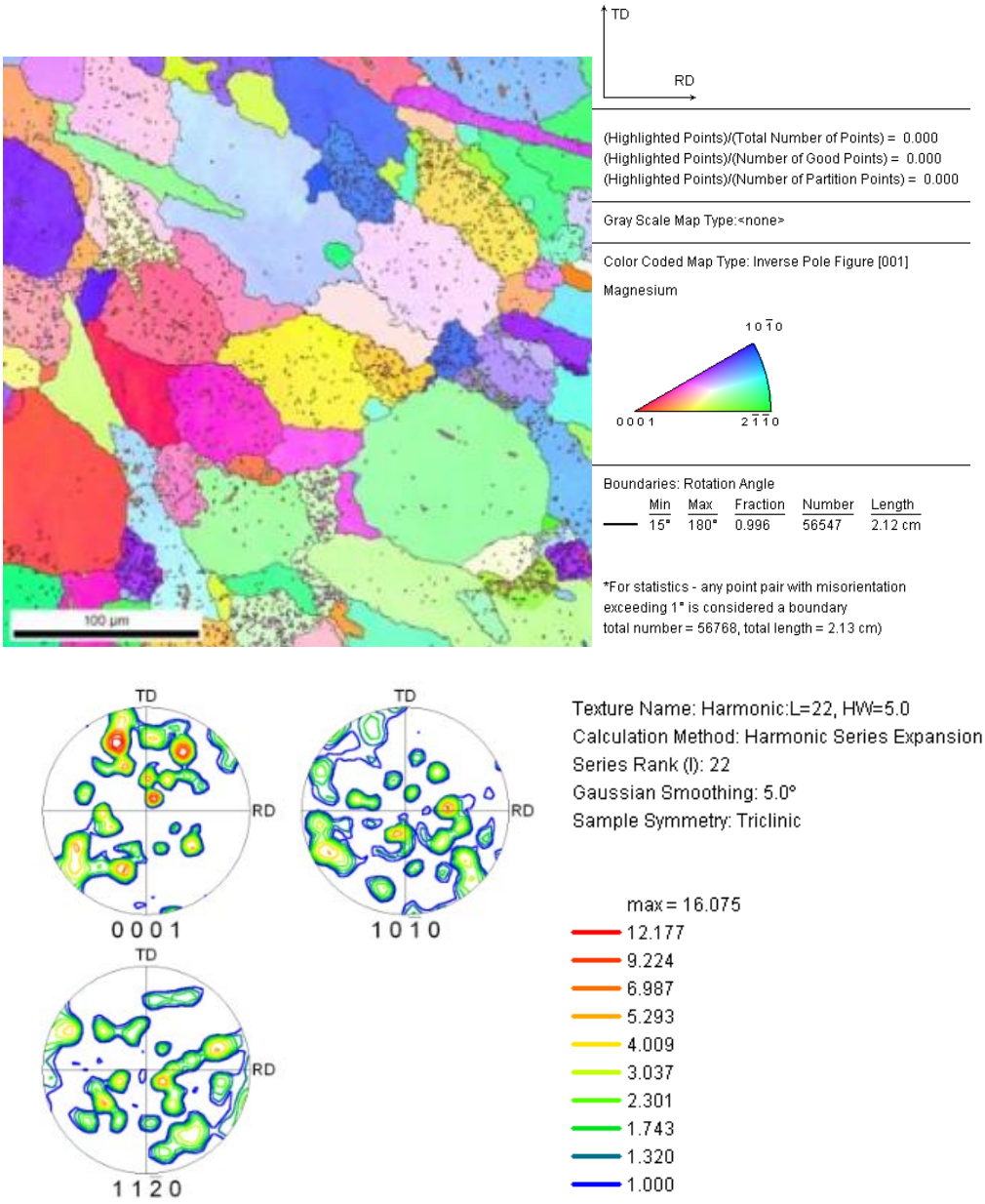

Figure 8.24: Detail of the EBSD image at the red rectangle section of the centre of the FZ and corresponding pole diagrams

This image is located 0.929 mm on the right compare to the reference point. It is on the middle of the weld because the specimen #6b-bead is 1.96 mm wide at the interface.
The images of the pole diagrams (**Fig. 8.24**) are cross sections of a 3D diagram of the orientation density function. The function describes the

density of the crystals oriented with those angles within the selected region of interest. The texture represented in the pole figures (**Fig. 8.24**) is not so strong according to the weak colours shown. A weak texture means that the material has isotropic behaviour. Only in the (0001) pole figure (**Fig. 8.24**) it is possible to see three maximum points. The three red points define three different texture components within selected region: g1 = (8 16 -24 -13) [22 -15 -7 8], g2 = (2 3 -5 35)[-28 -7 21 4] and g3 = (5 9 -14 12)[-8 4 4 5] obtained from ODF section at φ2 = 20° = const.
For the equiaxial grains (52.9 μm average diameter) in the centre of the FZ this texture components correspond to pyramidal crystal planes.
Further results with more and deeper EBSD analysis are shown in App. F.
As found in literature a significant grain coarsening in the HAZ can be observed in wrought AZ31 alloy [2].
The AZ31B magnesium alloy is susceptible to grain growth under the experimental condition, the grains grew in the HAZ with consequently decreasing mechanical properties.
Three different zones are clearly observable (**Fig. 8.25**): equiaxial grains in both FZ and BM, dendritic elongated grains at the interface HAZ-FZ.

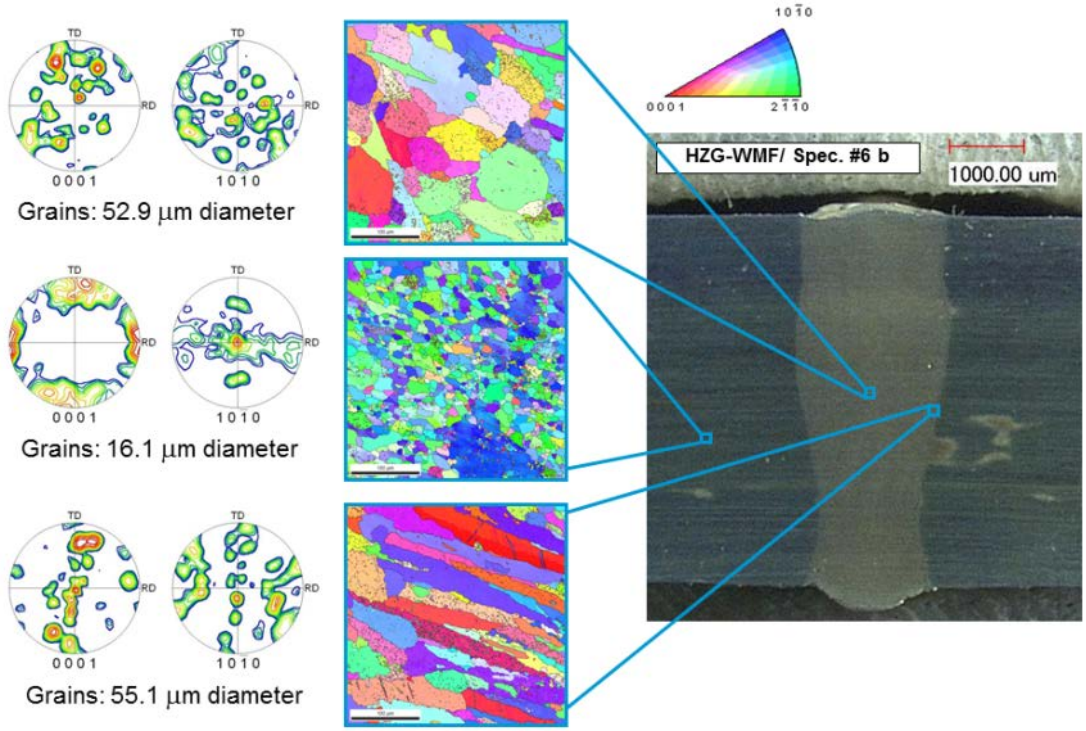

Figure 8.25: Detail of the EBSD images related to the macro-view cross section (sample #6b) from the top: fusion zone, base metal, heat affected zone and corresponding pole diagrams

The base material is primarily characterized by a <0001> // TD fiber texture and contains, as further component, the orientation (1 0 -1 0) [0 0 0 1]. This means that the basal planes are oriented substantially parallel to the rolled surface.
The <0001> // TD texture is held up the region near the fusion line (HAZ) and does not change. The average grain diameter of the upper-side heat-affected zone is 16.4 μm, almost identical compared to the base material with a grain size of 16.1 μm. In the gap between the upper and lower sheet and in the lower side area of the heat-affected zones the grains diameter decreases compared the initial base material.
One reason for this change could be that the heterogeneous nucleation was disturbed by the presence of a gap where the cooling process is in conjunction with the residual stresses distribution. The measure of 9.6 μm compared to the 16 μm of the BM could be due to the fact that the first measurement was made close to the rolled surface. In this case the plastic deformation may have created finer grains before the welding process. The measure on the BM instead was made slightly more down in the middle of the sheet.
At the edge between the heat affected zone (HAZ) and the fusion zone (FZ), the grain size increases significantly. The FZ is characterized in terms of morphology and micro-texture by heterogeneity. The transition region presents itself as a dendritic microstructure with grain sizes of 31.0 μm to 37.7 μm.
In the upper side of the weld there are mainly pyramidal crystal planes. In the gap region between the upper and lower plate there are only two dominant texture components for the transition zone. At the lower side edge area just one texture component is clearly marked.
Characteristics of the middle of the weld bead are the equiaxed dendritical colonies with colony sizes of 41.3 μm to 55.0 μm.
The pyramidal crystal planes dominate in the upper side and in the overlap zone, but without preferred orientations. In the bottom side a basal/transversal texture was observed.
In comparison with a AZ31 butt joint, the structural heterogeneity of overlap laser weld is significantly more pronounced in terms of morphology and micro-texture. As mentioned previously, the gap between upper and lower sheet metal appears to affect the heterogeneous nucleation in the gap region.

8.2.3 Results analysis for different laser welded joint shapes

The #3b process parameter conditions used to create the linear laser joint (**Section 7.2.2**) were selected as the reference for the other joint geometries to improve the fatigue behaviour. Therefore, based on the process

parameters shown in **Tab. 7.7**, three different laser welding paths (arc, circular and linear) were created (**Fig. 8.23**)

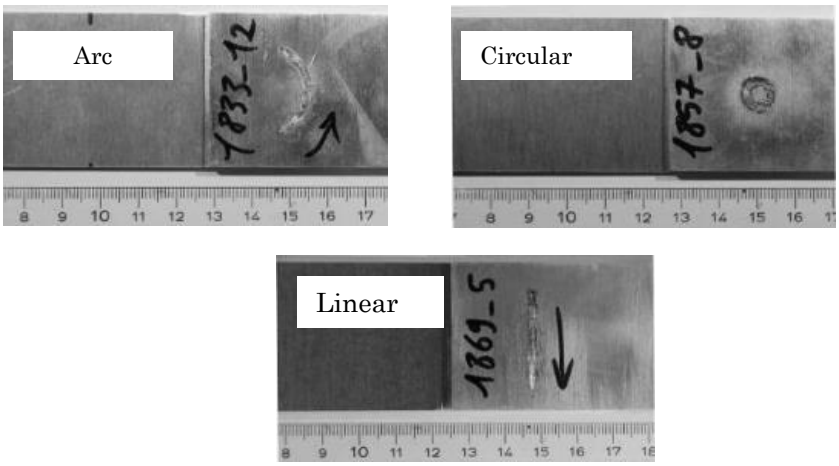

Figure 8.26: Top surface macro-view of the different laser joint paths

8.2.3.1 Tensile-shear testing and fractographic examination

In the tensile shear tests, the different laser welding paths showed almost the same load at failure (see **Graph 8.5**).

In the σ–ε graph shown in **Graph 8.4a**, an elongation under 1% may suggest the presence of brittle failure. Nevertheless the large displacement at failure (0.4 mm) with regards to the bead width (2 mm) indicates a ductile behaviour. Dividing by the resistant area, laser ring welds ultimately yielded larger shear strengths (100 MPa).

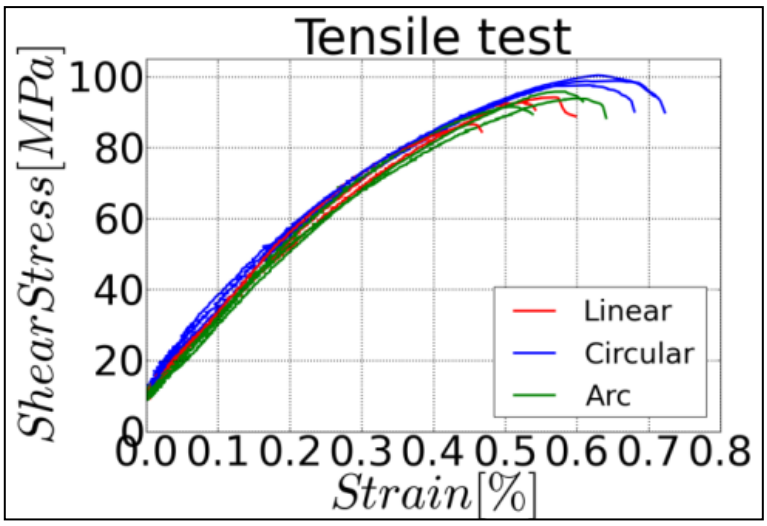

(a)

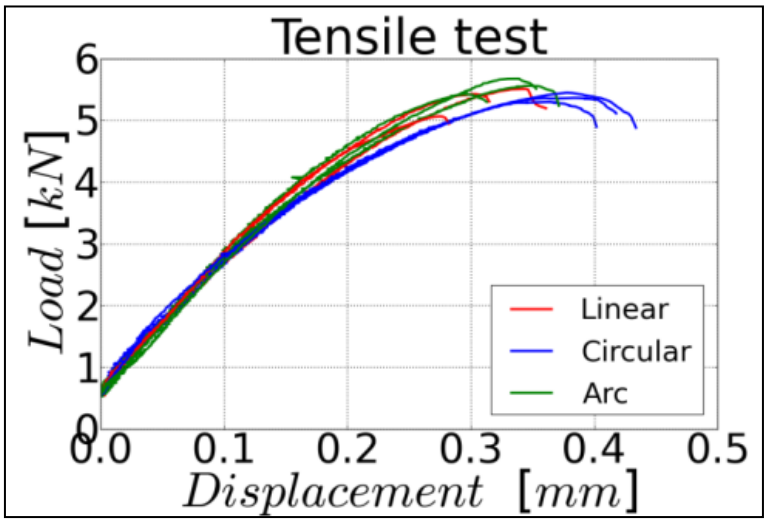

(b)

Graph 8.4: Tensile testing results for the different laser joint paths in overlap configuration: Stress-Strain (a) and Load-Displacement (b)

In the tensile shear tests, the laser welds showed the same load to failure for different welding paths. Dividing by the resistant area, the welds with the circular shape showed higher values in terms of elongation and ultimate shear stress. The resistant area values were acquired by the optical microscope.

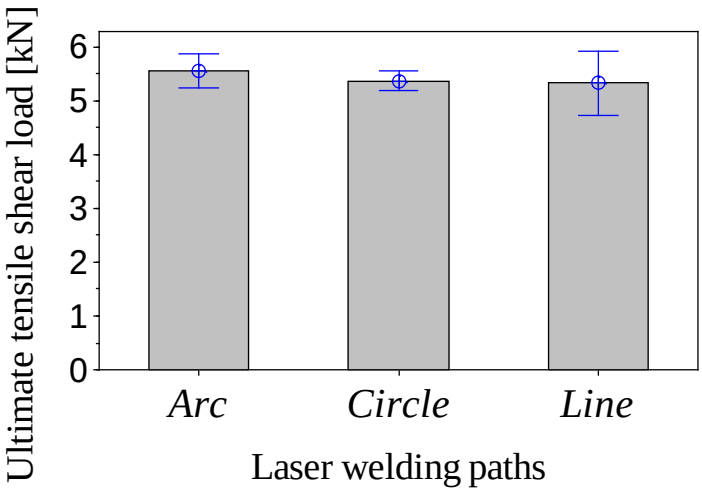

Graph 8.5: Ultimate tensile shear load (UTSL) for different laser welding paths

Table 8.6: Tensile shear test results for different laser welding paths

Sample	UTSL	UTSL av.	Std dev	Strain	Strain av.	Std dev	Meas. length	Bond area
	kN	kN	kN	%	%	%	mm	mm^2
Linear	5,51	5,33	0,24	0,59	0,53	0,07	60,3	58,5
	5,43			0,54			58,1	
	5,06			0,46			60,4	
Circular	5,36	5,37	0,08	0,71	0,70	0,02	58,7	54,8
	5,30			0,68			59,1	
	5,45			0,72			60,1	
Arc	5,56	5,55	0,13	0,64	0,59	0,05	57,9	59,3
	5,42			0,54			58,1	
	5,67			0,61			58,0	

In the tensile shear tests (**Table 8.6**), the laser welds showed the same load to failure for different welding paths. Fracture morphology of the overlap laser welded joint, after the tensile test, is shown in **Fig. 8.24**.
It is possible to see characteristic ductile failure behavior: the dimples are caused by fracturing of the elongated grains along the tensile direction during the test. There was no evidence of brittleness.

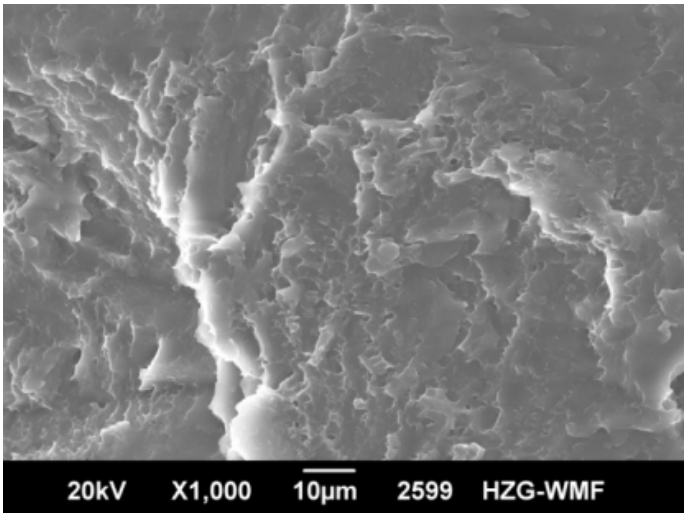

Figure 8.27: Dimple structure on fracture surface of a laser joint

The fracture plane was always on the interfacial one between the two sheets for all the tensile laser welded specimens (**Fig.8.25**). No pores appeared on the fracture surface of the fractured joints.
The bead width oscillations along the welding line (**Fig. 8.25**), were due to the keyhole instability from the beam-material interaction. The short

welding length (23.9 mm) was carried out for the most part in transient regime.

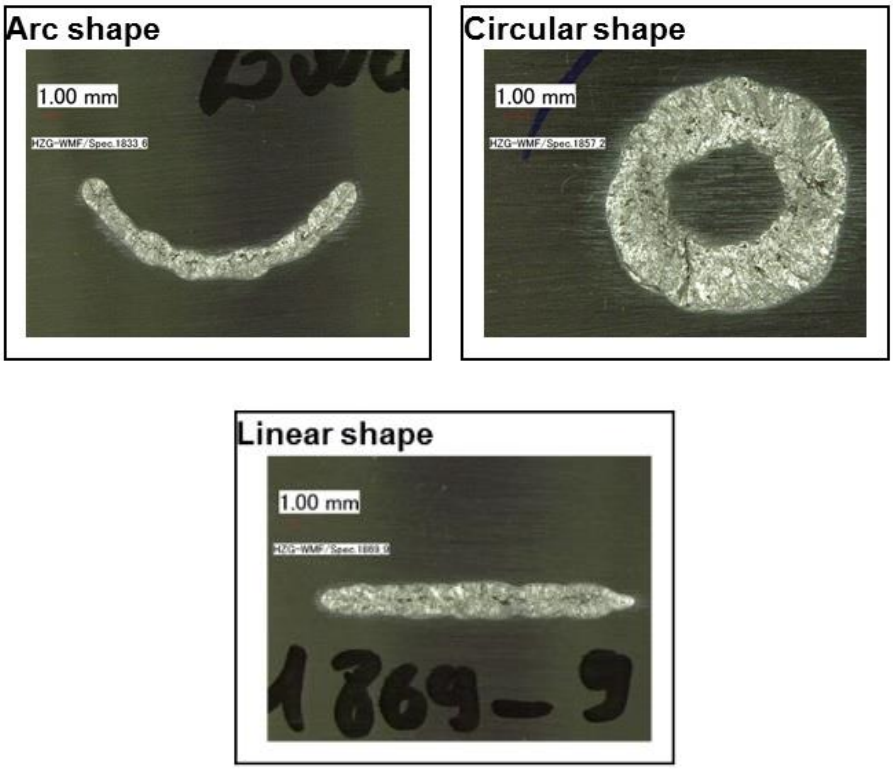

Figure 8.28: Fracture surfaces for different welding paths

8.2.3.2 Fatigue testing and failure modes

The load-lifetime data and corresponding L-N curves are shown in **Fig. 8.6**. The maximum load for the fatigue limit at 10^7 cycles is less than 1 kN. Furthermore, the linear, circular and arc variants show similar behaviour under a cyclic load. The cracks found at the end point of the ring laser weld experienced a fracture failure at a 0.6 kN load. The linear weld variant yielded the best behaviour in terms of high and low cycles fatigue and exhibited a fatigue limit of 0.9 kN. The different weld shapes have comparable effective bond areas. The different fatigue strengths for the three welding variants were not affected by the nominal stress value calculated by dividing the load by the effective bond area. Therefore, the fatigue life is primarily determined by the different stress distributions of the weld geometry. The geometry exhibiting the best fatigue behaviour was the linear shape perpendicular to the loading direction. For the linear laser joint, the load is uniformly distributed along the entire weld length, which reduces the local stress concentrations and retards crack nucleation.

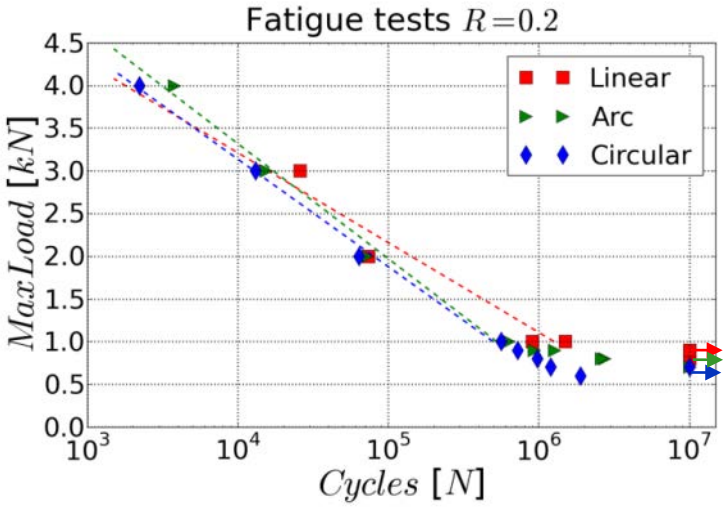

Graph 8.6: Load-life data for the different laser weld paths

The laser welds with arc shape failed in three different failure ways under cyclic loads: interfacial, along the weld bead and through-base material propagation (**Graph 8.7**).

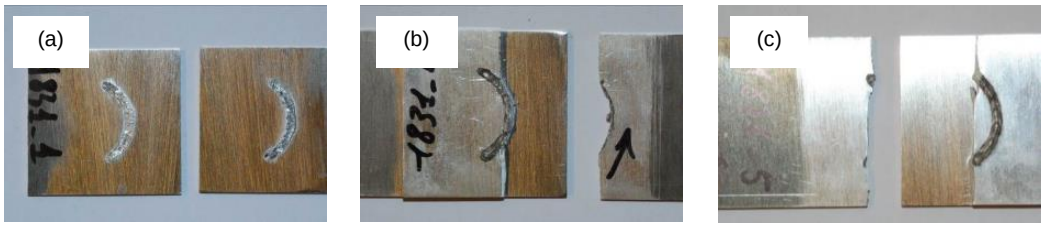

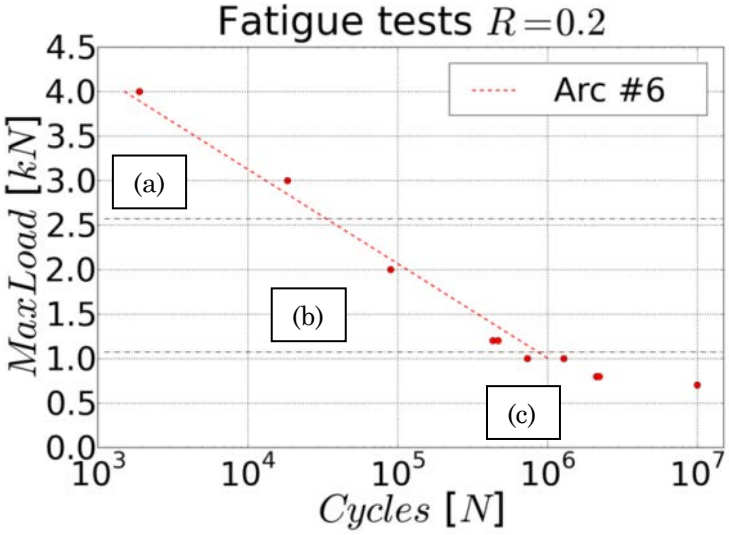

Graph 8.7: Fracture surfaces in fatigue arc shape laser joints test at different load levels represented in the L-N graph

The interfacial failure mode, occurred in the case of high load (above 3 kN), **Graph 8.7(a)**, the crack propagated within of the fusion material until the separation of the sheets.
In the case of medium load (**Graph 8.7(b)**, between 3 kN and 1 kN) the propagation proceeded along the transition zone between the base material and fusion bead until the crack growth through the coupon thickness. The final failure was reached without any interferences with the notches on the end or start points of the welds. This means that that the influence of the stress concentration due to the start/stop welding defects was low for this load range.
Finally in **Graph 8.7(c)**, in the through-base material propagation the cracks started indifferently from the start or the end point notches to proceed through the specimen width along a line perpendicular to the loading direction. This failure mode was observed only when the cyclic load was low (below 1 kN).
In the linear and circular laser joints fatigue tests the specimens showed always the same fracture behavior: in the case of the high cyclic load the separation of the coupons occurred as interfacial failure similar to the static rupture. With low cyclic loadings the crack started from the BM–HAZ interface in one of the two sheets. The crack propagated along the specimen on the side under tension (**Fig. 8.26**).

Figure 8.29: Cracks propagation in linear and circular laser welds

8.3 Comparison of the laser beam welds and resistance spot welds

For the mechanical properties comparison to RSW, 13 resistance spot overlap joints were created. The resistance spot weld had no apparent superficial defects (see **Fig. 8.27**) but had some distortion in the plates.

Figure 8.30: Top surface macro-view of the resistance spot welded joint

8.3.1 Metallographic investigation

X-ray analysis (**Fig. 8.31**) confirms the absence of macro pores or cracks within the welded material for both the laser and resistance spot welds. **Fig. 8.28(a)** shows a typical microstructure for a laser welded AZ31 joint. The transition zone between the base metal and fusion bead is excellently joined. As shown on the left side in **Fig. 8.28**(a) and (b), the base metal contains the typical rolled structure of an AZ31 wrought alloy with equiaxial grains (**Section 8.1.2**). A grain refinement occurs at the BM/FZ interface of the laser weld (**Fig. 8.28 a**) within the HAZ near the overlap zone (**Section 8.2.2.1***)*. A band region with columnar grains is present along the melt line shown in **Fig. 8.28(a)**. The dendritic growth direction of the columnar grains is perpendicular to the solid/liquid boundary. At the fusion boundary, the base material acts as a heat sink, and epitaxial growth occurs due to the large thermal gradient [23]. The FZ is on the right hand side of the dendritic band region. Equiaxial dendritic colonies form within the inner weld region. Some micro-pores are primarily located within the outer region of the laser welds. **Fig. 8.28(b)** shows the edge of the RSW nugget at the interface between the two rolled sheets. According to the literature results [24], the FZ in AZ31B magnesium alloy spot welds have an equiaxed dendritic structure.

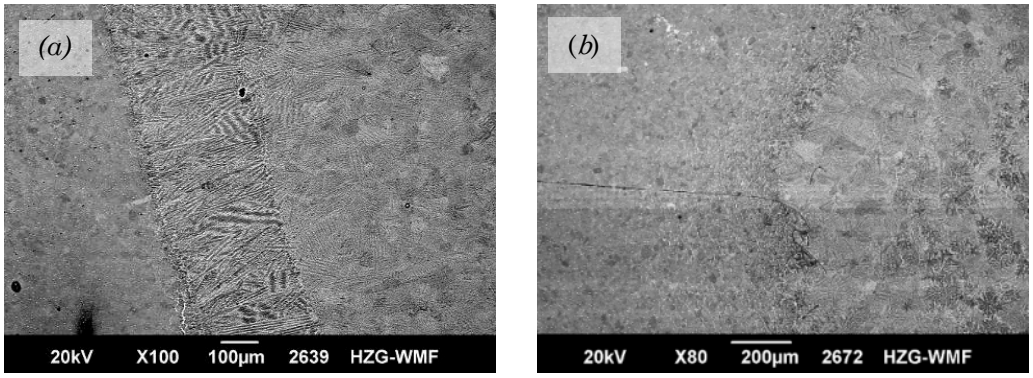

Figure 8.31: Microstructures of laser welds (a) and resistance spot welds (b) at the melting line

The black line in **Fig. 8.28b** represents the overlap plane, which continued inside the FZ because of the un-melted oxide layer (melting point at 2852°C) at the joint surface (**Fig. 8.29a**). These defects represent very sharp micro cracks and are preferential points for cracks initiation. Some micro cracks are present in the middle of the FZ of the RSW (Fig. 8.29c) and may weaken the spot welds under conditions that cause a fracture through the nugget.

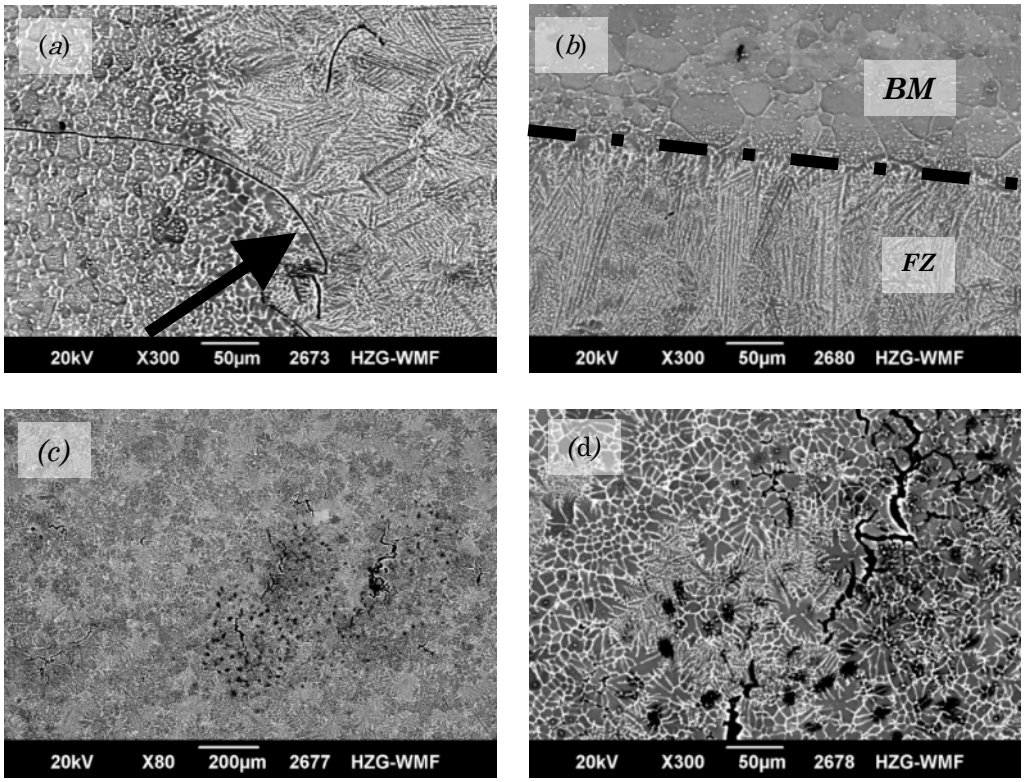

Figure 8.32: Microstructure of the welded metal at the BM/FZ interface (a), (b) and the centre of the RSW nugget (c), (d)

8.3.2 Microhardness

Graph 8.8 illustrates the microhardness of the base metals, weld metals, and HAZ for both LBW and RSW bead cross sections. The hardness profile of the laser welds (**Graph 8.8 a**) was affected by the dissimilar microstructures found in the different zones as discussed in Section 8.2.2.1. The obtained results indicate that the base metals are harder than the laser welded material. Increasing the grain size tends to decrease the hardness from the BM (approximately 58 *HV* 0.1) to the FZ (up to 40 *HV* 0.1). The microhardness profiles determined at different distances from the interface were not reported because they do not significantly differ from each other. Moreover, the results shown in **Graph 8.8 (b)** reveal that the RSW possess a broader softening due to the width of the FZ compared with the LBW.

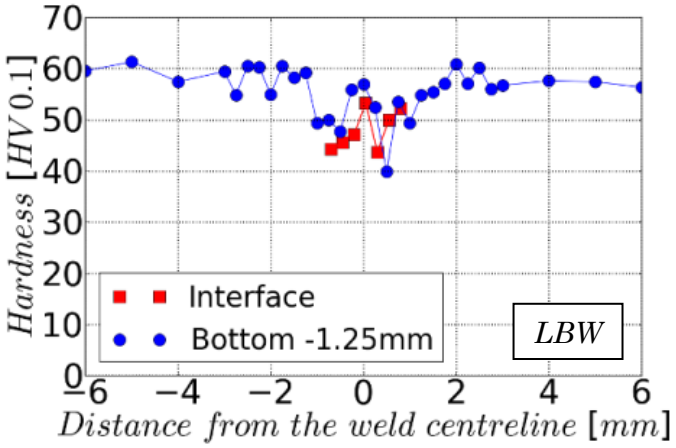

(a)

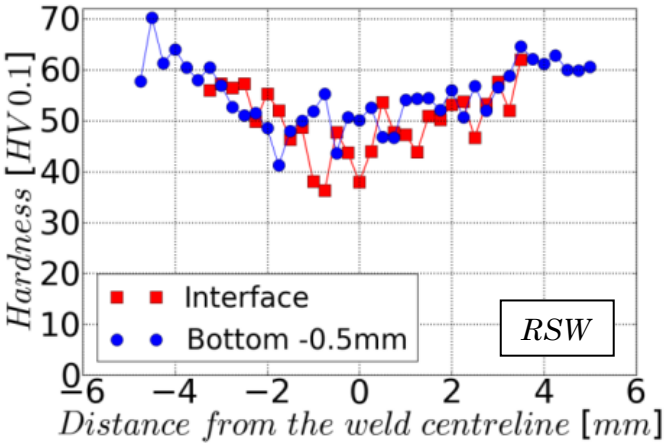

(b)

Graph 8.8: Comparison of the hardness (HV 0.1) profiles for the linear LBW (a) and RSW (b)

8.3.3 Tensile-shear testing

The effect of the different welding methods on the strength and failure mode was evaluated using tensile specimens tested under a quasi-static shear load. The relevant properties are shown in **Table 8.7**. All of the specimens failed at the interface. The ultimate tensile shear load (UTSL) determined for the linear laser welds was above 5 kN, while the resistance spot welds did not reach more than 4 kN on average. Dividing by the effective bond area, the ultimate tensile shear strength was approximately 40% of the base material for both the laser and resistance spot welds.
These are good results for linear laser welds, because it was used a shorter cycle time a smaller area necessary to join the two sheets, compared to the resistance spot joints.

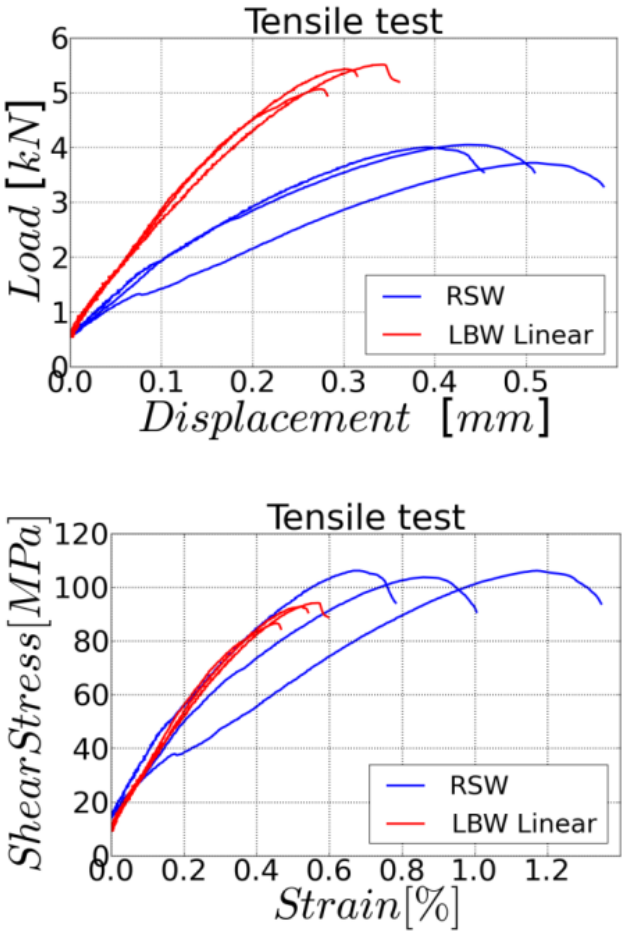

Graph 8.9: Tensile testing results for the linear laser welded and resistance spot welded joints

Table 8.7: Tensile shear test results for comparison between LBW and RSW

Sample	UTSL	UTSL av.	Std dev	Strain	Strain av.	Std dev	Meas. length	Bond area
	kN	kN	kN	%	%	%	mm	mm^2
Linear	5,51	5,33	0,24	0,60	0,54	0,07	60,3	58,5
	5,43			0,54			58,1	
	5,06			0,47			60,4	
RSW	3,72	3,92	0,18	1,35	1,04	0,28	43,4	35,1
	4,05			1,01			50,7	39
	4			0,78			58,0	37,7

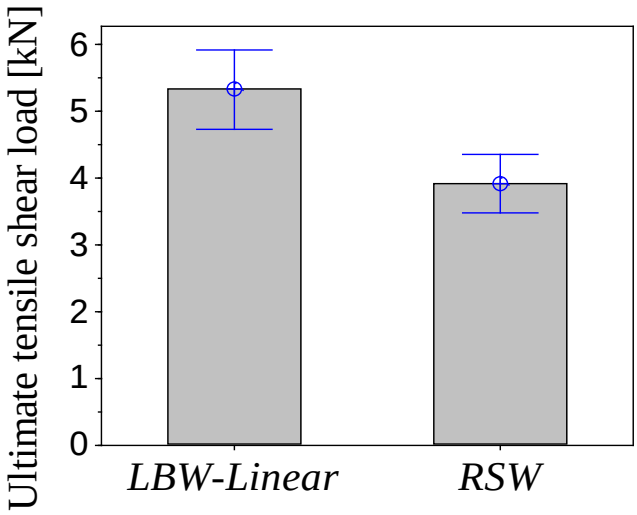

Graph 8.10: Ultimate tensile shear load comparison between LBW and RSW (95% CI for the mean)

8.3.4 Fatigue testing

The experimental load-lifetime data were compared in **Graph 8.11**; the obtained results are also compared with literature data on the state-of-the-art RSW of AZ31B alloys. S. B. Behravesh et al. [24] studied the mechanical behaviour of spot welds in a tensile–shear configuration for five sets of spot weld specimens prepared from sheets with 2 mm thickness and different welding parameters.
The following linear regression models was used to plot the fatigue L-N curves of selected joints for the comparison with the traditional resistance spot welds.

Regression Equation for linear LBW fatigue results

$Log_{10}(cycles) = 6,85839 - 0,860499\ Max\ Load$

Coefficients

Term	Coef	SE Coef	T	P
Constant	6,85839	0,290660	23,5959	0,002
Max Load	-0,86050	0,150096	-5,7330	0,029

Summary of Model

S = 0,248907 R-Sq = 94,26% R-Sq(adj) = 91,40%

Analysis of Variance

Source	DF	SS	MS	F	P
Regression	1	2,0363	2,0363	32,87	0,029
Residual Error	2	0,1239	0,0620		
Total	3	2,1602			

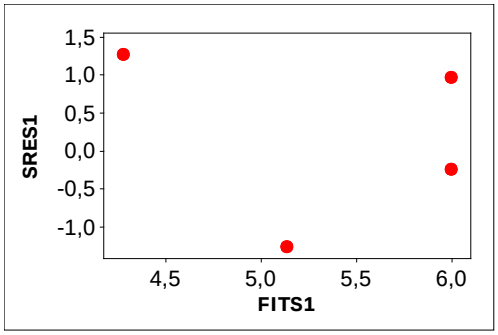

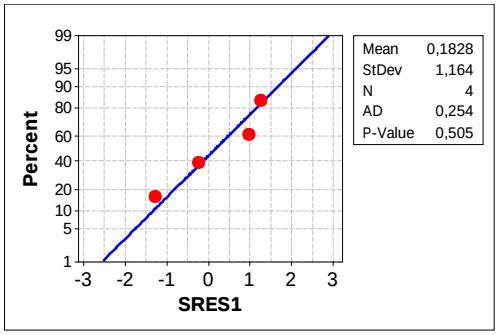

The standardized residuals did not reject the normality hypothesis. Moreover there are not standardized residual outliers with values not higher than 3 in modulus.

Regression Equation for RSW fatigue results

$Log_{10}(Cycles) = 7,17661 - 1,23318\ Max\ Load$

Coefficients

Term	Coef	SE Coef	T	P
Constant	7,17661	0,145376	49,3657	0,000
Max Load	-1,23318	0,074795	-16,4873	0,000

Summary of Model

S = 0,176295 R-Sq = 97,49% R-Sq(adj) = 97,13%

Analysis of Variance

Source	DF	SS	MS	F	P
Regression	1	8,4485	8,4485	271,83	0,000
Residual Error	7	0,2176	0,0311		
Total	8	8,6660			

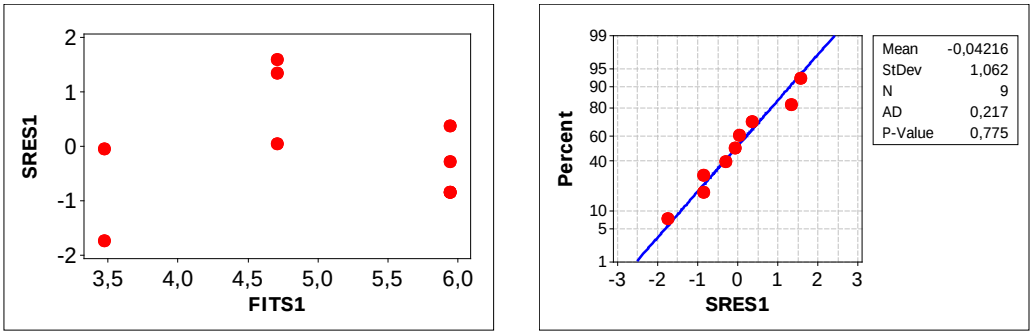

Again, the standardized residuals did not reject the normality hypothesis and there were not outliers.

According to this diagram shown in **Graph 8.11**, the difference in the fatigue behaviour between the laser and resistance spot welds is appreciable in the cycle regime up to 10^5 cycles. Below 10^5 cycles, the laser welded joints show an improved fatigue behaviour. However, only a minimal enhancement to the fatigue strength was achieved using the linear laser joints in the higher cycle regime (10^6 cycles).

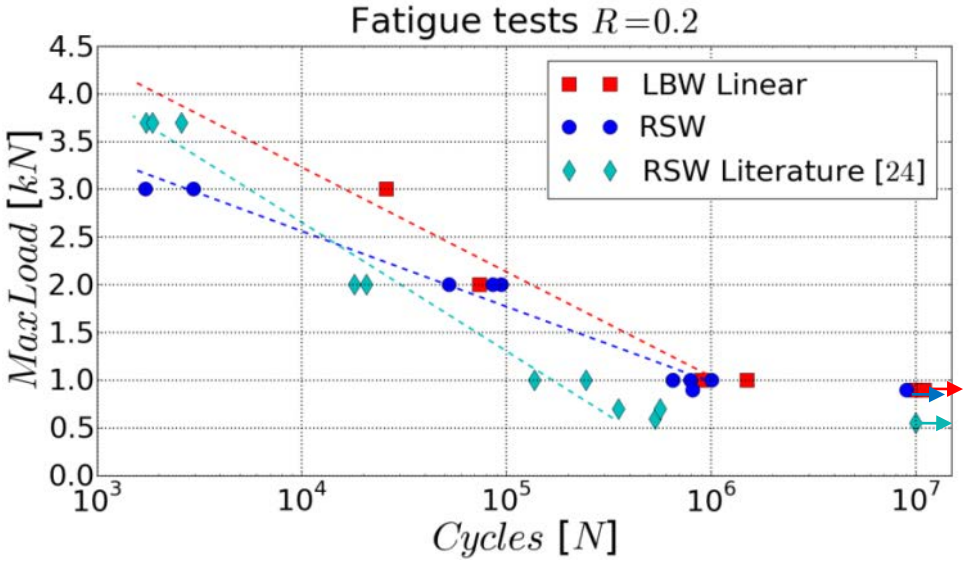

Graph 8.11: L-N curves to compare LBW and RSW

Both the laser beam and conventional resistance spot welds have cycles to failure values above the literature results [24] with maximum loads below 2 kN. The maximum load at 10^7 cycles was limited to 0.9 kN for RSW and linear LBW, 0.6 kN for the literature results.

8.3.5 Failure modes in fatigue tests

Fig. 8.30 presents an AZ31B Magnesium alloy overlap joint after failure. The RSW specimens failed in two different ways as reported for the laser ring welds. In low cyclic loads the failure mode is interfacial (**Fig. 8.30a**) , while the first point in tension on the spot at the HAZ is the preferential point of crack nucleation (**Fig. 8.30b**).

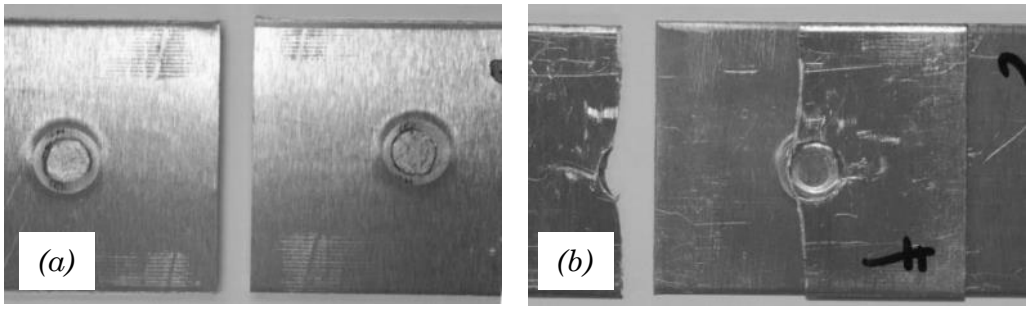

Figure 8.33: Fatigue fracture in RSW overlap joint for low (a) and high cyclic load

8.3.6 X-Ray analysis

X-ray investigation confirmed the absence of macro pores or cracks within the weld material for both laser (**Fig. 8.31 a**) and resistance spot weld (**Fig.8.30 b**).

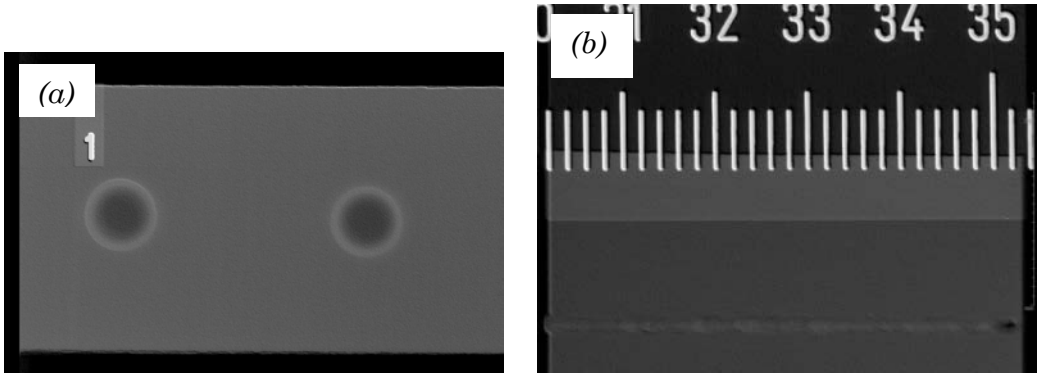

Figure 8.34: Laser weld (a) and resistance spot nuggets (b) from x-ray investigation

8.3.7 Energy Dispersive X-ray analysis

In **Fig. 8.32** is shown the lines profile analysis chosen to investigate the chemical composition (EDX) starting from the base material to reach the weld metal.

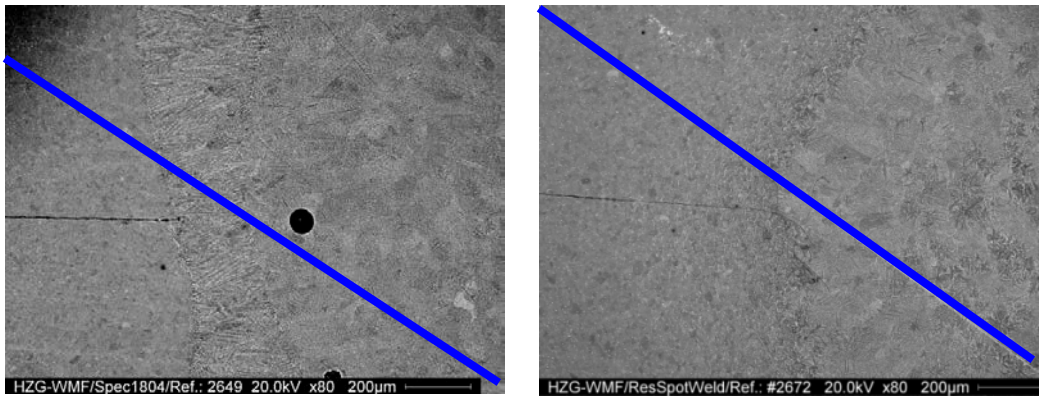

Figure 8.35: EDX analysis path for laser (a) and resistance spot (b) bead cross section

The EDX analysis summarized in the **Graph 8.12** indicated a decrease of the Mg concentration from base material to the laser beam weld.
The weld comprises a plurality of inclusion particles with high Mn concentration and diffusion-related segregation. The segregations are mainly localized near the inclusion particles.
The lap weld is characterized by a heterogeneous solubility condition. In the base material, however, the Mn-containing inclusion particles are less abundant and slightly coarser. Within the laser FZ, the Al distribution is characterized by strong fluctuations: the segregation due to diffusion during the solidification lead to the formation of intermetallics ($Al_{12}Mg_{17}$) at the grain boundary. The segregation of $Al_{12}Mg_{17}$, occurred because of the high cooling rate after the welding process, is the first cause of the decreasing of pure Mg: in fact the $Al_{12}Mg_{17}$ phase needs around 50% of Mg weight percentage. Moreover, the Mg matrix loses the hardening of the base material due to the fine distributed included particles.
A second reason resulting in the change of Mg distribution and content is the low melting point of magnesium (lower than Al). Magnesium was easily vaporised during the laser welding and formed the metal steam which may cause the decreasing in Mg content (**Graph 8.12**). A second path for EDX investigation of laser beam weld is reported in App. G.

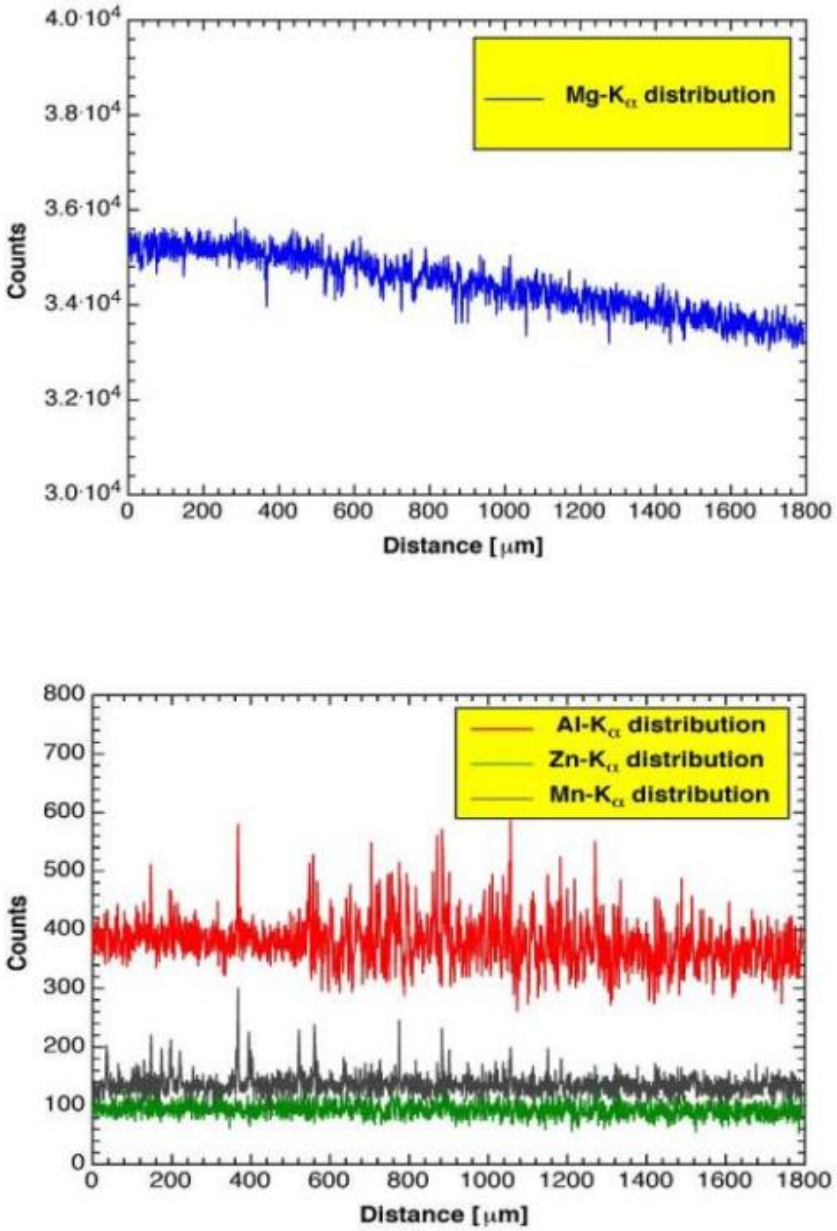

Graph 8.12: Alloying elements profile data from BM to FZ of laser beam weld

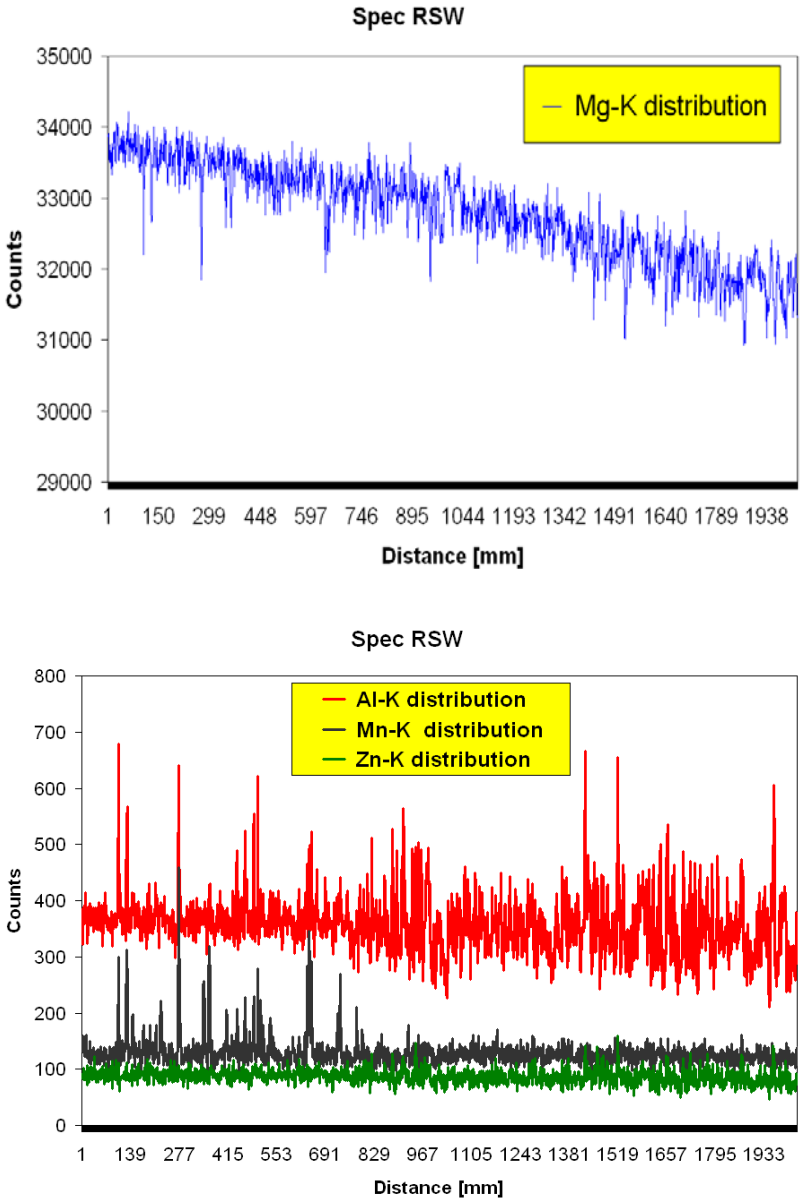

Graph 8.13: Alloying elements profile data from BM to FZ of resistance spot weld

As well as for the laser beam weld, the resistance spot weld line profile analysis indicates an decreasing Mg content from base material to the RSW nugget (**Graph 8.13**). Within the melted material Al content shows strong fluctuations.

9 Conclusions

The study offers an in-depth comparison between two welding processes, the resistant spot welding and the laser welding respectively, the first (RSW) being the reference state of the art of the industrial practice and the second one the new competitor, when a common magnesium alloy, AZ31B, is the investigated material. The main conclusions can be summed up in the following points:

- The laser welding process for Mg overlap joints has been developed and optimised. Defect-free laser beam welds with suitable geometries were created during this work.

- The tensile tests revealed that different laser weld shapes, such as linear, ring and arc, did not significantly affect the mechanical behaviour of the AZ31B over-lap joints under a tensile load. Moreover, the linear laser beam weld overlap joint yielded the optimum fatigue behaviour. Resistance spot welding formed voids and microcracks within the fusion zone. Such complications were not observed for the optimised laser beam welds.

- The hardness of the fusion zone was lower than the base material.

- Linear LBW required a shorter joining cycle time than the resistance spot joints and exhibited a higher ultimate tensile shear load. The tensile test comparison divided the UTSL by the effective joint area; the ultimate tensile shear strength was comparable for both RSW and LBW.

- The low cycle fatigue LBW showed enhanced strength relative to the RSW. Both the LBW and RSW improved relative to the literature values for conventional RSWs of AZ31 Mg alloys.

- Compared with conventional resistance spot welds, laser welded joints possessed improved fatigue behaviour and a comparable tensile shear strength.

- The investigation began with a basic study on the mechanical performances of different laser welding paths (linear, circular, C-shape). Since they were produced with a Laser Short Distance process, where the heat source is composed of a single laser beam,

the optimised experimental condition can also be implemented with a remote scanner welding system to increase the throughput, e.g., in the automotive industry.

References

[1] S. Giammarinaro, S. Riekehr, B. Previtali, M. Hibben, N. Kashaev. Mechanical Performance of Laser Welded and Resistance Spot Welded Overlap Joints from Magnesium AZ31B Sheets, JOM-17 Proc. (2013)

[2] X. Cao, M. Jahazi, J.P. Immarigeon, W. Wallace. A review of laser welding techniques for magnesium alloys, *J. Mater. Process. Technol.,* **171** (2006) 188–204

[3] J. Zhu, L. Li, Z. Liu. CO2 and diode laser welding of AZ31 magnesium alloy, *Appl. Surf. Sci.*, **247,** (2005), 300–306

[4] H. Hiraga, T. Inoue, S. Kamado, Y. Kojima. Effects of the shielding gas and laser wavelength in laser welding magnesium alloy sheets, *Quart. J. Jpn. Weld. Soc.,* **19 (4)**, (2001), 591–599

[5] Y.J. Quan, Z.H. Chen, X.S. Gong, Z.H. Yu. Effects of heat input on microstructure and tensile properties of laser welded magnesium alloy AZ3, *Mater. Characterizat.,* **59**, (2008), 1491-1497

[6] Z. Wang, M. Gao, H. Tang, X. Zeng. Characterization of AZ31B wrought magnesium alloy joints welded by high power fiber laser, *Mater. Characterizat.,* **62**, (2011), 943-951

[7] R.S. Coelho, A. Kostka, H. Pinto, S. Riekehr, M. Koçak, A.R. Pyzalla. Microstructure and mechanical properties of magnesium alloy AZ31B laser beam welds, *Mater. Sci. Eng. A* **485,** (2008) 20–30

[8] William M. Steen, Mazumder Jyotirmoy. Laser Material Processing, 4th ed. 2010, Springer

[9] S. Beretta, B. Previtali. Estimate of maximum pore size in keyhole laser welding of carbon steel, *Sci. Technol. Weld. Join.,* 2009, VOL 14 NO 2, 106-116

[10] 'Specimen dimensions and procedure for shear testing resistance spot, seam and embossed projection welds', ISO 14273, 2000

[11] R. Arias, Á. Prada, E. Vaamonde, A. Vandewynckèle, D. Gutierrez, A. Lara, M. García. Laser welding applied to advanced high strength steels for automotive applications, Paper 1002, ICALEO - LIA 2010, 371-379

[12] S. Daneshpour, S. Riekehr, M. Kocak, V. Ventzke, A. I. Koruk. Failure behaviour of laser spot welds of TRIP800 steel sheets under coach–peel loading, *Sci. Technol. Weld. Join.,* **12** , (2007), 508–15.

[13] P. Martinson, S. Daneshpour, M. Koçak, S. Riekehr, P. Staron. Residual stress analysis of laser spot welding of steel sheets, *Mater. Des.,* **30** (2009) 3351–3359

[14] S. Daneshpour, S. Riekehr, M. Kocak and C. H. J. Gerritsen. Mechanical and fatigue behaviour of laser and resistance spot welds in advanced high strength steels*, Sci. Technol. Weld. Join*., 2009, VOL 14 NO 1, 20-25

[15] 'Resistance spot welding – Destructive tests of welds – Method for the fatigue testing of spot welded joints', EN ISO 14324, 2003

[16] N. Kishore Babu, S. Brauser, M. Rethmeier, C.E. Cross. Characterization of microstructure and deformation behaviour of resistance spot welded AZ31 magnesium alloy, *Mater. Sci. Eng. A* **549**, (2012), 149-156

[17] G. Padmanaban, V. Balasubramanian. Optimization of laser beam welding process parameters to attain maximum tensile strength in AZ31B magnesium alloy, *Opt. Laser Technol.,* **42**, (2010), 1253–1260

[18] L.D. Scintilla, L. Tricarico, M. Brandizzi, A.A. Satriano. Nd:YAG laser weldability and mechanical properties of AZ31 magnesium alloy butt joints, *J. Mater. Process. Technol.,* **210**, (2010) 2206–2214

[19] Afia Kouadri-David. Welding of Thin Light Alloys Sheets by CO2 Laser Beam: Magnesium Alloys, *PSM Team*, INSA of Rennes, LGCGM, (2011)

[20] R.S. Coelho, A. Kostka, H. Pinto, S. Riekehr, M. Koçak, A.R. Pyzalla. Microstructure and residual stresses in dissimilar Mg-Al-Zn-alloy single overlap laser beam welds, *Mater. Sci. Forum*, **571-572** (2008), 361-366

[21] G.L. Liang, G. Zhou, S.Q. Yuan. Study on hybrid heat source overlap welding of magnesium alloy AZ31B, *Mater. Sci. Eng. A* **499**, (2009), 93–96

[22] G. Song, L. Liu, P. Wang. Overlap welding of magnesium AZ31B sheets using laser-arc hybrid process, *Mat. Sci. Eng. A*, **429** (2006) 312–319

[23] Sindo Kou. Welding metallurgy, 2nd Ed. 2003, Wiley-Interscience,

[24] S. B. Behravesh, H. Jahed, S. Lambert. Characterization of magnesium spot welds under tensile and cyclic loadings, *Mater. Design*, **32**, (2011), 4890-4900

[25] M. Gao, S. Mei, Z. Wang, X. Li, X. Zeng. Process and joint characterizations of laser–MIG hybrid welding of AZ31 magnesium alloy, *J. Mat. Proc. Tech.*, **212**, (2012) 1338– 1346

[26] N. Pierron , P. Sallamand, S. Mattei. Study of magnesium and aluminum alloys absorption coefficient during Nd:YAG laser interaction, *Applied Surface Science* , **253**, (2007) 3208–3214

[27] L. Liu, G. Song, G. Liang, J. Wang. Pore formation during hybrid laser-tungsten inert gas arc welding of magnesium alloy AZ31B—mechanism and remedy**,** Mat. Sci. Eng. A, Vol 390, **15** (2005)

[28] H. Zhao, T. DebRoy. Pore formation during laser beam welding of diecast magnesium alloy AM60B –mechanism and remedy*, Weld. J.*, **80** (2001) 204S–210S

[29] E. Capello. Le lavorazioni industriali mediante laser di potenza, *ed. Clup*, 2003

[30] T. Kim, J Kim, Y. Hasegawa, Y. Suga. Welding of AZ31B Magnesium Alloy by YAG Laser/ TIG Arc Hybrid Welding Process, *Mat. Sci. F.*, Vols. **449-452**, (2004), pp. 417-420

[31] Z. Sun, D. Pan, J. Wei. Comparative evaluation of tungsten inert gas and laser welding of AZ31 magnesium alloy, *Sci. Technol. Weld. Joining,* **7** (2002) 343.

[32] A. Weisheit, R. Galun, B.L. Mordike. CO_2 laser beam welding of magnesium based alloys, *Weld. J.,* **77** (1998) 149s.

[33] I.S. Krull. Trace Metal Analysis and Speciation*, J. Chromatography*, Library Vol. 47, Elsevier

[34] L. Liu, L. Xiao, J.C. Feng, Y.H. Tian, S.Q. Zhou, Y. Zhou. Resistance Spot Welded AZ31 Magnesium Alloys, Part II: Effects of Welding Current on Microstructure and Mechanical Properties, DOI: 10.1007/s11661-010-0339-7, *The Minerals, Metals & Materials Society and ASM International 2010*

[35] S. Hassanifard, M. Zehsaz. The effects of residual stresses on the fatigue life of 5083-O aluminum alloy spot welded joints, *Procedia Engineering 2* (2010) 1077–1085

[36] L. Xiao, L. Liu, D.L. Chen, S. Esmaeili, Y. Zhou. Resistance spot weld fatigue behavior and dislocation substructures in two different heats of AZ31 magnesium alloy, *Mat. Sci. Eng. A* **529** (2011) 81– 87

[37] F. Hayat. The effects of the welding current on heat input, nugget geometry, and the mechanical and fractural properties of resistance spot welding on Mg/Al dissimilar materials, *Mat. Des.* **32** (2011) 2476–2484

[38] D.Q. Sun, B. Lang, D.X. Sun, J.B. Li. Microstructures and mechanical properties of resistance spot welded magnesium alloy joints, *Mat. Sci. Eng. A* **460–461** (2007) 494–498

[39] R. F. Qiu, S. Satonaka, C. Iwamoto. Mechanical properties and microstructures of magnesium alloy AZ31B joint fabricated by resistance spot welding with cover plates, Sci. Tech. of Weld. and Join., Vol 14, n 8 (2009) 697

[40] J. D. Shearouse, Magnesium and magnesium alloys, *Mat.of Eng.*, **6-84**

[41] H. Shi, R. Qiu, J. Zhu, K. Zhang, H. Yu, G. Ding. Effects of welding parameters on the characteristics of magnesium alloy joint welded by resistance spot welding with cover plates, *Mat. and Des.*, **31** (2010) 4853–4857

[42] P. Uslu, B. Demir, F. Hayat. Effect of the weld current on tensile shear properties of the RSW junctions AZ31 Mg alloy sheet, *6th IATS'11*, Elazığ, Turkey

[43] M. Ishak, K. Yamasaki, K. Maekawa. Laser Welding of Thin Sheet Magnesium Alloys, (2012) *Nd YAG Laser*, ISBN 978-953-51-0105-5

[44] S.M. Chowdhury, D.L. Chen, S.D. Bhole, E. Powidajko, D.C. Weckman, Y. Zhou. Microstructure and Mechanical Properties of Fiber-Laser-Welded and Diode-Laser-Welded AZ31 Magnesium Alloy, *Met. Mat. Trans. A* VOL. 42A (2011)

[45] Y.S. Yang, S.H. Lee. A study on the joining strength of laser spot welding for automotive applications, *J. Mat. Proc. Tech.*, **94** (1999) 151-156

[46] Son, Wang J., Liang G., Liu L. Microstructure and mechanical properties of wrought magnesium alloy AZ31 welded by laser-TIG hybrid, *Trans. Nonferrous Met. Soc. China*, Vol. 14, **3** (2004)

[47] D.Ren, L. Liu, Y. Li. Investigation on overlap joining of AZ61 magnesium alloy: laser welding, adhesive bonding, and laser weld bonding, *Int J Adv Manuf Technol* (2012) 61:195–204

[48] Joachim Berkmanns, Mark Faerber. Laser welding, Linde gas

[49] H. Haferkamp, F. von Alvensleben, I. Burmester, M. Niemeyer. The characteristics of laser beam welded magnesium alloys, *Proc. ICALEO*, Part 2, (1997). 140–149

[50] A. G. Demir, B. Previtali, D. Colombo, Q. Ge, M. Vedani, L. Petrini, W. Wu, C. A. Biffi. Fiber laser micromachining of magnesium alloy tubes for biocompatible and biodegradable cardiovascular stents*, Proc. SPIE 8237, Fiber Lasers IX: Tech., Syst. Appl.,* (2012) 823730

[51] M. K. Kulekci. Magnesium and its alloys applications in automotive industry, Int. J. Adv. Manuf. Tech., 39 (2008), 851–865

[52] Metals Handbook, ASM. Beck, Technology of Magnesium and Its Alloys. *Annual Book of Standards*, ASTM. Publ. of the Dow Chemical Co.

[53] E. A. Brandes, G. B. Brook. Smithells Light Metals Handbook, *Butterworth-Heinemann*, 1998

[54] D. Havrilla, R. Brockmann. Remote Laser Welding in Automotive Production, *TRUMPF*

[55] D. C. Montgomery. Design and Analysis of Experiments, John Wiley & Sons, 2008

APPENDIX A– Effect of the Shielding Gas flow variation on the UTSL

The first tensile tests were performed to understand if the shielding gas flow rate can affect the static mechanical performance. The decreasing gas flow was tested on the #3 process condition (see Section 7.2.1). 40 mm linear welds were produced on 40 mm width samples, then they were cut obtaining a width of 33.7 mm to compare the Tensile tests results to the RSW data, with same welding area, removing notches on the edge and the start-up effect.

	Sample	Sh. gas above [L / min]	Sh. gas below [L / min]
	1799	10 Ar	4.5 He
	1800	10 Ar	8 He
	1801	10 Ar	12 He

Tensile tests results

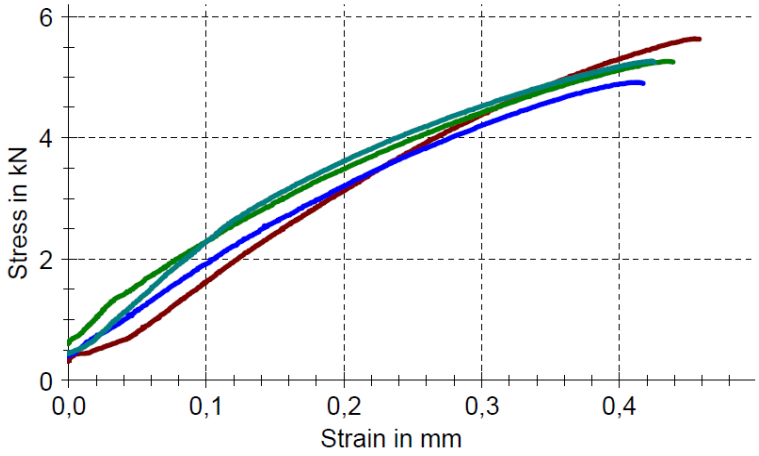

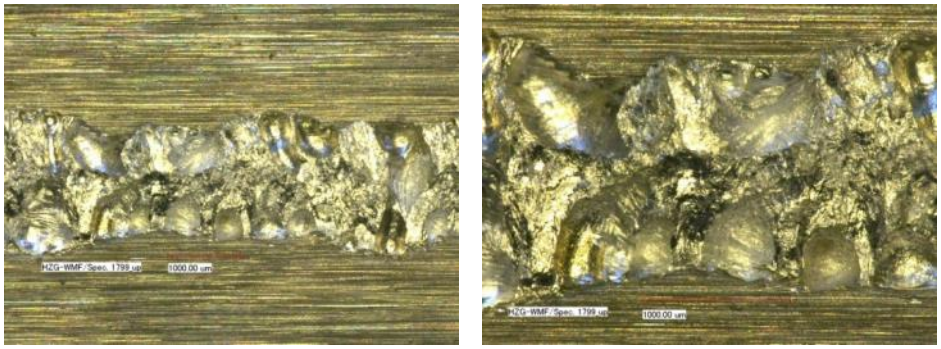

Figure: Fracture analysis of the *1799 sample– upper sheet*

From the microscope picture is possible to see the big amount of pores on the interface area due to the oxide layer on the plate surface.

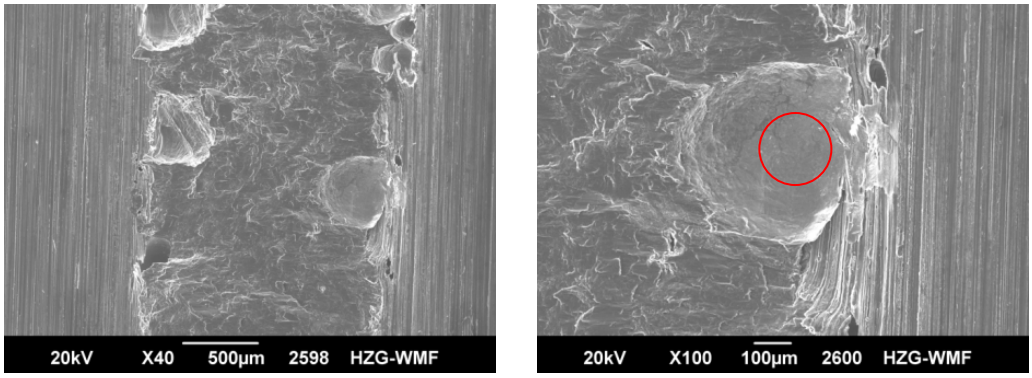

Figure: Fracture analysis of the *1801 sample– upper sheet*

On the right and left of the bead is observed the rolling direction.
The smooth surface of the pores (red circle) is due to the pressure of the entrapped gas.
In the right picture the dimples are oriented in the load direction.

In the x1000 magnification pictures is possible to see characteristic ductile fracture behaviour: fracture surfaces exhibit dimple structure. The dimples are flat cause of the shear stress during the tensile test. There is no evidence of brittleness.
The variation of flow rate does not seem to affect the tendency to pores formation, neither the fracture behaviour.
The pores are distributed at the edge of the welding because during the process gases try to leave the bead through the gap between the two sheets.
The weld width is decreasing with increasing the Helium flow rate (1801) due to the higher cooling rate.
The middle condition bead shows more stable process behaviour (10 Ar / 8 He).
Good results reached, compared to the RSW Max Tensile shear load (4.7 kN found in Literature – 9.5 mm nugget diameter – 1.2 mm thick, Shi et al. 2010): in the presence of pores - no grinded surfaces - more than 5 kN reached with LBW.

By increasing the Helium backside shielding flow:

- UTS unaffected
- No Drop-out visible variations
- No qualitative superficial shape variations

APPENDIX B – Surfaces preparation before the process

Grinding of the surface was one of the key factors to reduce porosity and increase the failure strength.

In the figure below some pores appear in the welded samples.
The degreasing by acetone did not prevent porosity in any experimental conditions as shown in the picture. From the microscope picture is possible to see the big amount of pores on the interface area due to the oxides and contamination present on the plates surfaces. The pores are distributed along the edge of the weld because the gases try to leave the bead through the gap between the two sheets during the solidification .

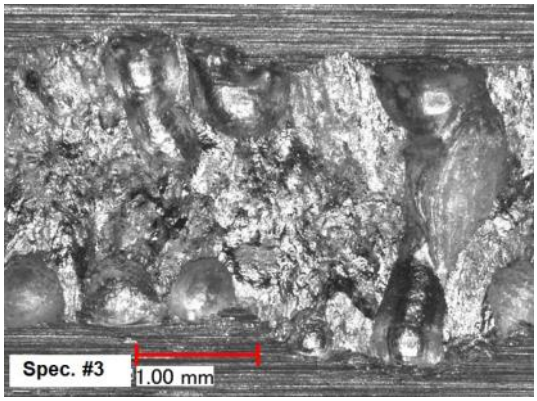

Figure: Welding plane at the sheets interface

Weld Quality improvement

The #3, #2 and #6 experimental conditions were improved by changing process parameters:

- the laser power was decreased to reduce the big drop out effect due to the low viscosity of magnesium;
- both shielding gas (Ar and He) were tested to investigate the presence of ripples and notches on the surface;
- all the surfaces involved in the joint were grinded because degreasing by acetone did not prevent porosity.

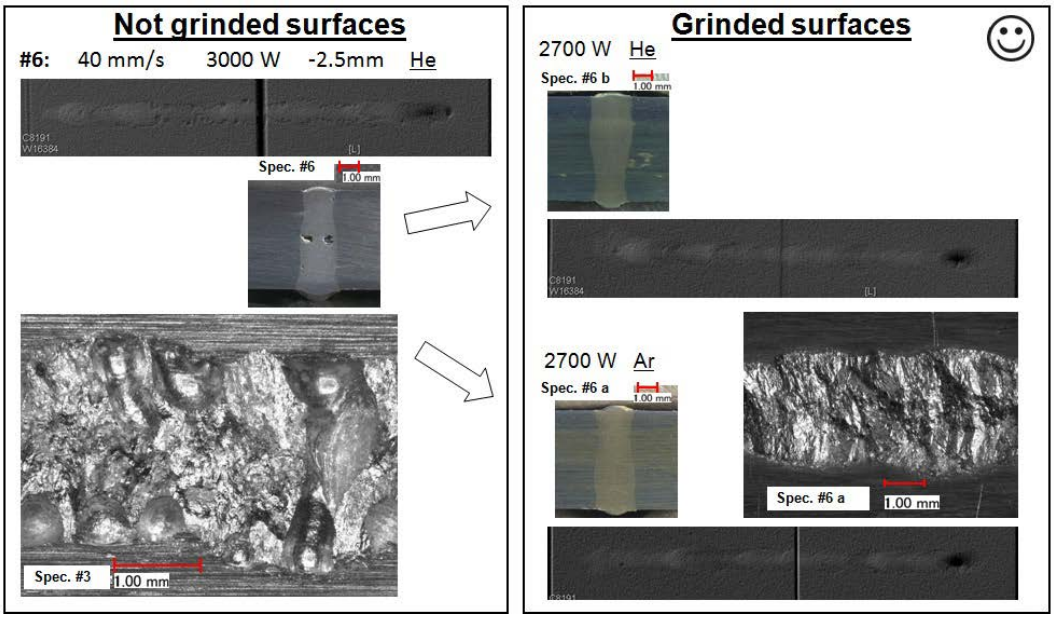

With the developed surface preparation, welds with optimal bead geometry, without cracks and pores were acquired. As showed on the x-ray pictures of the example above, pores disappeared, by grinding the surfaces.
Compared to the first factorial experiments, by decreasing Power: different bead shapes were obtained; less Drop Out effect; wider Upper Width and smaller Lower Width;
Samples with Argon as shielding gas, show a bigger **Interface With** but also more **ripples** on the upper surface (#2a, #3a). The first will increase the Ultimate Tensile Stress but the ripples could be reduce the fatigue behaviour.

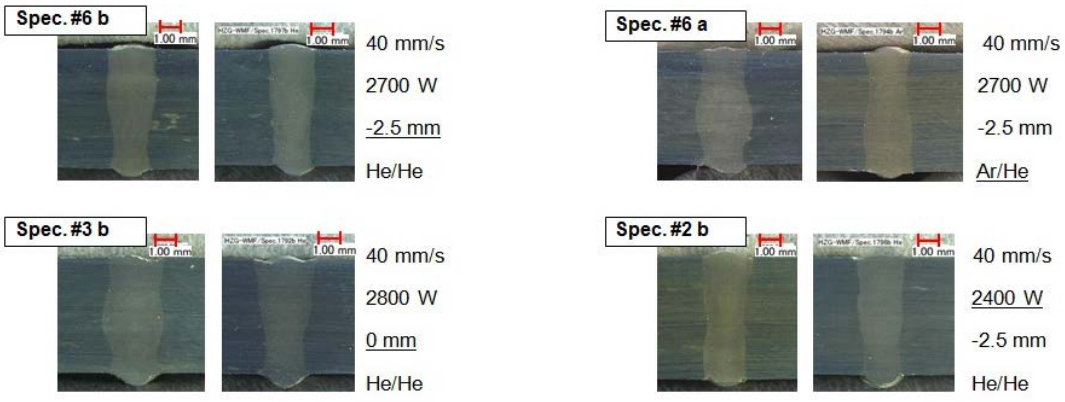

The different bead shapes, seen between the two cross sections of the cut, showed the laser bead instability.

APPENDIX C – Mechanical comparison between arc welds under different conditions

Another condition (#6 a) was chosen to investigate the process-property-performance relationships on the laser beam welds with arc path.

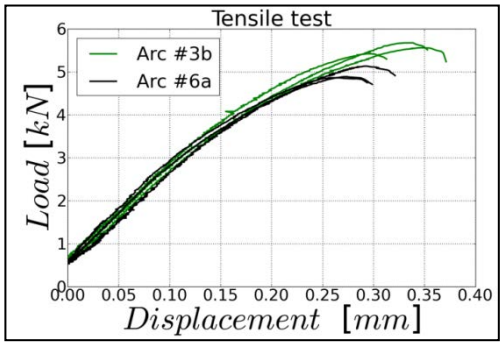

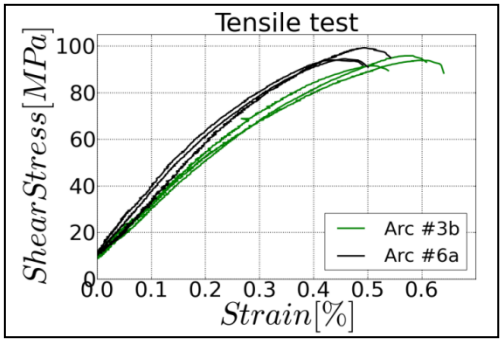

The difference shown in the load-displacement graph was due to the changed joint resistant areas.

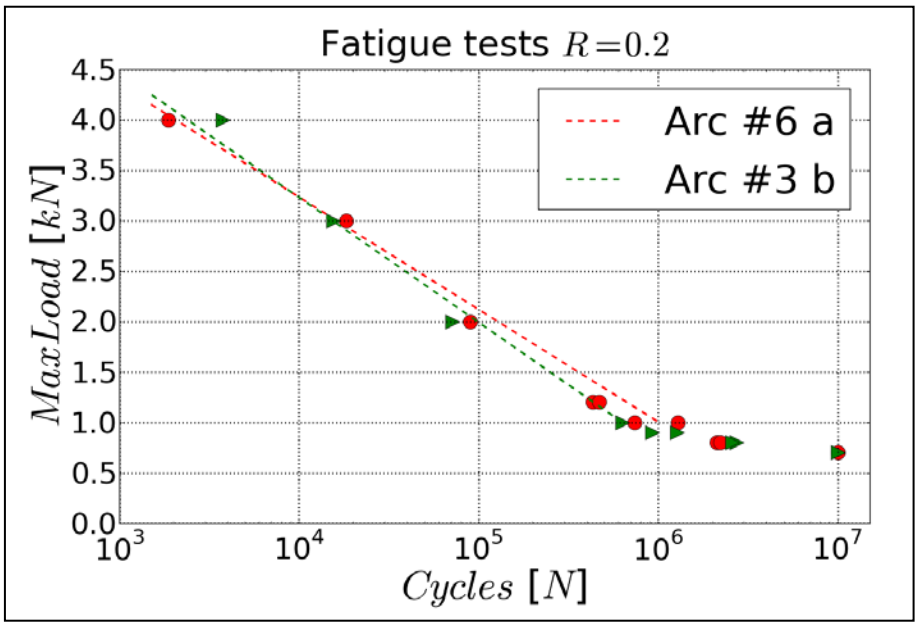

In both cases, for tensile shear and fatigue tests, the mechanical properties were comparables changing the main laser parameters (laser power, focus position and shielding gas).

APPENDIX D – The full EBSD analysis

Overlap zone on the left side (reference position/see SEM image #2638):

EBSD data: Spec6b_#01/Position: x_0 = 6.742 mm, y_0 = -36.855 mm

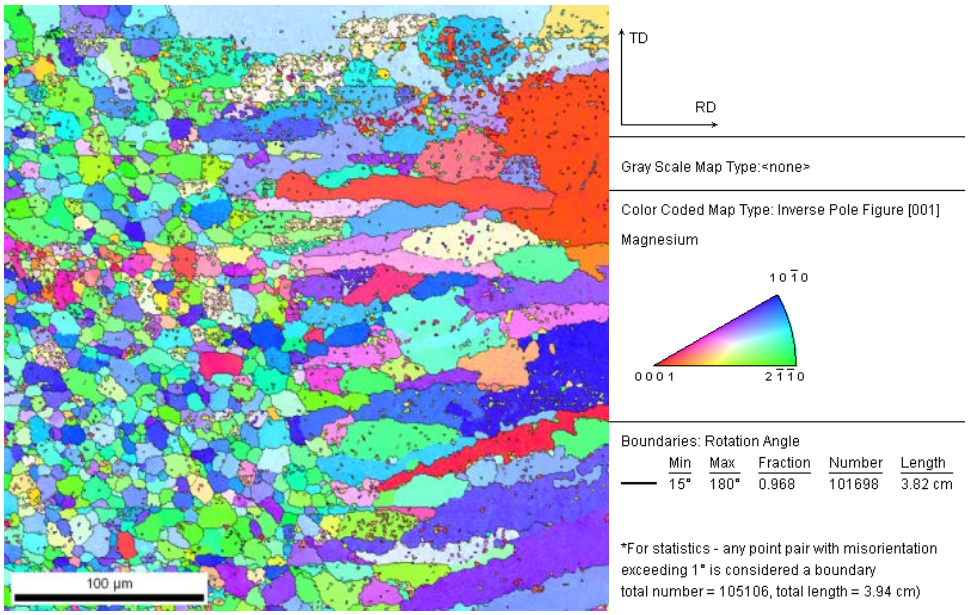

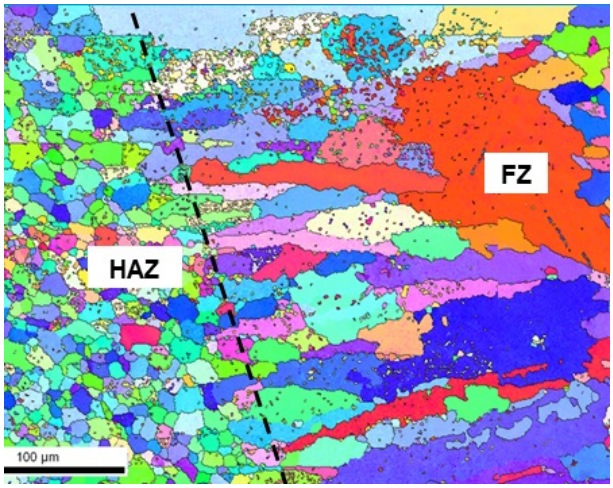

Transitional area on the top side (see SEM image #2639):
EBSD data: Spec6b_#08/Position: x_0 = 6.742 mm, y_0 = -37.276 mm

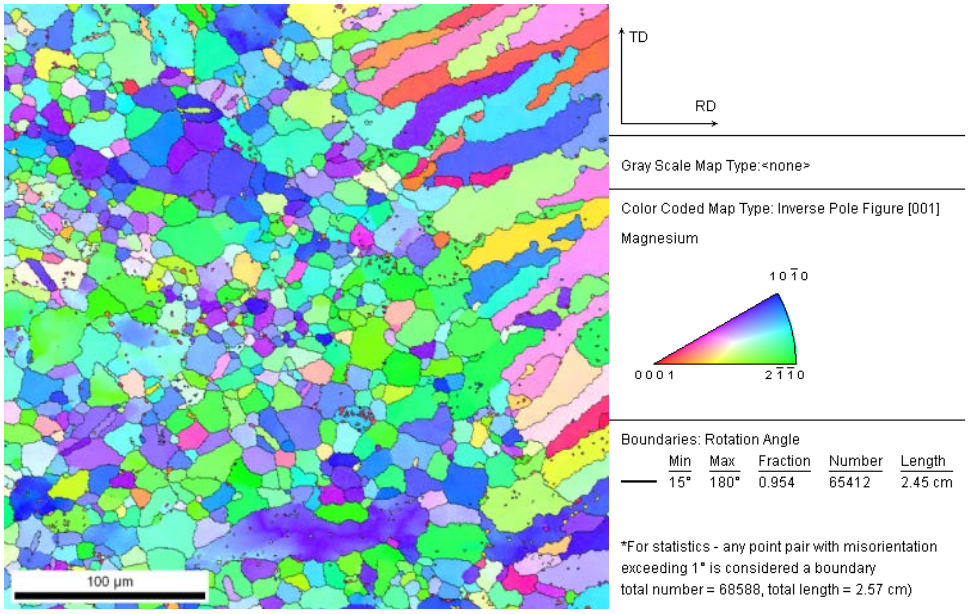

a) section of HAZ

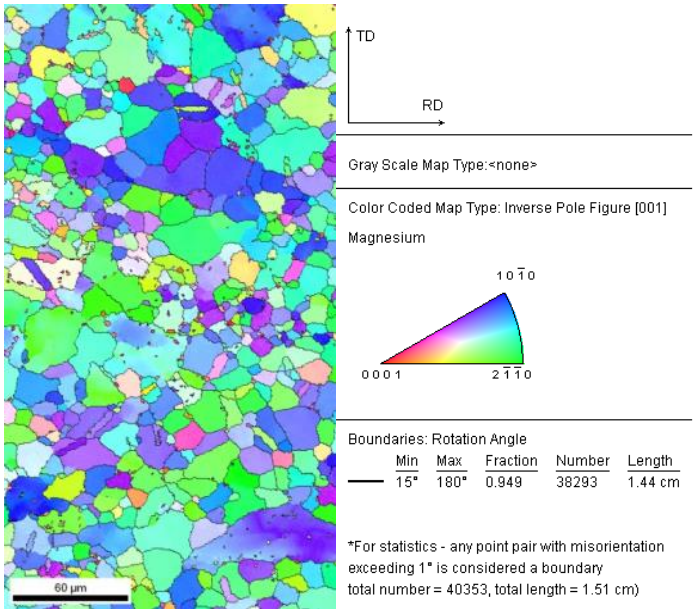

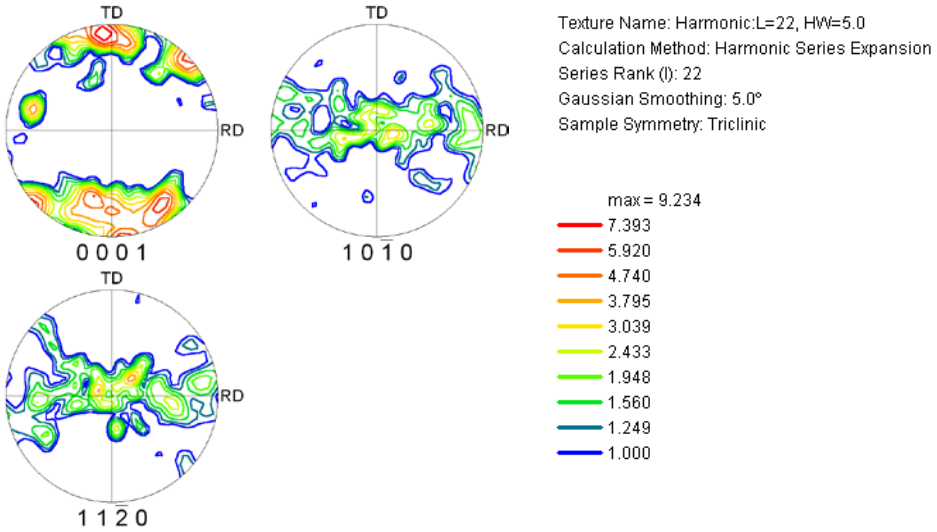

- specimen location: HAZ at melting line on left top side;
- grain size: 16.4 µm;
- texture components within selected region of interest: <0001>//TD fibre texture
- equiaxial grains, prismatic crystal planes are pronounced.

b) section of laser beam weld

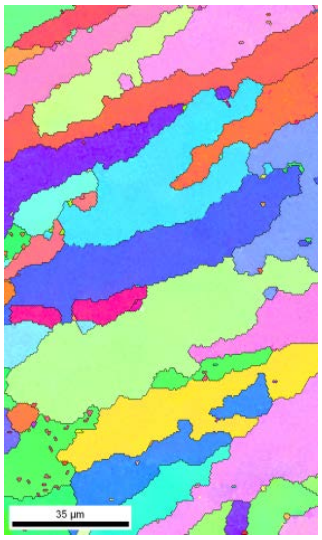

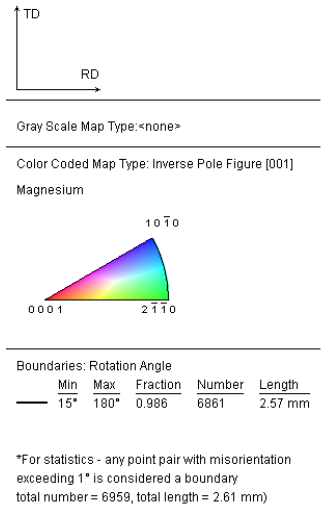

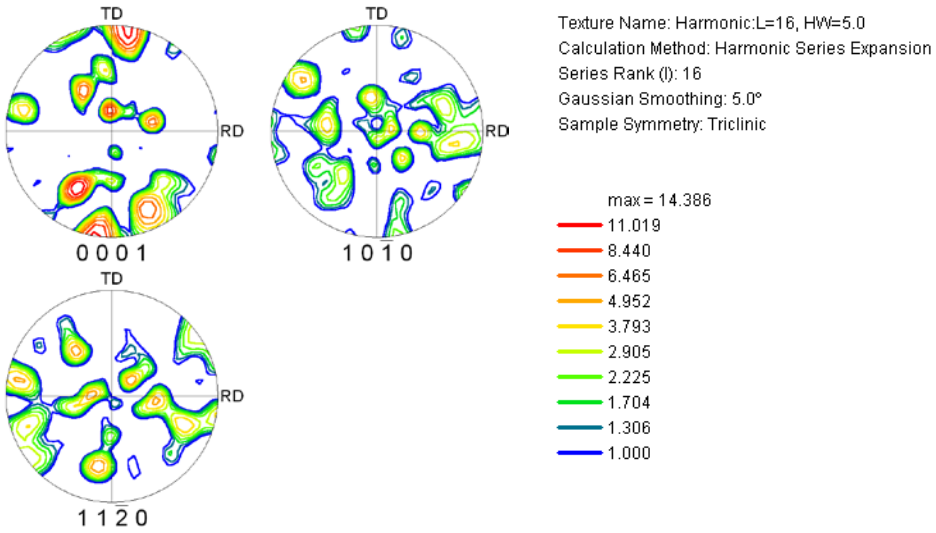

- specimen location: fusion zone at melting line on left top side;
- grain size: 31.0 µm;
- dissolution of <0001>//TD fibre texture and splittings resulting in further texture components: (0 3 -3 1)[-19 9 10 3], (0 3 -3 2)[18 -14 -4 15], (0 3 -3 5)[12 -1 -11 6], (2 2 -4 7)[-11 -3 14 12], (2 2 -4 -3)[-12 17 -5 10], (1 1 -2 9)[-16 13 3 1];
- dendritic grains, prismatic and pyramidal crystal planes are pronounced.

Transitional area on the bottom side (see SEM image #2640):
EBSD data: Spec6b_#09/Position: x_8 = 7.191 mm, y_0 = -36.345 mm

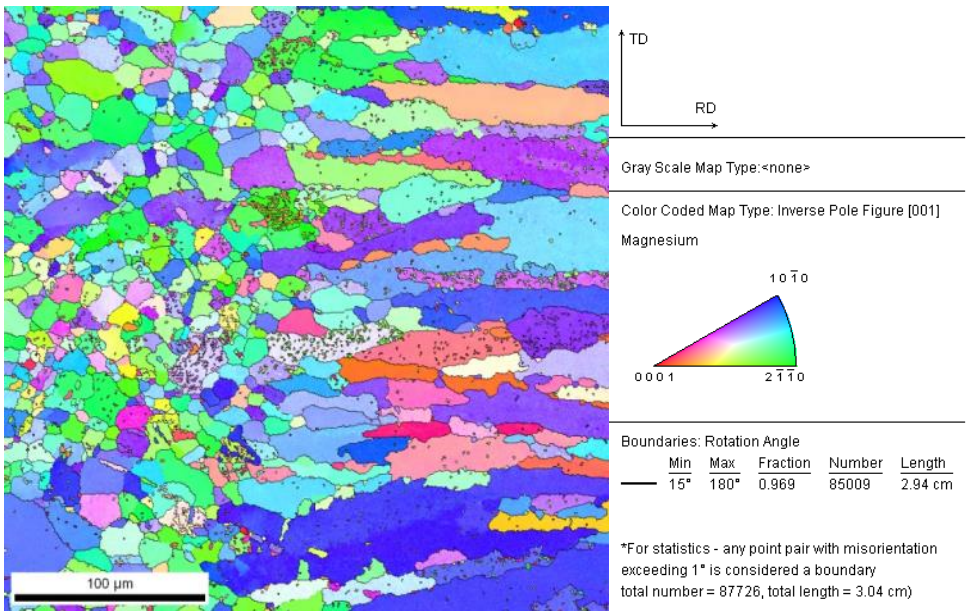

a) section of HAZ

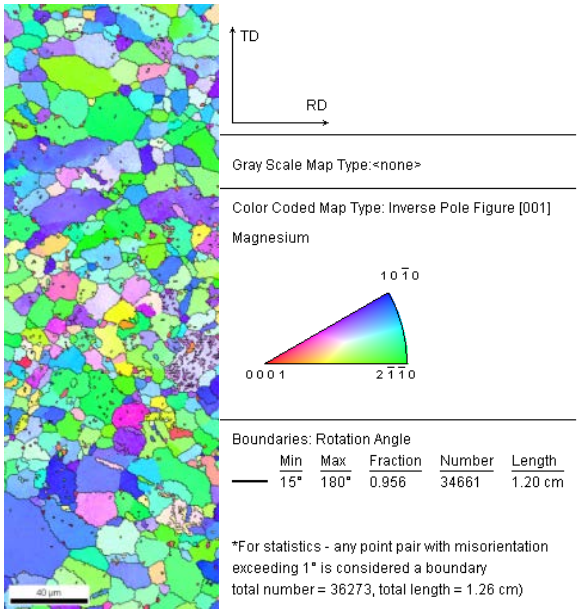

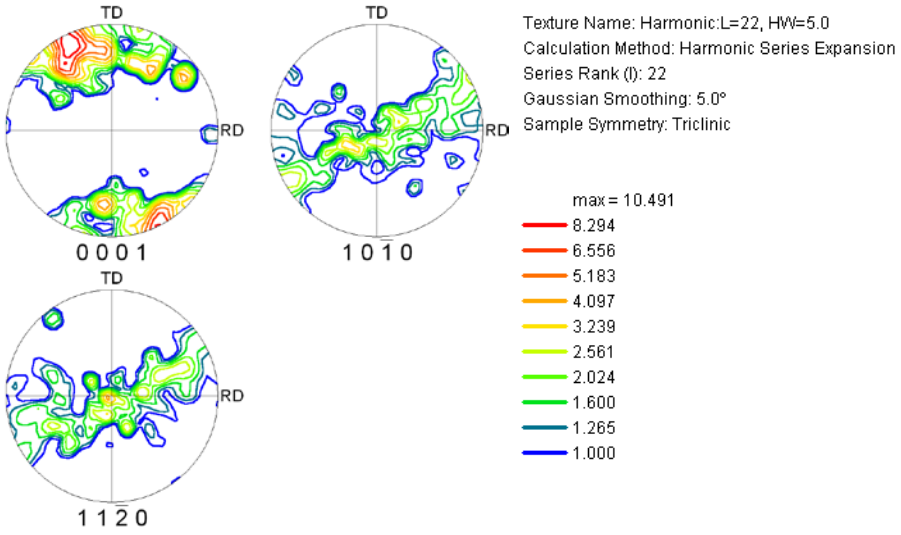

- specimen location: HAZ at melting line on left bottom side;
- grain size: 14.5 μm;
- texture components within selected region of interest: <0001> fibre texture@θ = 15°;
- equiaxial grains, prismatic crystal planes are pronounced.

b) section of laser beam weld

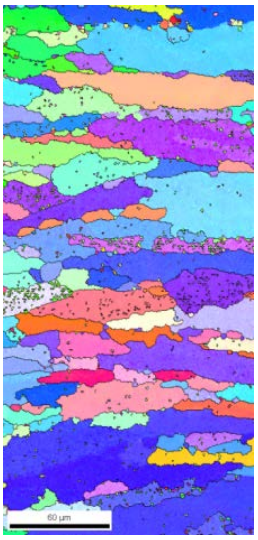

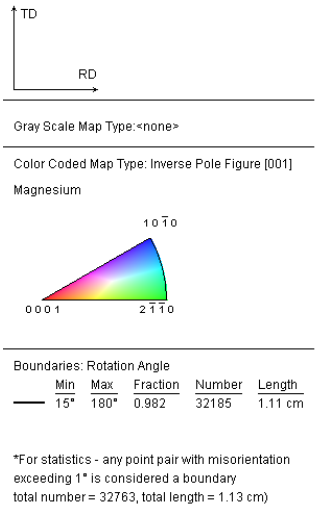

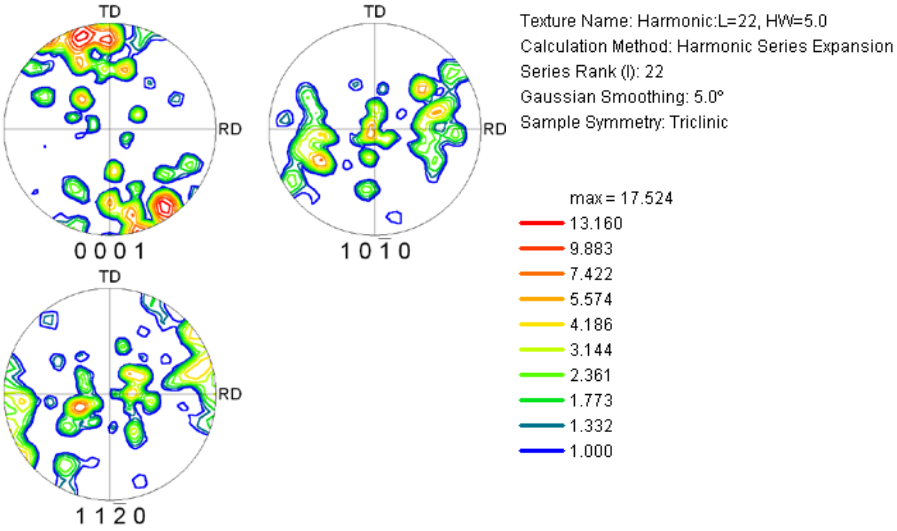

- specimen location: fusion zone at melting line on left bottom side;
- grain size: 36.6 µm;
- texture components: (1 0 -1 0)[1 1 -2 0]@θ = 15°
- dendritic grains, prismatic and pyramidal crystal planes are pronounced.

Fusion zone on the top side (see SEM image #2643):
EBSD data: Spec6b_#07/Position: x_6 = 6.635 mm, y_6 = -37.276 mm

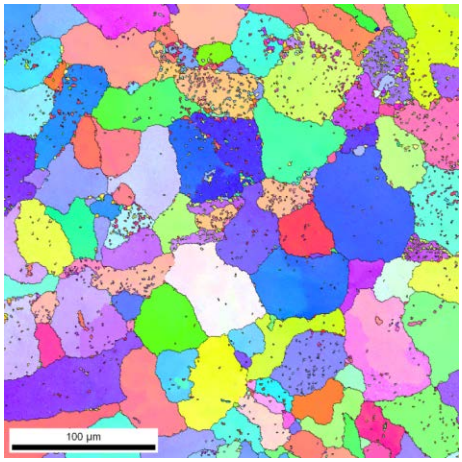

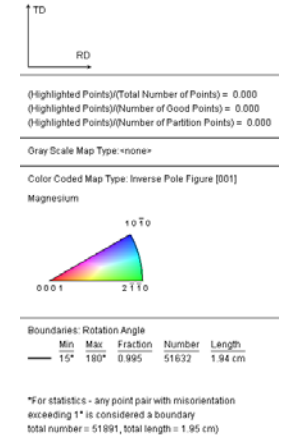

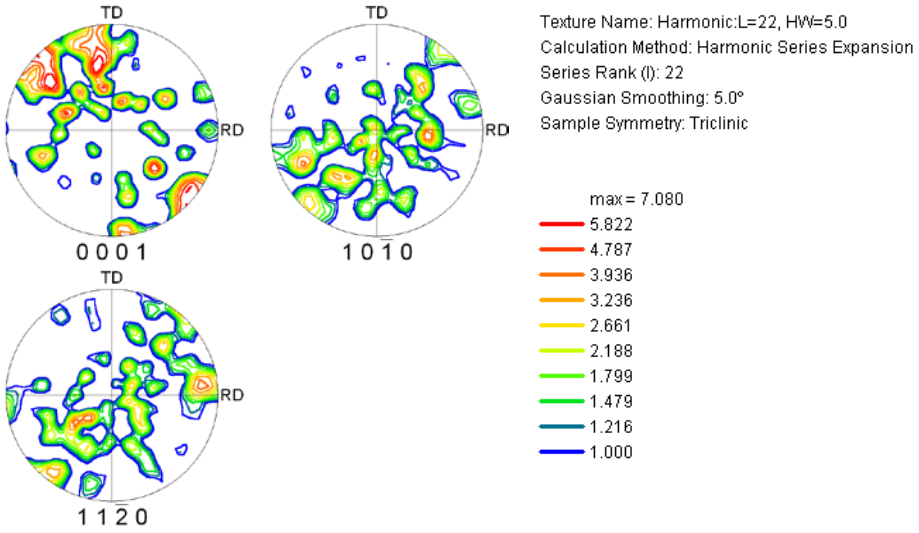

- specimen location: centre of fusion zone on top side;
- grain size: 41.3 µm;
- texture components within selected region of interest: (0 1 -1 0)[uvtw] as well as (5 5 -10 12)[uvtw] and (1 1 -2 -1)[uvtw];
- equiaxial grains, prismatic and pyramidal crystal planes are pronounced.

Fusion zone on the bottom side (see SEM image #2647):
EBSD data: Spec6b_#05/Position: x_4 = 6.197 mm, y_4 = -36.454 mm

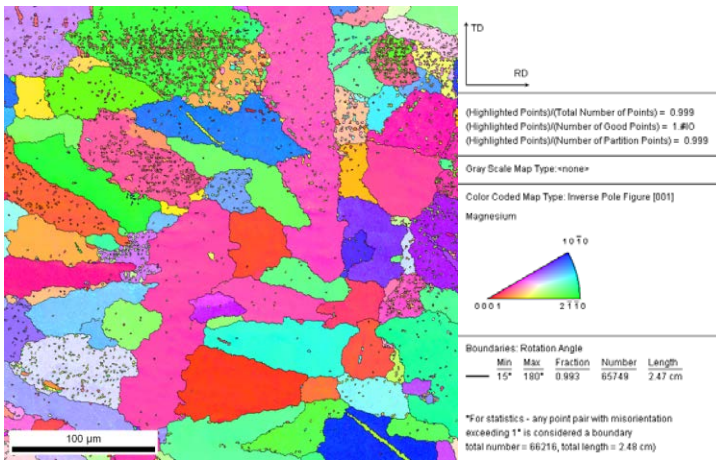

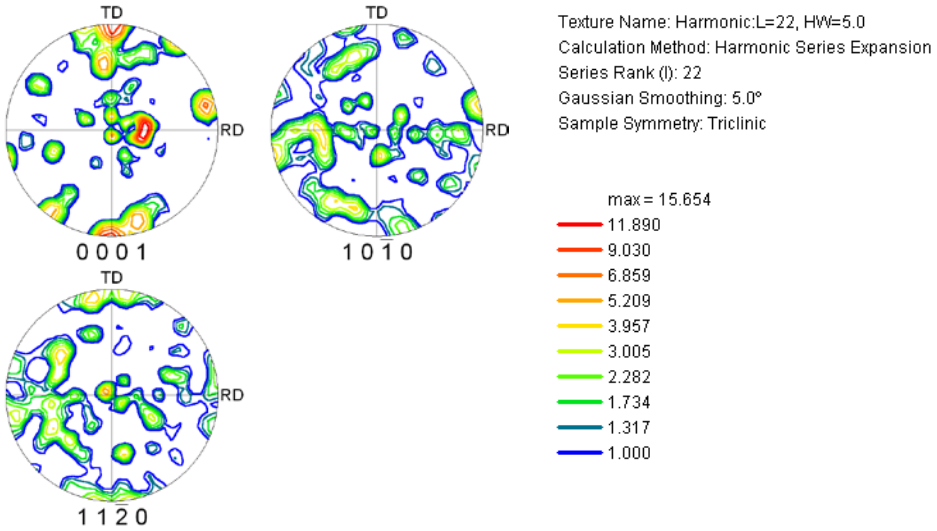

- specimen location: fusion zone on bottom side;
- grain size: 55.0 µm;
- texture components within selected region of interest: basal-transversal texture
- equiaxial grains, basal and primatic crystal planes are pronounced.

Property/Region	BM	HAZ
grain size	16.1 µm	top side: 16.4 µm overlap zone: 9.6 µm bottom side: 14.5 µm
texture	<0001>// TD fibre (1 0 -1 0)[0 0 0 1]	top side: <0001>//TD fibre overlap zone: <0001>//TD fibre bottom side: <0001>//TD fibre

Table: Results of EBSD analysis regarding base material and HAZ

Property/Region	FZ (edge, dendritic)	FZ (middle, equiaxial)
grain size	top side: 31.0 µm overlap zone: 37.7 µm bottom side: 36.6 µm	top side: 41.3 µm centre: 52.9 µm bottom side: 55.0 µm
texture	top side: (0 3 -3 1)[-19 9 10 3] (0 3 -3 2)[18 -14 -4 15] (0 3 -3 5)[12 -1 -11 6] (2 2 -4 7)[-11 -3 14 12] (2 2 -4 -3)[-12 17 -5 10] (1 1 -2 9)[-16 13 3 1] overlap zone: (0 0 0 1)[1 1 -2 0]@θ=15° B/T texture bottom side: (1 0 -1 0)[1 1 -2 0]@θ=15°	top side: (0 1 -1 0)[uvtw] (5 5 -10 12)[uvtw] (1 1 -2 -1)[uvtw] overlap zone: (8 16 -24 13)[22 -15 -7 8] (2 3 -5 35)[-28 -7 21 4] (5 9 -14 12)[-8 4 4 5] bottom side: B/T texture

Table: Results of EBSD analysis regarding the fusion zone (FZ)

APPENDIX E – Second path for EDX investigation of laser beam weld

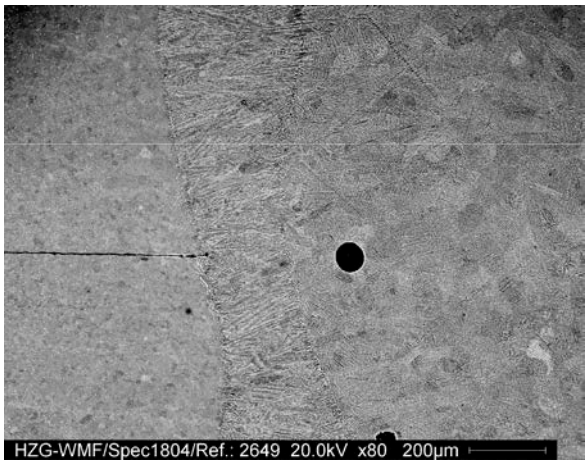

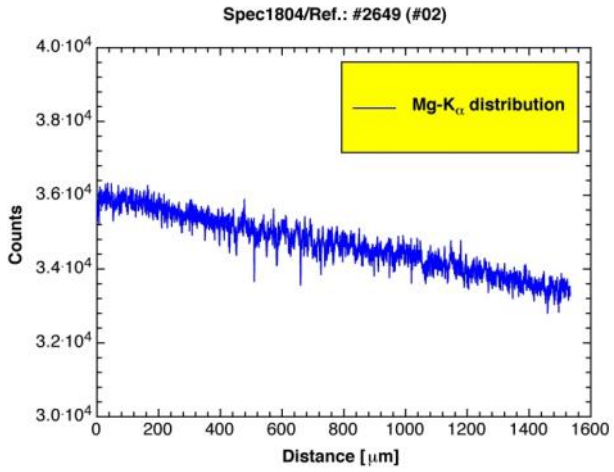

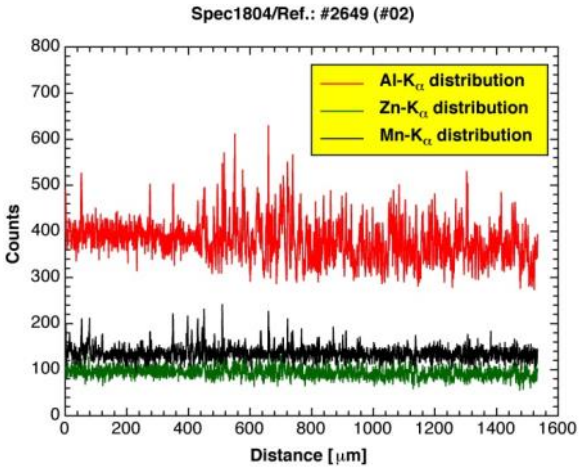

APPENDIX F- Breve estratto in lingua italiana

Negli ultimi anni, come metalli strutturali, le leghe di magnesio hanno ricevuto una crescente attenzione in diversi settori come l'aerospaziale, automobilistico ed elettronico.
Le informazioni di base, per quanto riguarda l'argomento di tesi, sono riportate nel Capitolo 2. Le elevate caratteristiche delle leghe di magnesio, rispetto ad altre leghe, in termini di rapporto "resistenza-peso" e di riciclabilità, le rendono adatte alla fabbricazione di componenti nell'industria automobilistica. L'utilizzo del magnesio in applicazioni automotive può contribuire significativamente alla riduzione dei pesi grazie alla combinazione tra bassa densità, elevata resistenza specifica e rigidezza [40]. La lega di magnesio AZ31B, utilizzata in questo lavoro di ricerca, è stata ampiamente sperimentata nei settori dell'ingegneria più innovativi grazie alla sua leggerezza. In particolare, nell'ambito dell'industria dei trasporti, la sostituzione di parti in acciaio e alluminio è stato un fattore rilevante per l'aumento della velocità e la riduzione dei consumi di carburante nei veicoli.
Nello sviluppo di nuovi tipi di leghe, le tecniche di produzione e giunzione, come la saldatura, svolgono un ruolo essenziale.
Metodi di saldatura attuali, come il MIG, TIG, saldatura a resistenza (RSW), Friction Welding , Electron Beam, saldatura a fascio laser (LBW) e saldatura ibrida laser-TIG, sono stati utilizzati in passato per la giunzione di leghe di magnesio [2-7, 17-22].
Tuttavia, la necessità di ridurre i tempi ciclo e la scarsa flessibilità nelle strutture complesse della convenzionale saldatura a resistenza, hanno attirato l'attenzione delle industrie automobilistiche verso il processo di saldatura laser (LBW) [2].
Il processo di LBW può rivelarsi una soluzione soddisfacente per l'alta velocità di esecuzione, il basso apporto termico e stress residui che assicurano una bassa distorsione del giunto saldato. Inoltre, la saldatura laser, in configurazione overlap, compete nei confronti del RSW, nella fabbricazione ed assemblaggio di carrozzerie, per il fatto di essere un processo senza contatto in cui è sufficiente che il giunto sia "a vista".
I recenti sviluppi di laser ad alta potenza e nel settore del controllo robotico hanno accelerato l'applicazione del LBW nell'assemblaggio delle parti strutturali dell'autoveicolo, al posto del processo di saldatura a punti.

I parametri di saldatura di prossimità, tramite singolo fascio laser (non con sorgenti ibride multiple), può essere implementato tramite scanner in remoto. Per esempio, si prevede che l'utilizzo di uno scanner ottico aumenti la produttività e riduca il costo nella produzione industriale.
Nel Capitolo 3 è presentato lo stato dell'arte della saldatura laser e quella per resistenza (RSW) di leghe di Mg. In letteratura l'ottimizzazione e la saldabilità dei laminati in lega di magnesio sono ben discussi. I giunti saldati laser di lega di magnesio AZ31B sono stati investigati in 18 articoli utilizzando diverse sorgenti (laser a diodi, laser in fibra, Nd: YAG, CO_2 e ibride), in accoppiamenti con diverse configurazioni (saldature di testa, per sovrapposizione, ad angolo, ecc.). Secondo le conoscenze dell'autore, non è presente ad oggi in letteratura una sistematica caratterizzazione meccanica per le saldature laser in overlap nel caso di lega AZ31B.
Inoltre, per i laminati in lega di magnesio è assente qualsiasi confronto tra giunti overlap saldati laser (LBW) e quelli saldati per punti (RSW). I pochi documenti, riguardo quest'ultimo argomento, si concentrano su altri materiali come gli acciai ad alta resistenza per applicazioni automobilistiche.
Le metodologie applicate utilizzati per la progettazione degli esperimenti e l'analisi dei risultati sono discusse nel Capitolo 5.
L'attrezzatura di laboratorio fornita dall'Helmholtz-Zentrum Geesthacht e utilizzata durante il lavoro sperimentale è esposta nel Capitolo 6. Sono presentate le caratteristiche del sistema di saldatura laser, del robot utilizzato, delle macchine per i test meccanici e della strumentazione per l'analisi chimica e delle microstrutture: microscopio ottico, SEM, EDX, EBSD.
La progettazione del lavoro sperimentale e l'analisi dei risultati sono qui presentati nei Capitoli 7-8. La sperimentazione concerne la saldatura laser (LBW) di laminati sovrapposti in lega di magnesio AZ31B utilizzando una sorgente laser Nd: YAG . Si è cercato di sviluppare un processo di saldatura laser ottimale di leghe di magnesio per supplire alla mancanza di conoscenza di queste giunzioni nel settore automobilistico. La ricerca indaga, dapprima, la combinazione dei parametri di processo e progettazione del giunto che migliora la resistenza strutturale e la fatica dei componenti meccanici. Per questo sono state realizzate e caratterizzate meccanicamente cordoni saldati laser con diverse forme (lineari, circolari, C-shape). Il comportamento meccanico dei provini saldati laser è stato testato sotto carichi ciclici e statici confrontando i risultati con le tradizionali saldature. E' offerto un approfondito confronto tra due processi

di saldatura, la saldatura a punti e la saldatura laser, essendo, il primo (RSW) riferimento dello stato dell'arte nella pratica industriale e il secondo un nuovo concorrente, utilizzando la lega di magnesio AZ31B.

- Le principali conclusioni possono essere riassunte nei seguenti punti. Il processo di saldatura laser per sovrapposizione di laminati è stato sviluppato ed ottimizzato. Nel corso di questo lavoro, sono stati realizzati cordoni di saldatura privi di difetti e con opportune geometrie.

- Le prove di trazione hanno rivelato che le diverse forme di saldatura laser, ad esempio quella lineare, circolare e ad arco, non influenzano in modo significativo il comportamento meccanico dei giunti overlap in AZ31B. Inoltre, le saldature laser lineari garantiscono il comportamento a fatica ottimale. Le saldature per punti, realizzate grazie a STADCO Saarlouis Ltd., presentano vuoti e microcricche all'interno della zona di fusione. Tali difettosità non sono state osservate nelle saldature laser realizzate presso l'HZG.

- I valori di durezza della zona fusa erano inferiori a quelli del materiale base.

- Rispetto al giunto saldato a resistenza (RSW), la saldatura laser lineare ha richiesto un tempo ciclo minore ed ha mostrato un superiore carico di rottura (UTSL) a trazione. La resistenza a rottura delle LBWs lineari (dividendo il valore UTSL per l'area resistente del giunto) era paragonabile a quello delle RSWs.

- A basso numero di cicli le LBWs hanno mostrato una resistenza maggiore rispetto alle RSWs. Sia le LBWs che le RSWs, realizzate nel corso di questo lavoro di tesi, hanno potenziato i valori di rottura a fatica trovati in letteratura per le convenzionali RSWs in lega di Mg AZ31B.

- Rispetto alle tradizionali saldature per punti, le saldature laser possedevano un migliore comportamento a fatica e una resistenza alla trazione comparabili.

- Partendo da uno studio di base sulle diverse forme del cordone di saldatura (lineare, circolare, C-shape) realizzate con un processo laser di prossimità, poiché la sorgente è composta dal solo fascio laser, la stessa condizione sperimentale può essere implementata anche su un sistema di saldatura scanner in remoto per aumentare il throughput, ad esempio, nel settore automotive.